SIMULATION OF RESPIRATORY FLOW IN HUMAN UPPER AIRWAY MODEL

MING-ZHEN LU

PhD

The Hong Kong Polytechnic University

2019

The Hong Kong Polytechnic University

Department of Mechanical Engineering

SIMULATION OF RESPIRATORY FLOW IN HUMAN UPPER AIRWAY MODEL

MING-ZHEN LU

A thesis submitted in partial fulfillment of

requirements for the degree of

Doctor of Philosophy

April, 2018

CERTIFICATE OF ORIGINALITY

I hereby declare that this thesis is my own work and that, to the best of my knowledge and belief, it reproduces no material previously published or written, nor material that has been accepted for the award of any other degree or diploma, except where due acknowledgement has been made in the text.

____

Ming-Zhen Lu

Abstract

Obstructive sleep apnea (OSA) is a common disorder characterized by partial or complete narrowing of the pharyngeal airway during sleep. The pathogenesis of this disorder is not, however, fully understood yet, and a better understanding of OSA pathophysiology is required in order to guide treatment planning. Widening upper airway is a common surgery to treat severe OSA, but the success rate is quite low. To understand the pathogenesis of OSA from fluid mechanics point of view, we carried out both numerical and experimental investigations in this study.

First of all, as Computational Fluid Dynamics (CFD) is a potential non-invasive tool for investigating the pathophysiology of OSA, we carried out CFD for numerical simulation for both normal and OSA subjects. To build the idealized model for CFD simulation, the medical imaging technique is used to generate the upper airway model.

Secondly, because the flow in the upper airway region is expected to be turbulent, different turbulence models including Unsteady Average Navier-Stokes (URANS), two-equation turbulent models (unsteady k-ε, standard k-ω, and k-ω Shear Stress Transport) and Large Eddy Simulation (LES) model were compared in CFD numerical simulation. It is concluded that the LES model should be the most appropriate model for this CFD simulation of OSA.

To validate the suitability of CFD modeling methods, we carried out Laser Doppler measurement in 3D-printing OSA upper airway models, and found excellent agreement between the measured and calculated velocity profiles in two upper airway models for the first time. Then four pairs of OSA upper airway subjects with 8 different apnea-hypopnea index(AHI) values are investigated with LES model. It is found that a dominant recirculation downstream of the minimum cross-section should be a main feature of a successful surgery, and the strength of 3-5 Hz signal induced by flow separation in the upper airway plays an important role in appraising breathing quality. This provides a new guideline for surgery planning.

Finally, the stochastic resonance(SR) phenomenon was investigated in both normal and OSA subjects. We found that the SR phenomenon is existed in both subjects. The strong correlation between the signal-to-noise ratio (SNR) and AHI indicates that SR may play an important role in the respiratory system as periodic oscillating signals are enhanced significantly by noise. It seems that the quality of the oscillating signal can serve as a quantitative measure to quantify the breathing quality of OSA subject.

Keywords: OSA, Upper airway, CFD, LES, SR phenomenon.

Publications arising from the thesis

Lu M.Z., Chi T.X.., Liu Z.G., Wang S., Liu Y. and Ye J.Y, 2018. The Comparison of Spectral Analyses and Flow Features in Upper Airways with Obstructive Sleep Apnea (OSA) Between Successful and Failed Surgeries, intend to be submitted to Journal of Applied Physiology.

Lu M.Z., Liu Y., Ye J.Y., Luo H.Y., 2014. Large Eddy Simulation of flow in realistic human upper airways with obstructive sleep, Procedia computer science, 29, 557-564.

Lu M.Z., Liu Y., Ye J.Y., Flow pattern comparison between LES Simulation and Reynolds-Average Navier-Stokes modeling for flow in realistic upper airway models with obstructive sleep apnea, the 3rd International Conference on Computational and Mathematical Biomedical Engineering, Hong Kong, China, on December 16 – 18, 2013.

Lu M.Z., Liu Y., Ye J.Y., Large Eddy Simulation of Flow with Obstructive Sleep Apnea at Pre- and Post-Surgical Treatment, the 4th International Conference on Computational Methods, Gold Coast, Australia, on November 25 – 28, 2012.

Lu M.Z., Liu Y., Ye J.Y., Turbulent Flow Pattern in Upper Airway with Obstructive Sleep Apnea, 15th International Symposium on Flow Visualization, Minsk, Belarus, on June 25 – 28, 2012.

Lu M.Z., Liu Y., Ye J.Y., Flow Pattern Comparison in Upper Airways of Two OSA Subjects Before and After Surgery, 19th Congress of the European Society of Biomechanics, Patras, Greece, on August 25 – 28, 2013.

Acknowledgements

I would like to express my sincere gratitude to my supervisor Dr. Yang LIU for guiding me into the world of CFD, for his precious advice, cheerful encouragement and endless patience. This dissertation cannot be finished without his invaluable supervision.

Also I would like to thank my former and present team members Dr. Zhengang Liu and Dr. Weiwei Yan for providing the necessary assistance. Special thanks to Dr. Zhenggang Liu for sharing his expertise on mathematics.

This dissertation is dedicated to my parents for their endless love, understanding and support, the lady Ms. Lan Ma who holds my hand and brings me sunshine on my toughest days.

Table of Contents

List of Abbreviations

AASM American Academy of Sleep Medicine

AHI Apnea-hypopnea Index

APAP Automatic Positive Airway Pressure

AR Area-Ratio

BFO Bacterial Foraging Optimization

CAD Computer Aided Design

CFD Computational Fluid Dynamics

CPAP Continuous Positive Airway Pressure

CT Computed Tomography

CVs Small Contral Volumes

DNS Direct Numerical Simulation

EEG Electroencephalography

EMG Electromyography

EPG Electrooculography

FDA Food and Drug Administration

FDM Finite Difference Method

FEM Finite Element Method

FFT Fast Fourier Transformation

FVM Finite Volume Method

HU Hounsfield Unit

ICSD Ⅱ Second International Classification of Sleep Disorders

LAUP Laser-Assisted Uvulopalatoplasty

LDA Laser Doppler Anemometer

LES Large Eddy Simulation

LP Laryngopharynx

LRN Low Reynolds Number

MAD Mandibular Advancement Device

MAS Mandibular Advancement Splints

MMA Maxillomandibular Advancement

MRI Magnetic Resonance Imaging

NP Nasopharynx

OP Oropharynx

OSA Obstrictive Sleep Apnea

OSAS Obstructive sleep apnea syndrome

PDE Pritial Differential Equations

PSD Power Spectral Density

PSG Polysomnography

RANS Reynolds Average Navier-Stokes

Re Reynolds Number

RP Rapid Prototyping

SGS Sub-Grid-Scale

SNR Signal-to-Noise Ratio

SR Stochastic Resonance

SRBD Sleep-Related Breathing Disorders

SST Shear Stress Transport

UA Upper airway

UPPP Uvulopalatopharyngoplasty

URANS Unsteady Reynolds Average Navier-Stokes

VPAP Variable Positive Airway Pressure

WALE Wall-Adaption Local Eddy-Viscosity

1D One Dimensional

2D Two Dimensional

3D Three Dimensional

Chapter 1 Introduction

1.1 Significance

The upper respiratory tract, or upper airway (UA) is a complex and highly variegated ensemble of soft tissues, muscles and bony structures which, by modulating its patency, plays a crucial role in respiration, speech and alimentary functions. The UA proceeds from the mouth, nose, sinuses and throat, down to and merging with the lower respiratory tract, which latter consists of the trachea together with the bronchial tubes that terminate at the innermost structures of the lungs (Ballentine et al., 1998). The main region of the UA in which an obstruction may occur is the pharynx, this usually divided anatomically into three parts, as shown in Fig. 1.1: the nasopharynx (NP, from the end of the nasal septum to the free margin of the soft palate or uvula), the oropharynx (OP, from the margin of the soft palate to the tip of the epiglottis), and the hypopharynx, also called the laryngopharynx (LP, from the tip of the epiglottis to the vocal cords) (Xu et al., 2006).

Obstructive sleep apnea (OSA), or obstructive sleep apnea syndrome (OSAS), is the most common type of sleep disorder. It is characterized by abnormal, repetitive pauses in breathing, or instances of abnormally low breathing, during sleep (Gleadhill, et al., 1991; De Backer, 2006). There is partial or complete narrowing of the UA, leading to a reduction in blood oxygen saturation which culminates in sleep disruption. OSA affects about 20% of the adult population and 2% of children. The disorder is increasingly recognized as an independent risk factor for a range of conditions including diabetes, hypertension and stroke (McCabe & Hardinge, 2011).

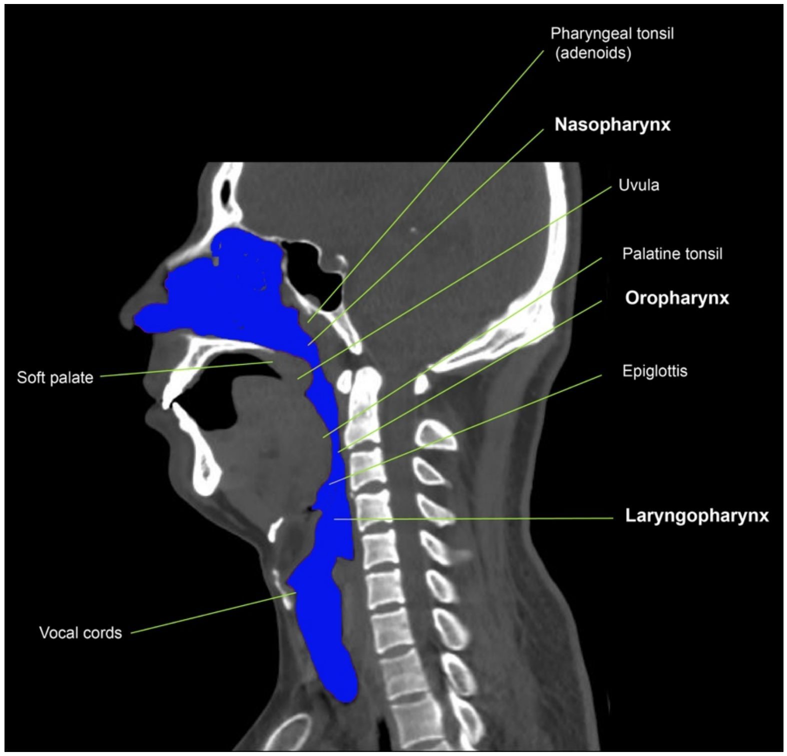

Fig. 1.1 Major structure of upper airway.

The short-term consequences of sleep apnea include sleep fragmentation, loud snoring, daytime sleepiness, and fatigue-related accidents. Without prompt treatment in these early stages, adverse effects on neurocognitive and cardiovascular functions may in the long-term develop, exerting negative impacts on multiple organs and systems (Lipton & Gozal, 2003). Among the possible anatomical factors, upper airway narrowing has been reported in both child and adult subjects with OSA, a structural change which may predispose an airway to collapse (Miyazaki, et al., 1989).

A better understanding of the unsteady flow field inside the airway will facilitate the characterization of airflow and pressure forces associated with airway narrowing in OSA patients. Due to the non-invasive characteristics of the UA, as well as its complex geometry, it is difficult and expensive to conduct experimental measurements on an OSA patient, whether in-vitro or in-vivo. Here we expect to use the computational fluid dynamics (CFD) technique, which has better non-invasive features. Investigating the UA within the context of OSA will contribute to the understanding of the mechanism of UA flow characteristics.

1.2 Background and Literature Review

1.2.1 Sleep disorder and Obstructive Sleep Anpea

Sleep occupies one third of human life, and is related to the cardiovascular system, along with the regulation of brain glucose metabolism. Sleep is not, however, a steady state of unconsciousness, but a periodic process. In order to classify sleep, Rechtschaffen and Kales (1968) introduced discrete sleep stages based on waves and patterns measured by electroencephalography (EEG) and electrooculography (EOG), as well as mental or sub-mental muscle tone as measured by electromyography (EMG) (Table 1.1). The Second International Classification of Sleep Disorders (ICSD Ⅱ) lists many disorders, such as insomnias, hypersomnias, parasomnias, sleep-related breathing disorders (SRBD), sleep-related movement disorders, and circadian disorders (Levy, et al., 2006), all of which, taken cumulatively, are emerging as a substantial public health issue.

Obstructive sleep apnea is a common SRBD. As noted above, OSA induces a reduction in, or complete cessation of, airflow in the ongoing respiratory effort.

Table 1. 1. The sleep stages and their characteristic features follow by Rechtschaffen and Kales, 1968

Sleep Stages	Features
Wake	Beta, alpha >50% /epoch; rapid eye movements; muscle tone highest
REM	Theta, some alpha; rapid phasic eye movements; muscle tone lowest
NREM1	Theta, alpha<50% /epoch; slow eye movements; muscle tone reduced
NREM2	Theta, spindles. K-complex; no eye movements; muscle tone low
NREM3	Theta, delta >50%/epoch; no eye movements; muscle tone very low

1.2.2 Symptoms of OSA

The most direct symptoms of OSA are witnessed apneas. The apnea-hypopnea index (AHI) represents the number of apneas and hypopneas per hour, a number used to define and characterize the severity of the sleep apnea syndrome. A patient with apnea experiences a cessation of airflow of at least 10s in duration, and an AHI of >5-10 events per hour. With a rise in AHI come two main consequences. The first is that patients undergo an increased number of sleep arousals, disruptions in sleep architecture which result in non-restorative sleep and are experienced as daytime somnolence. The second consequence is impaired cardiovascular function. Repetitive hypoxemia can cause tissue damage, and may play a role in the development of cardiovascular disease (Yim S., 2006).

Table 1.2. Severity indices of OSA

	AHI, events/h	**O_2 saturation, %**
Normal	<5	>95
Mild	5-19	>85
Moderate	20-39	>65
Severe	>40	<65

Snoring is one of the most common symptoms of OSA, occurring in 70-95% of patients (Whyte et al., 1989). Although severity of snoring is not an indicator of sleep apnea, only 3-6% of non-habitual snorers have OSA (Young et al., 1993).

Like snoring, daytime sleepiness is relative common: approximately 20-30% of the general population suffers from it (Duran et al., 2001). Of those who suffer from it enough to visit a sleep clinic, 80-90% are subsequently diagnosed with sleep disorder (App et al., 1990).

Symptoms for children may differ from those observed in or reported by adults. For instance, children so affected may sleep longer than usual, an occurrence more frequent among obese children, or those with severe apnea. There may be more effort in breathing, the chest displaying an inward motion during sleep. Growth failure (apart from weight gain) may result, and the child may exhibit behavioral problems for which there is no obvious cause.

1.2.3 Pathogenesis of OSA

It is widely known that UA collapse is governed by a complex interplay of mechanical and neuromuscular factors, including abnormal anatomy of the upper airway, pathological and insufficient reflex activation of the upper airway dilator muscles, and increased collapsibility of the passive upper airway. However, the pathogenesis of OSA is not yet clearly understood. It was originally believed that upper airway patency is determined by the balance of pressures between the intraluminal and extraluminal space (Remmers, et al., 1978). When intraluminal suction pressure (negative pressure) overcomes the dilating force, the pharynx will (or so it was thought) collapse during sleep. But later studies have found that the upper airway can occlude spontaneously, even when intraluminal pressure is positive (Schneider, et al., 2002), a finding that minimizes the role of intraluminal suction pressures in the pathogenesis of upper airway obstruction. What these studies demonstrate is that the negative intraluminal pressures generated during upper airway obstruction are the consequence, rather than the cause, of upper airway occlusion (Kirkness, et al., 2006).

Starling Resistor Model for Upper Airway Obstruction

As seen in Fig. 2, the upper airway can be represented as a mechanical analogue of the Starling resistor model, consisting of a rigid tube with a collapsible segment. Upper (upstream, nasal) and lower (downstream, hypopharyngeal) segments have fixed diameters and defined resistances. Pressures in these segments are represented by P_{us} and P_{ds}, respectively. The collapsible segment has no resistance, but is subject to the surrounding pressure P_{crit}. Airway flow limitation is induced when downstream pressure falls below P_{crit} during inspiration (Pride, et al., 1967). For airway flow limitation, the airflow will rise to a maximal level (V_{Imax}) despite further increase in inspiratory effort (Schwartz, et al., 1989).

$$V_{\mathrm{Im}ax} = (P_{us} - P_{crit}) / R_{us} \qquad (1.1)$$

Under flow limitation, the level of maximal inspiratory airflow is determined by the upper airway and critical pressures together with upstream nasal resistance, as described in the equation (1.1). As V_{Imax} falls, obstructive hypopneas, snoring, and URAS will result. However, according to the Starling resistors prediction, decreasing downstream pressure will not cause the flow-limited airway to occlude (Schwartz, et al., 1988; Whyte K.F., 1989).

Complete airway occlusion occurs only when P_{crit} exceeds both the upstream and downstream pressure (lower panel), as demonstrated experimentally in normal sleeping individuals by Schwartz, et al. (1988). The Starling resistor model was able to predict the effects of pressure on airflow dynamics, as well as the severity of UA obstruction during sleep.

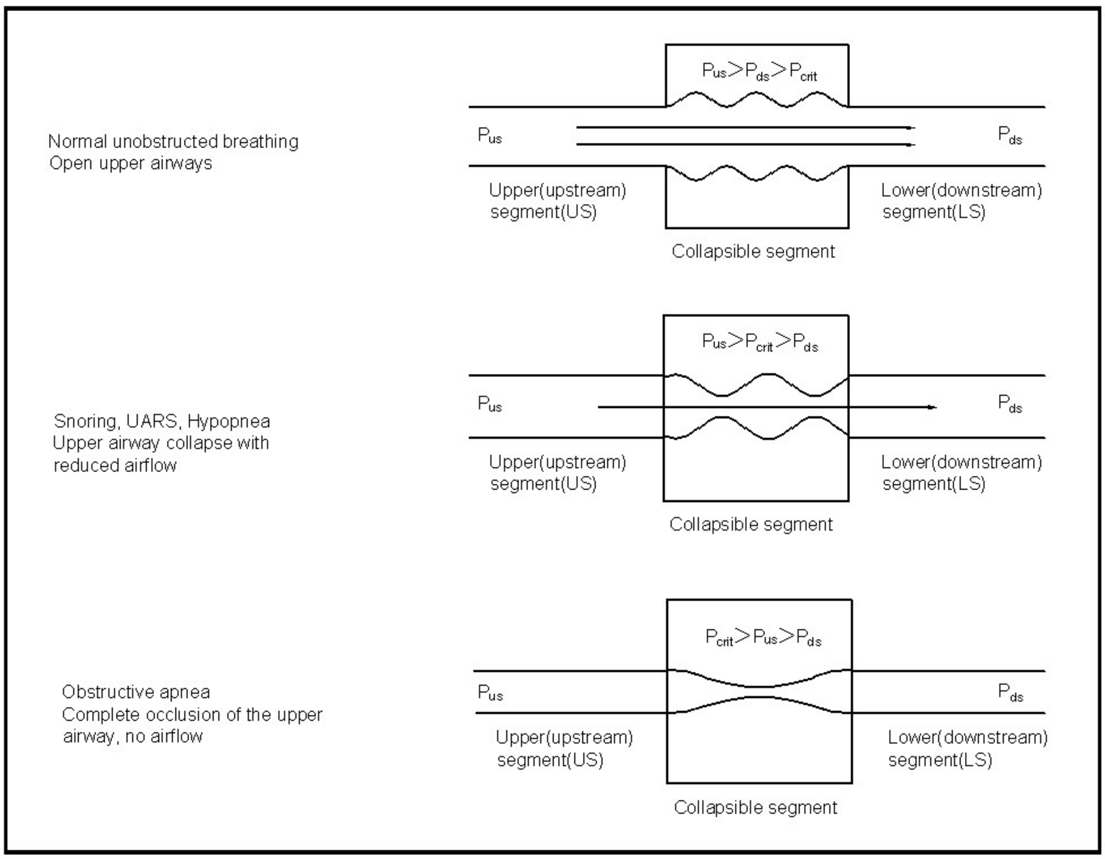

Fig.1.2. The relationship between pressure and flow in the upper airway segment.

In further study, the critical pressures were measured based on manipulation the upstream nasal pressure for groups of individuals with different degrees of UA obstruction during sleep by Schwartz et al. (1988) as shown in Fig. 1.3. They found that critical pressures were markedly negative in normal individuals, indicating that both upstream and downstream pressures were larger than critical pressures and that breathing was completely unobstructed. While critical pressures were positive in obstructive hypopnea or apnea patients with complete upper airway collapse and finally occlude. For apneic patients with complete UA occlusion, the critical pressures were positive. For patients with partial UA obstruction with (snoring or UA resistance syndrome and obstructive hypopnea) critical pressures were between these two ranges during sleep.

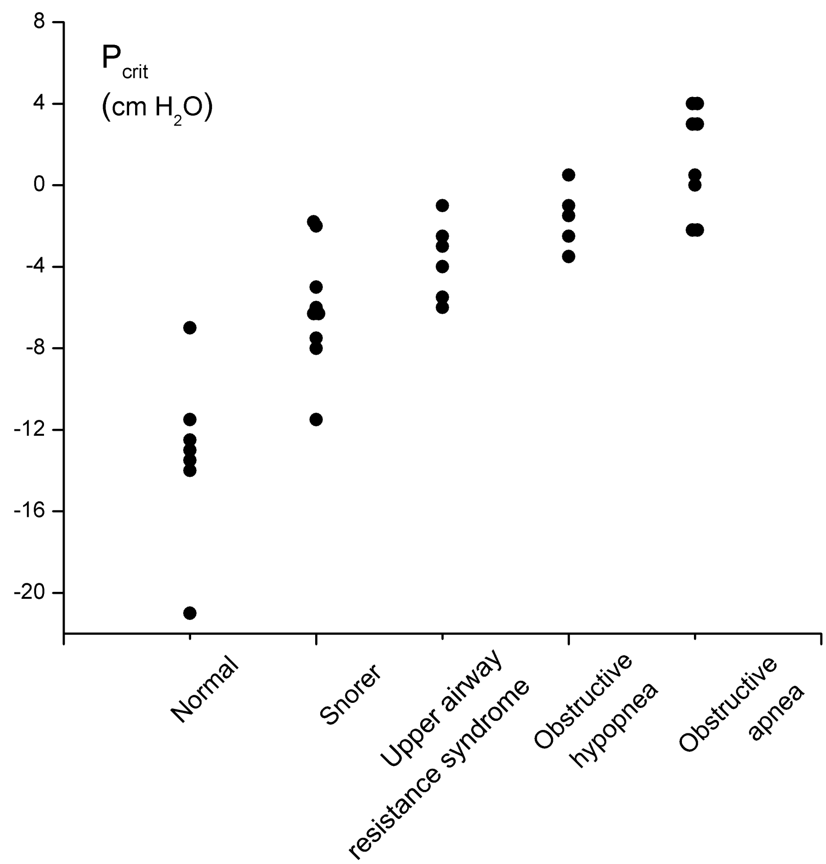

Fig.1.3. Upper airway critical extra-luminal pressures and clinical express.

Abnormal Anatomy of the UA

Abnormal anatomy of the UA includes tonsillar hypertrophy, retrognathia, and variations in craniofacial structure, all of which contribute to increased risk of OSA. (Miyazaki, et al., 1989) Computed tomography (CT) and magnetic resonance imaging studies both provide evidence that fatty tissue deposits in the lateral pharyngeal walls result in narrowing and collapse of the UA during sleep. Suratt et al. (1983) have used lateral fluoroscopy and CT scans to study the anatomical structure of the UA in both normal and OSA subjects. Their studies found that obstructions always begin during inspiration, when the tongue comes into contact with the soft palate and posterior pharyngeal wall during sleep, and that the narrowest section of airway in OSA patients and in normal subjects was the region posterior to the soft palate. The cross-sectional area near the retro-palate was quite narrower in OSA patients during inspiration compared to normal subjects. The researchers concluded that abnormally narrow airway is an important factor in the pathogenesis of OSA.

Insufficient Reflex Activation of UA Dilator Muscles

The imaging studies show that UA dilator muscle activation in OSA patients is quite adequate, and even intensified, during wakefulness (Fogel, et al., 2000). This activation is mainly induced by the negative intra-luminal pressures due to the narrow airway in OSA patients. However, dilator muscle activation in OSA patients decreases significantly during sleep, especially during NREM sleep, at which time it is suspended completely (De Backer, 1993). Due to the loss of this reflex activation of

UA dilator muscles during sleep, the UA of OSA patients may be narrower during inspiration than in normal subjects.

Increased UA Collapsibility

Because the increased level of UA collapsibility would lead to greater degree of airflow obstruction, increased airway collapsibility contributes significantly to UA collapse in with OSA patients. UA collapsibility is defined by the critical pressure (P_{crit}) determined by the relationship between maximal inspiratory airflow and nasal pressure (Gleadhill, et al., 1991). It has been shown that, during inspiration, the P_{crit} is determined by the anatomy of the UA, especially the cross-sectional area of the UA.

1.2.4 Diagnosis and Treatments

Diagnosis

Polysomnography (PSG) is the standard method for diagnosing OSA during sleep, at which time decreased blood oxygen and increased blood carbon dioxide emerge with repetitive apneas. Cessation of breathing is not, however, accompanied by an absence of inhalatory chest movement; rather, the chest movements become more notable. PSG allows many characteristics to be monitored, including brain waves, eye movements, heart rate and rhythm, blood pressure, blood oxygen levels, breathing patterns, body position, limb movement, snoring and other noises. Small sensors (electrodes) monitor brain waves, while elastic belts around the chest and stomach track breathing patterns. A small finger clip records blood oxygen levels. All of the data is entered into a computer. AHI and oxygen saturation are indices used to diagnose the severity of OSA (Table 1.2).

Treatments

There are various treatment options for OSA, which mostly depend on the sites of obstruction or collapse, symptom severity, and the extent of clinical complications. The selection of these treatments should balance the consider multiple factors and the effectiveness of the treatment.

Behavioral and Medical Treatments: The airway of a sleeper who has adopted a supine position may collapse due to gravitationally induced relaxation of the pharyngeal tissues. To counter the effects of gravity, sleep at a 30 degree, or a lateral position (sleeping on a side), are recommended treatments for sleep apnea (Szollosi, et al., 2006). Either position can easily be used in combination with other treatments, and may be particularly effective in morbidly obese patients. Overweight patients with OSA may find that weight loss leads to reductions in snoring and hypopnea/apnea. Habits such as smoking, alcohol and drugs are best quit. There remains, however, little evidence of supporting the medical treatment of OSA.

Continuous positive airway pressure (CPAP) is considered the best treatment for OSA on account of its safety and effectiveness for people of all ages, including children. The treatment is conducted by use of a mask to supply a continuous stream of compressed air into the airway, increasing nasal pressure (upstream pressure) to prevent UA collapse. It is suitable for patients with mild to severe OSA. However, compliance with CPAP is a problem for some patients. A newer form of treatment - automatic positive airway pressure (APAP), or Auto CPAP - has been approved by the U.S. Food and Drug Administration (FDA). APAP treatment integrates pressure sensors with a computer that continuously monitors a patient's breathing performance, adjusting airway pressure as needed (Whitelaw, et al., 2005)

A more expensive treatment is variable positive airway pressure (VPAP), which uses an electronic circuit to monitor breathing performance, providing higher pressure during inhalation and lower pressure during exhalation. This method is used to treat patients who have additional, coexisting respiratory problems, and/or who find the increased pressure of CPAP to be uncomfortable or disruptive to their sleep. However, some OSA patients feel that VPAP, too, is uncomfortable.

Although CPAP is a very effective treatment for OSA, acceptance and adherence have been a challenge. Dental devices may then present an alternative treatment option for patients who cannot tolerate CPAP. The American Academy of Sleep Medicine (AASM) recommends dental devices for patients with mild to moderate OSA who are not compliant for CPAP or who have not been helped by it. The most widely used dental device for treatment of OSA is the mandibular advancement device (MAD), which moves the lower jaw forward and down slightly in order to maintain UA patency. The MAD can significantly reduce apneas, especially for those who sleep on their backs or stomachs, and can reduce the frequency of snoring in most patients.

However, this treatment is not as effective as CPAP, and the devices are expensive. Long term complications, such as nighttime pain, dry lips and tooth discomfort, may cause nearly half of patients to stop using dental devices. In some cases, the treatment may worsen the apnea.

Surgery then becomes an option for patients, particularly those with severe OSA, who are not compliant with CPAP and for whom other treatments have also failed. Surgical treatment of OSA aims to improve the size or tone of a patient's UA. For decades, tracheostomy was the only effective treatment for sleep apnea, but several more recent surgical techniques have been employed (Boudewyns & Van de Heyning, 2006), including:

1) Nasal surgery: Turbinectomy, in which removes or reduces some or all of the nasal turbinate attached to mucous membranes in the nasal airway in order to decrease the nasal obstruction and increase the nasal pressure. However it may result in empty nose syndrome.

2) Tonsillectomy or adenoidectomy: Uvulopalatopharyngoplasty (UPPP) attempts to increase the size of the airway, via removal or reduction of parts of the soft palate and some or all of the uvula (Fig. 1.4). While UPPP is the most commonly performed surgical procedure for OSA, it is not always the sole procedure; it may, in some cases, be coordinated with other treatment methods. One of the challenges for UPPP is how much tissue should be cut: too little excision may fail to obtain the surgical target, while excess tissue reduction may 'tighten' the airway and so worsen the disease. Another adenoidectomy is laser-assisted uvulopalatoplasty (LAUP),

which removes less tissue at the back of the throat than does UPPP, the specific goal being reduction of snoring.

3) Reduction of the tongue base, by use of either laser excision or radiofrequency ablation.

4) Reduction of the tongue base, by use of either laser excision or radiofrequency ablation. Hyoid suspension, which moves the hyoid bone in the neck forward to the front of the larynx.

5) Maxillomandibular advancement (MMA) is the most effective sleep apnea surgical procedure currently available, with reduction of the AHI to less than 15 in over 90% of patients, and reduction of AHI to <5 in over 45% of patients(Li, et al., 2000).

Although the majority of medical practitioners suggest CPAP as being suitable for most patients, followed by dental splints and weight loss, with surgical intervention representing a treatment of last resort, it is evident that surgery may obtain the same treatment outcomes as CPAP. Nevertheless, the success rates of the various surgical treatments are still not entirely satisfactory, their efficacy being directly proportional to the accuracy of the initial diagnosis of site of obstruction. Therefore, accurate prediction of the obstruction site together with optimal tissue reduction, are urgent treatment goals.

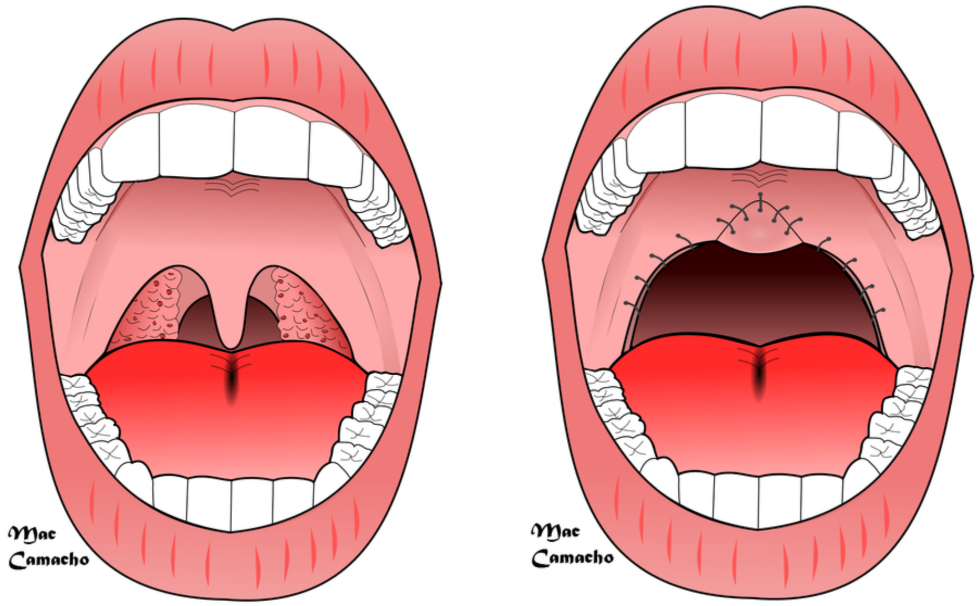

Fig.1.4. Appearance of throat pre- and post- UPPP surgery. Reprinted from http://en.wikipedia.org/

1.2.5 Computational Fluid Dynamics Simulation for the OSA models

In order to predict treatment outcomes with accuracy, it is essential to establish the flow characteristics of the UA in cases of OSA. Recently, due to its non-invasive nature, Computational Fluid Dynamics (CFD) software has been used to analyze fluid flow characteristics in human UA simulation models, especially in cases of OSA. The complexity of the UA demands accurate models in the investigation of OSA mechanisms. Initial studies used simplified geometry models. Malhotra et al. (2002) created simple, 2D male and female upper airways based on the data from 10 subjects, and demonstrated that the male airway is substantially more collapsible than the female airway. They suggested that an increased length of vulnerable airway, as well as increased soft palate size, resulted in the male predisposition to pharyngeal collapse. Martonen et al. (2002) generated a 3D upper airway model based on a medical school teaching model. Their results suggest that airflow patterns are mainly dependent on flow rate values for a prescribed phase of breathing (i.e., inspiration or expiration).

Thanks to the development of computer imaging techniques, more accurate UA simulation models have been used in CFD studies. Nithiarasu et al. (2008) carried out numerical simulation using the Reynolds-Averaged Navier-Stokes (RANS) method based on a CT-scanned upper airway model. Their numerical technique was validated against measurements of an idealized oropharynx from Heenan et al. (2003). Further studies by Jeong et al. (2007) analyzed numerically the flow in a CT-scanned upper airway using a low Reynolds number k–ε model. They found that the turbulent jet formed at the velopharynx due to area restriction was the most noteworthy feature in the pharyngeal airway of patients with OSA. Cheng et al. (2013) also studied the flow in a realistic upper airway using an extended k–ε turbulence model.

In real life situations, the airflow in a human UA is unsteady. Time-averaged turbulence models (Zhao & Lieber, 1994; Nithiarasu, et al., 2008; Jeong, et al., 2007; Cheng, et al., 2013) are unable to capture the characteristics in the anisotropic flow, such as adverse pressure gradients or turbulent velocity fluctuations, generated in these irregular upper airway models (Wilcox, 1998). Direct numerical simulation (DNS) is the best way to capture airway flow characteristics, because it solves the Navier-Stokes and continuity equation directly, and no reductions or assumptions are required in the solving process. Theoretically, the data from DNS can be considered equivalent to the data obtained experimentally (Sodja, 2007). However, DNS is computationally expensive and infeasible for the flow of high Reynolds numbers. Hence, a compromise model between RANS and DNS is the Large Eddy Simulation (LES), which is far more economical than DNS in terms of computational power required, and can resolve the most energetic flow scales (entering into the inertial sub-range) while modeling only the smallest dissipative scales (Pope, 2003). More and more CFD computations on upper airways with OSA are using LES, which is a proven tool for capturing relevant flow features, such as the separation flow downstream of the minimum cross-sectional area(Luo, et al., 2004; Mihaescu, et al., 2008; Mihaescu, et al., 2011; Liu, et al., 2012).

To validate the stability of CFD modeling methods, experimental or clinical data should be collected for comparison. Owing to the development of rapid prototyping technology, the anatomical in vitro airway model of subjects with OSA can be fabricated according to numerical geometry models. Xu et al., (2006) studied the effects of airway geometry on internal pressure in the upper airway of children with OSA, by using a two-equation low-Reynolds number turbulence model with steady flow boundary conditions in inspiration and expiration. To validate their CFD methods, they conducted a physical test with an 85% scale airway model. Wall pressure at each pressure tap location was measured for comparison with the CFD model and clinical studies of nasal resistance in normal children. They found their in-vitro measurements were consistent with the CFD method and the clinical measurements. Mylavarapu et al. (2009) investigated an anatomically accurate human upper airway model which was constructed from MRI scans during expiration. They used unsteady LES, steady RANS with two-equation turbulence models (k-ε, standard k-ω, and k-ω Shear Stress Transport (SST)), and a one-equation Spalart-Allmaras model. To validate their CFD results, they fabricated a 2:1 scale mechanical airway model by SLA, with which they measured wall pressure and mean velocity of the inlet. They found a high correlation between the computations and the experimental results, which suggests that CFD can be used to accurately investigate the aerodynamic flow characteristics of the upper airway. Zhao et al. (2013) used CFD to study the upper airway response to treatment involving mandibular advancement splints (MAS). The physical airway of a patient was fabricated, and the CFD method was validated against the pressure profile of the physical model. The conclusions provide further support for CFD as a potential tool for prediction of the treatment outcomes of MAS in OSA patients without requiring patients' specific flow rates.

1.3 Stochastic Resonance

The addition of noise in a nonlinear system can amplify a weak input so as to increase the output signal-to-noise ratio (SNR), which would improve the ability to transmit signals reliably (Wiesenfeld and Moss 1995). The broadband noise can be either intrinsic to the signal itself, or applied extrinsically to improve performance. This signal enhanced phenomenon is called stochastic resonance (SR), and has been found to exist in many physical and biological systems (Benzi et al. 1981, Bulsara and Gammaitoni 1996, Collins et al. 1995, Suki et al. 1998).

Russell et al. (1999) found that stochastic resonance enhances the normal feeding behavior of paddlefish, which use passive electroreceptors to detect electrical signals from planktonic prey. Bahar and Moss 2003 studied the effects of stochastic resonance on the nonlinear dynamics of the crayfish mechanoreceptor system. They found that the crayfish can detect water motions of as little as 20 nm and quit sensitivity for the light. The SNR was found to be at maximum when the light intensity optimized. Stochastic resonance has also been found in human perception. Hagan et al. (1977) discovered that the vibratory stimuli applied to the chest wall of preterm infants can cause significant changes in breathing patterns. Bloch-Salisbury et al. (2009) used stochastic vibrotactile stimulation to evaluate the hypothesis that low-level noise somatosensory stimulation can stabilize breathing in preterm infants. Their findings suggest that nonlinear properties of the immature respiratory control system can be harnessed using afferent stimuli to stabilize eupneic breathing, thereby potentially reducing the incidence of apnea and hypoxia.

1.4 Structure and Contribution of This Thesis

Chapter 1 describes the extent to which OSA in adults has been shown to be associated with structurally narrow upper airways by comparing OSA patients with normal adults though medical imaging techniques such as CT and MRI, which can quantify and visualize anatomical abnormalities associated with OSA. Uvulopalatopharyngoplasty

(UPPP) is currently the most common surgical procedure used for adults with OSA. However, the success rate of this procedure is limited due to an incomplete understanding of the pathogenesis of OSA. It is therefore necessary to further the understanding of OSA pathophysiology in order to achieve better treatment planning as well as better prediction of surgical outcomes.

Chapter 2 introduces the research methods employed. The governing equation and various turbulence models, including unsteady LES as well as unsteady RANS with two-equation turbulence models (k-ε, standard k-ω, and k-ω Shear Stress Transport (SST)), are presented first. Apart from the numerical methods, the experimental methods, including the experimental methods used to validate the numerical results, together with the experimental methods employed in investigation of the SR phenomenon in OSA patients, are also presented.

Chapter 3: CFD technology with variegated turbulence models (large eddy simulation (LES) and unsteady Average Navier-Stokes (URANS), including unsteady k-ε, unsteady standard k-ω, and unsteady k-ω Shear Stress Transport (SST) models) are applied to investigate airflow in the UA models of two pairs of OSA patients successfully treated with UPPP surgery. The computational fluid dynamics models were constructed from the computed tomography (CT) images of OSA patients. Results indicate that all turbulence models attempted are able to produce the same pressure drop across airway, and that a strong flow jet near the minimum cross section can be found in all models prior to surgery. LES is better able to capture the flow oscillation downstream of the minimum cross section near the retro-palate than is

URANS. URANS models cannot replace LES models for accurate prediction of surgical outcomes.

Chapter 4: in order to validate the CFD results, two 1:1 scaled in vitro airway physical models are fabricated. Earlier studies experimentally validated CFD results by focusing mainly on UA wall pressure via the setting of pressure taps. Our work experimentally validates the inner velocity distributions with LES. The experimental models are fabricated by means of a rapid prototyping method - 3D printing technology - and internal velocity is measured by the Laser Doppler Anemometer system. There is strong evidence that axial velocity from LES well agrees with the experiment results, and that LES is the better method for investigating flow features in the UA as well as for predicting surgical outcomes for patients with OSA.

Chapter 5 presents a study of four OSA patients, three of whom experienced successful UPPP surgery and one of whom did not (assessed by the apnea-hypopnea index (AHI)). The aim is to reveal flow variation between successful and unsuccessful OSA patients. Results indicate that there is still negative pressure in the minimum cross section of the unsuccessfully treated patient. This persistent negative pressure is considered the most important feature of upper airway collapse. Another factor may be a shift in location of the minimum cross section from the retro-palate to the oropharynx. It was also found that AHI and the area ratio of the minimum cross section plane near the retro-palate and the maximum cross section plane in the oropharynx are related ($r = -0.868$, $p = 0.005$), whereas there is no relationship between AHI and the area of minimum cross section.

Chapter 6 features the results of another experiment on stochastic resonance (SR) and signal-noise-ratio (SNR), conducted in order to study flow oscillation, which, by activating the dilator muscles through mechanoreceptor stimulation, may represent an additional key factor in UA occlusion. Six normal subjects and 15 OSA subjects were measured. It was found that the SR phenomenon is manifested not only in normal subjects but also in OSA subjects, and that SNR correlates with AHI. The correlation between SNR and AHI supports the hypothesis that flow oscillation is the afferent stimulus which activates the mechanoreceptors, this activation being a key factor in UA patency regulation.

The final chapter offers a brief summary of the research undertaken, together with a discussion of some possible shortfalls, and their potential remediation in future research.

Chapter 2 Methodology

The thesis employs computation fluid dynamics (CFD) in order to calculate airflow in the human UA, the results subsequently validated by experiment using fabricated physical models. Further, experimental technique on the SR phenomenon in normal and OSA subjects is discussed.

2.1 CT date acquisition

X-ray computed tomography (x-ray CT) is a common, non-invasive diagnostic method that can produce detailed 2D images of scanned objects. Radiologists using CT images can easily diagnose many diseases, such as cancer, cardiovascular disease, infectious disease, trauma and musculoskeletal disorders. There are also studies conducted using CT or MRI to diagnose medical images of the UA structures of OSA patients, yielding data as to anatomy and pathophysiology. Although neither CT nor MRI imagery alone can accurately predict surgical outcomes, some studies have demonstrated that a mandibular-hyoid distance of <20mm and the absence of retrognathia could be signs of improvement following UPPP surgery for patients with moderate OSA.

The CT scan measures the pharynx through axial slices at several levels for accurate assessment of UA area, and volumetric evaluation of the pharynx can be provided by

3D reconstruction of axial CT images. Ultrafast CT allows for higher spatial and temporal resolution with the possibility of dynamic imaging (Fig. 2.1).

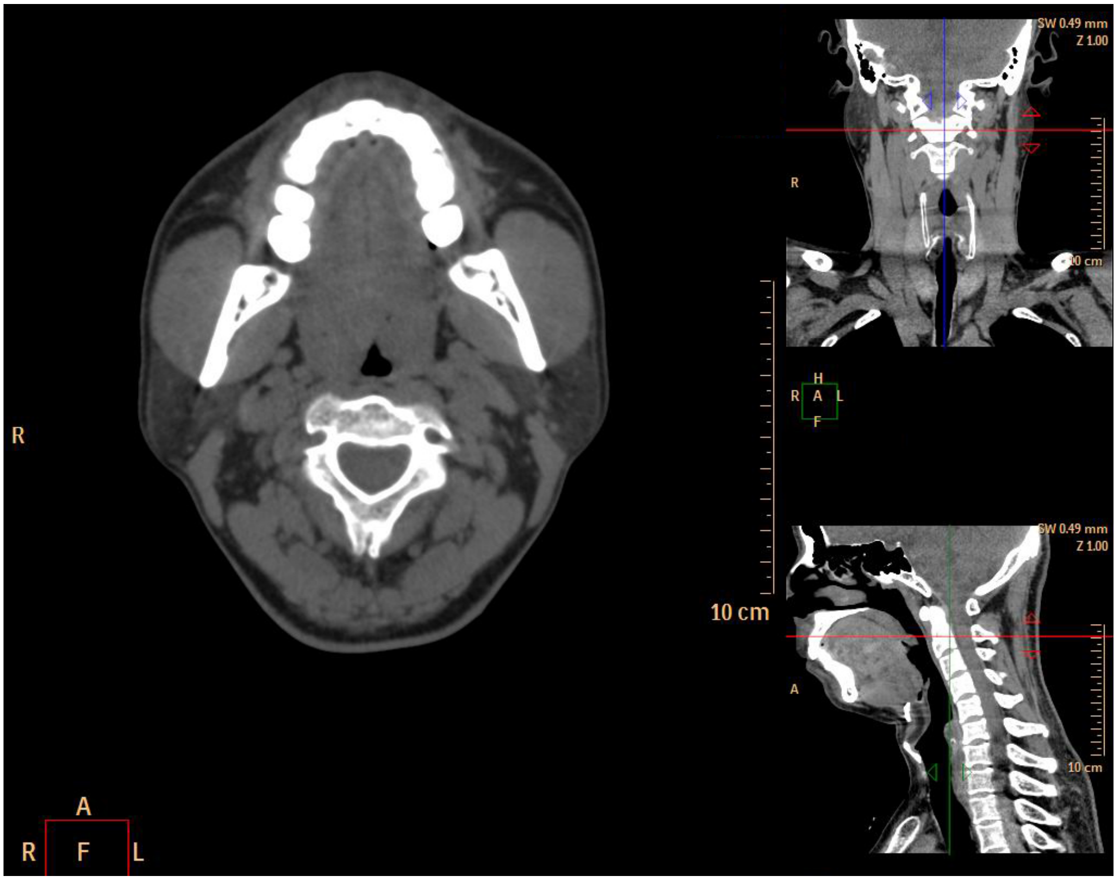

Fig.2.1. A: Coronal reconstructed view. B: Sagittal reconstructed view C Axial view.

CT scanning technology was developed on the basis of conventional x-ray examinations, by which a type of radiation penetrates the body. Since absorption coefficients vary with tissue type, conventional x-ray detectors can record an image of attenuation profiles on photographic film or a special image recording plate. For a CT scan, a number of x-ray fan beams together with a set of electronic x-ray detectors rotate around a patient. The width of the image slice accords with the selected thickness of the x-ray fan beams. Once the x-ray data has been digitized, CT reconstruction algorithms calculate the attenuated values and transfer them to a matrix of pixels (the picture element) with variegated gray values reflected in 2-dimensional cross-sections. The Hounsfield unit (HU) or CT number is a standardized and accepted unit for reporting and displaying reconstructed x-ray CT values.

$$HU = 1000 \times \frac{\mu_X - \mu_{water}}{\mu_{water} - \mu_{air}} \tag{2.1.1}$$

μ_{water}, μ_{air}, and μ_X are the linear attenuation coefficients of water, air and a substance of interest. Since the liner attenuation coefficient of air is nearly zero, a change of 0.1% of the attenuation coefficient of water could represent a change of one Hounsfield unit (HU). Thus the calibration of CT scanners is made in reference to water. The substance densities in HU are shown in Table 2.1.

Table 2.1. Substance densities in Hounsfield Units (Radiodensity).

Substance	HU
Air	-1000
Lung	-700
Soft Tissue	-300 to -100
Fat	-50
Water	0
Blood	+30 to + 45
Muscle	+40
Calculus	+100 to +400
Bone	+1000 (up to +3000 for dense bone)

The HU is the relative density of a substance (amount of X-ray radiation absorbed by each element in tissue). The gray value of each pixel in the CT image represents various densities of air and of tissue types - bone, fat, muscle, etc. For example, high density tissue such as bone and even blood appear white on the image; soft tissue shows up in shades of gray and low density air appears black. First, the scanned substance is reconstructed, with each image added in sequence until finally the whole three-dimensional UA has been built, resembling a loaf of bread cut into many slices. When the image slices are exported to processing software such as MIMICS, the UA can be reassembled as a very detailed 3D model.

Fig.2.2. Different tissues in the CT scan image.

Due to the noise and partial volume effect within the image, it is impossible to use a simple threshold to identify all airway pixels. (Reinhardt et al., 1997) First, the gray values (HU) would show interpolation when a pixel is located at the intersection of different tissues (Choi et al., 1991; Soltanian-Zadeh et al., 1993; Tardif, 2001). For example, the HU of air is generally -1000, however, the pixels across the air and airway walls typically have values well above -1,000 HU. Secondly, due to the size of the pixel and the thinness of airway, it is difficult to identify the airway wall, which may moreover appear broken or discontinuous. Finally, the image reconstruction algorithm can itself contribute to the appearance of a discontinuous airway (Kalender, 2000). All these discontinuities may result in both under-and over-segmentation errors during the extraction

2.1.1 Segmentation of CT image

To segment CT images correctly, the segmentation algorithm is defined to collect correlative pixels with homogenous characteristics. All segmentation methods are based on one theory of the approximately same gray value for one apparatus. Then the shape of an apparatus can be separated from the specific gray value in the region it occupies. Many segmentation techniques have been developed in the literature (Sonka et al., 1996; Mori et al., 1996; Schlatholter et al., 2002), but there is no single method which can be considered adequate for all images, nor can all methods be perfectly applied in a particular type of image due to noise in real circumstances. Moreover, algorithms developed for one type of image may not always be applicable to other types of image. This is particularly true when the algorithm is developed for a specific image formation model. Fortunately, most segmentation methods developed for one type of image can in fact be easily applied extended to others. Usually, to segment the

CT correctly and accurately, two or more methods are combined to segment a successful apparatus.

The two most commonly used segmentation methods - thresholding and region growing - are described in the following paragraphs.

Thresholding is a simple and effective method for images (Cheng et al., 2002). The purpose of this method is to separate objects and background into non-overlapping sets. Firstly, the critical HU value can be selected along a user defined line through one tissue. Then the pixels can be classified by assigning the value: pixels above this critical value are set as one category, and the rest are set to another. Obviously this method is quite efficient when critical peak value can be found. However, when peak value is not distinct, such as for air and the bronchi wall, it is difficult to select the critical value, which will put some pixels into the wrong set. Therefore this method is usually employed as the first coarse filter.

Region growing is a method used to identify apparatus regions occupied. This method is able to segment an apparatus based on the connectivity of gray value in a certain gray value range (Schlatholter et al., 2002; Roerdink & Meijster, 2001). It is especially suitable for segmentation of blood vessels and bronchi. For this method, the center of an area of interest should first be selected. Next to be selected are some nearby seeds from which to start growing the region selected. The method begins at each 'starting' pixel, and the neighboring pixels of seeds are examined and added to the region class if no edges are detected. For two-dimensional images, the starting pixel scans the neighboring 4/8 pixels in a circular fashion (Fig. 2.3 and 2.4). For three-dimensions, 6/26 pixels are scanned (Fig. 2.5 and 2.6). Comparing gray values, pixels with gray values that obey the following rules will be added to the seed group.

$$\left| I^* - I \right| < d \qquad (2.1.2)$$

where I^* is the average gray value, I is the new gray value, and d is the deviation.

The method repeats with the newly detected pixels as the new center seed till the edge is found and, finally, the region is constructed. This method is quite suitable for UA segmentation, due to its advantages over other segmentation techniques. Firstly, for recognition of thin airway walls, the region growing method can perfectly determine region borders, since each time only one pixel is added to the exterior of the air region. Secondly, the method is very stable with respect to noise. Lastly, the region will never contain too much of the background, so long as the deviations are defined correctly.

Although region growing is extremely fast and accurate, it is difficult to be certain of the deviation, especially for 3D region growing. If the deviation is too small, some pixels belonging to an air region cannot be selected. If the deviation is too large, the edge of the area is difficult to identify and is included in the area as seeds. The result of the misleading seeds is region leakage ("explosion") to other tissues. Therefore, only the 2D region growing method is selected in our work.

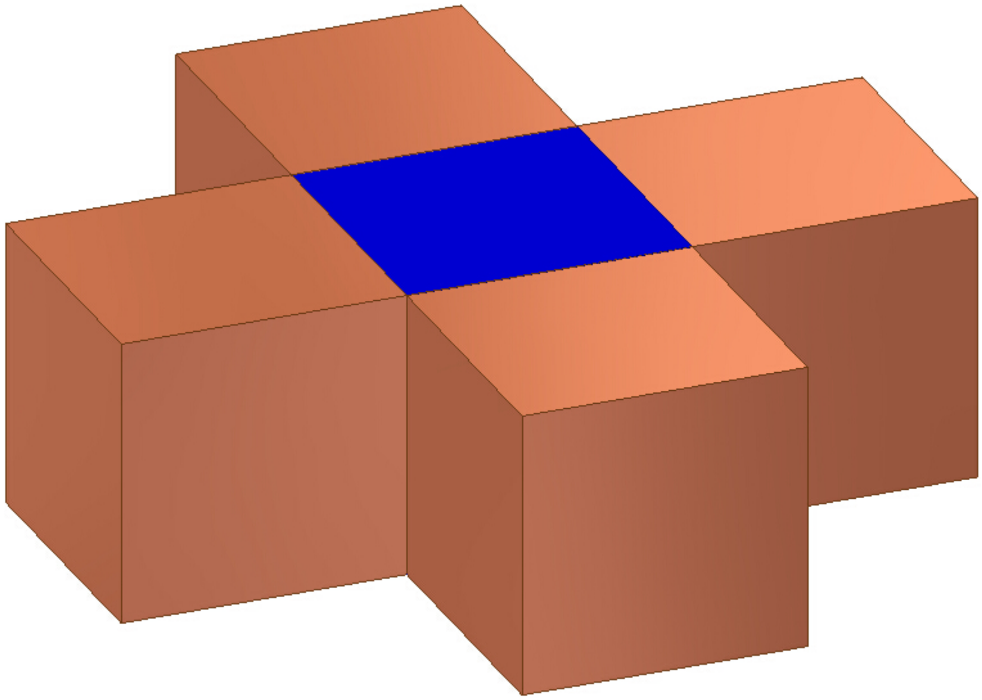

Fig 2.3. Two dimension 4 connectivity.

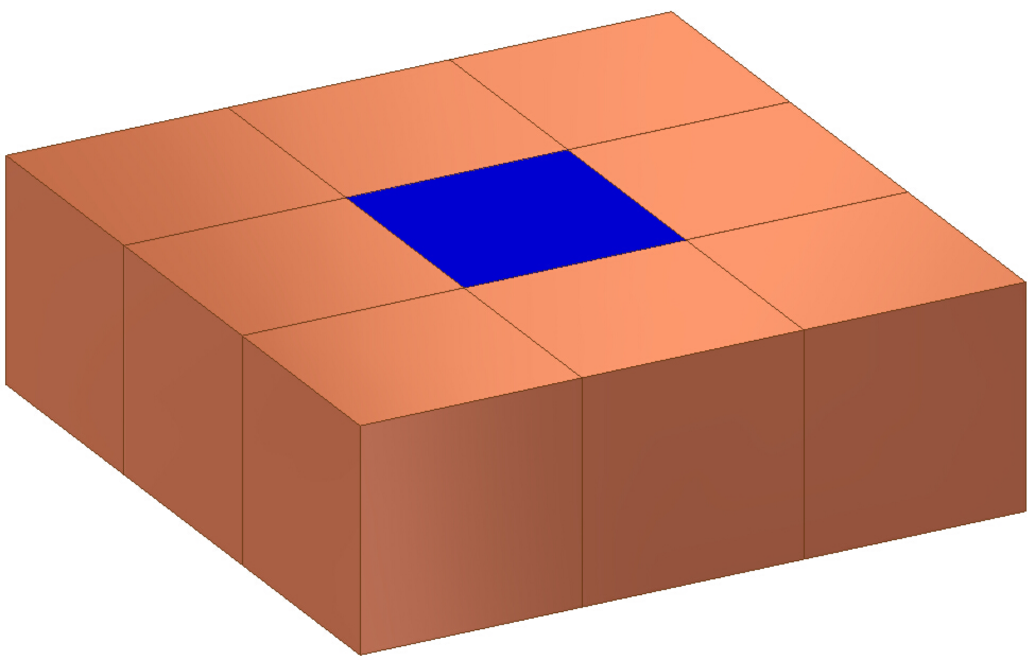

Fig.2.4. Two dimension 8 connectivity.

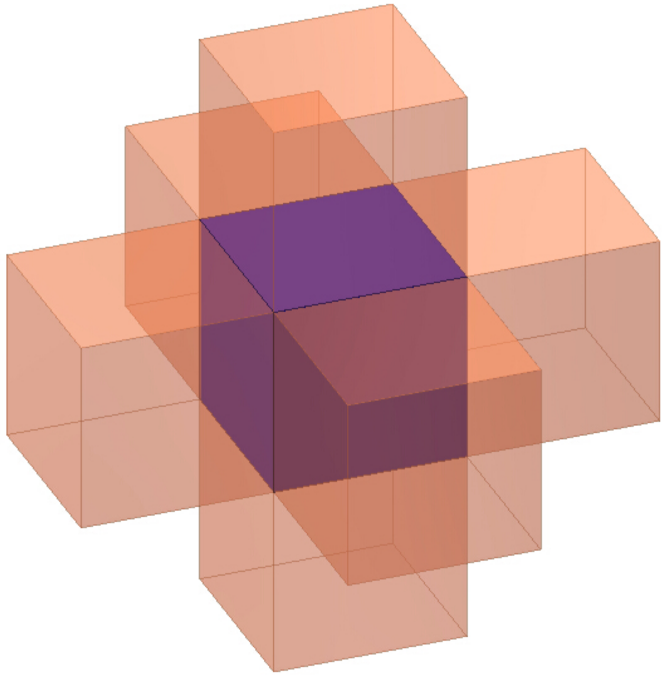

Fig.2.5. Three dimension 6 connectivity.

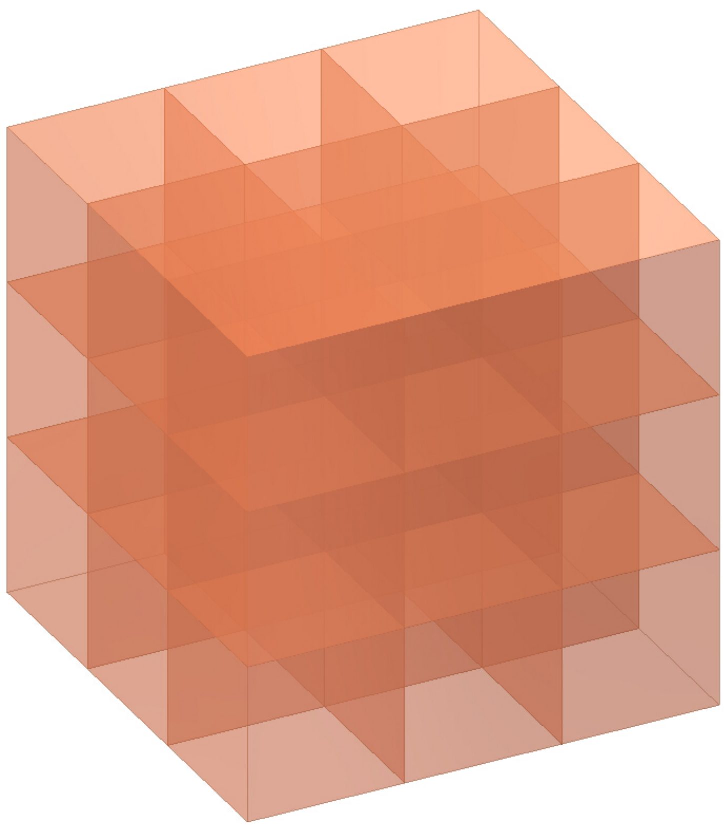

Fig.2.6. Three dimension 26 connectivity.

It should be noted that our research investigation has been approved by the local ethics committee, and is performed in accordance with the Declaration of Helsinki. The subjects were provided with written informed consent forms.

In total, four pairs of OSA patients were selected for investigation. All subjects were adult male, aged no more than 40. The treatment method was UPPP surgery. Thoracic computed tomography (CT) imaging using a single-slice helical CT scanner (Phillips, Brilliance 64) was performed in the affiliated Beijing Tongren Hospital, Capital Medical University. CT images were acquired when the patient was in supine position. The patients were awake during the entire scan process, and were instructed not to move their neck position. The table was first passed through the gantry quickly in order to find the correct starting table position for subsequent scans. The images were obtained in the axial plane with a resolution of 0.7×0.7 mm2, and slice thickness was 2 mm.

Airway extraction was performed using a combination of thresholding and region growing as discussed above. The image was first thresholded as an initial segmentation filter, that is, to clarify airway pixels from surrounding noise. After deleting noise in the images, region growing was then performed as outlined in the previous section (Fig. 2.7 and 2.8). For the region growing method, the first step is to select a serial of CT images which contain airways of interest for UA geometry extraction. When the first image is selected it is possible to zoom in on the area of interest and scale it to provide a better view of the airways. The next step is to extract airway geometry from the loaded scan images.

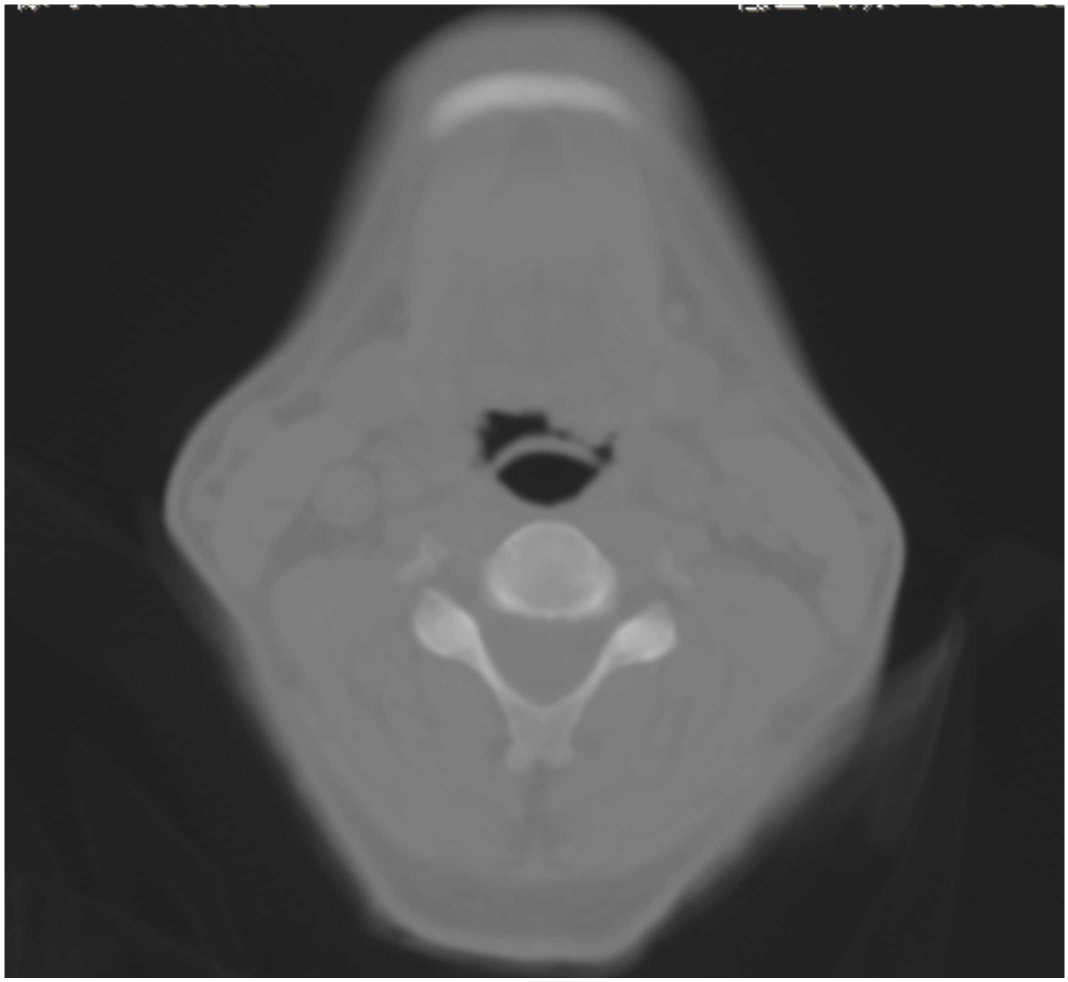

Fig.2.7 Unfiltered image.

Fig.2.8. Filtered image.

In order to designate the seed in region growing, some prior experience should be gained about airway regions to decide which region is the area of interest. This algorithm uses the concept of 8-connectedness to perform region growing.

2.1.2 Volume Reconstruction from 2D Pixel Data

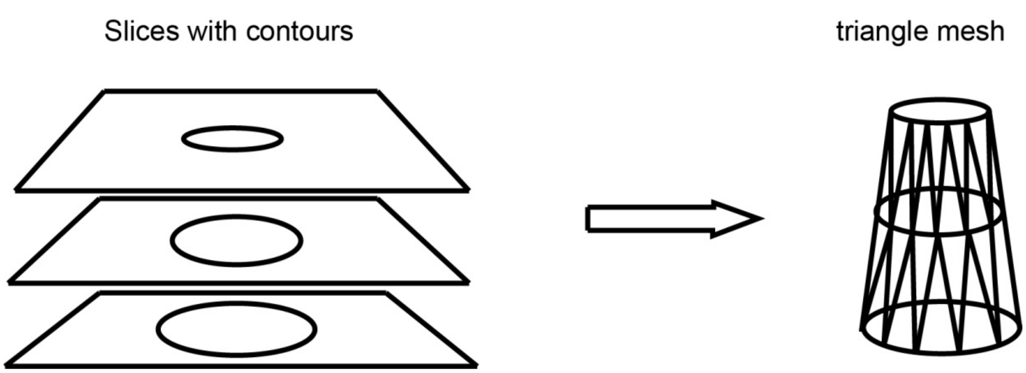

Fig.2.9. Contour oriented method.

There are many methods for volume reconstruction using 2D slice data. Our work features a simple contour-oriented method, which attempts to find the corresponding contour region in each slice, and connect the consistently oriented contour lines between adjacent slices with triangular meshes (Fig. 2.9). The advantages of this method are simplicity and high speed. The disadvantage is that if the distance between two successive slices is too large, there may be discontinuous areas from one slice to the next. In our study, due to the very small distances between slices, this disadvantage is negligible. Using this method, all the selected regions in each slice are added together so as to construct an entire UA.

Three-dimensional (3D) anatomically accurate patient models were reconstructed from CT images using the medical imaging software MIMICS (Materialise, Belgium). The entire series was loaded into MIMICS and the airway was identified in each of the axial images based on a pre-defined thresholding relative to the surrounding tissue. 3D raw models were reconstructed from the surface triangulation and then exported to REMESHER, another MIMICS module, so as to: (1) demarcate individual faces of inlet, outlet, and wall from the 3D surface model, and (2) improve the surface mesh quality by smoothing and re-meshing, in order to control maximum cell edge length and grid density. This re-meshed surface was used to generate numerical and experimental 3D volume models (Fig. 2.10).

(a)

(b)

(c)

(d)

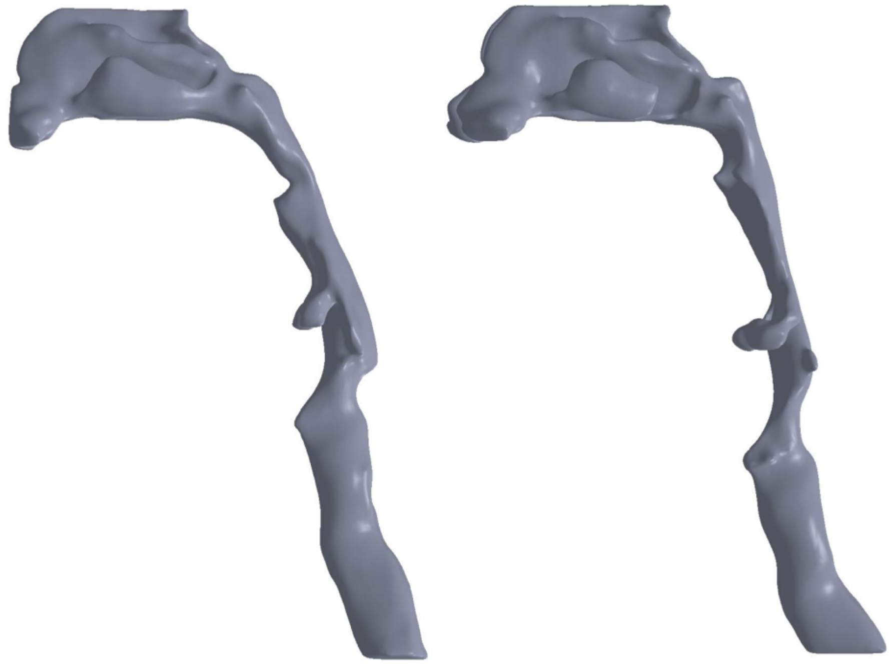

(e) (f)

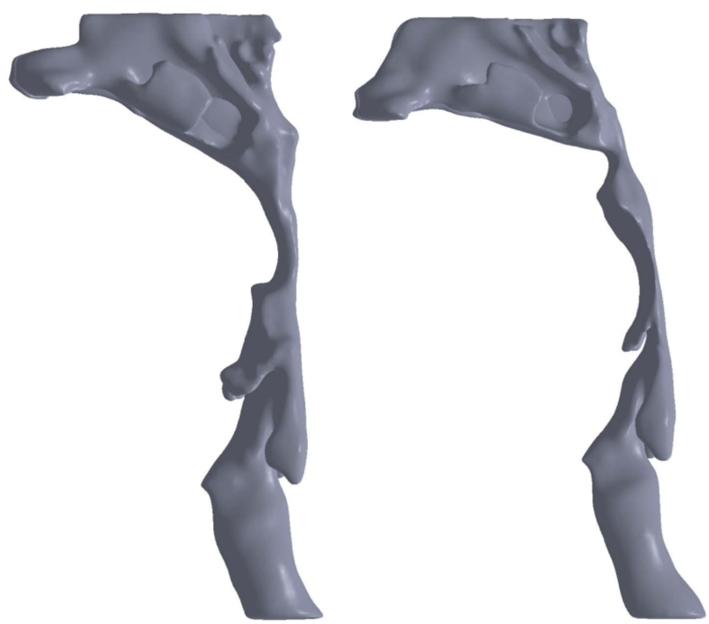

(g) (h)

Fig. 2.10. The upper airway models for four subjects: subject #1-before (a) and after surgery (b); subject #2-before (c) and after surgery (d); subject #3-before (e) and after surgery (f); subject #4-before (g) and after surgery (h).

2.2 Numerical approaches

2.2.1 The governing equations of air flow

In the present study, the working fluid is air and the airway is assumed to be rigid because it is not time-dependent. Patient-specific airway geometry is generated based on the CT data in the time of UA patency. Due to the very low Mach number (<<0.3), the airflow in the upper airway could be considered as the incompressible flow and the continuity equation and momentum equation for the unsteady flow can be written as:

$$\nabla \cdot \vec{u} = 0$$

$$\frac{\partial \vec{u}}{\partial t} + \vec{u} \cdot \nabla \vec{u} = -\frac{1}{\rho} \nabla p + \upsilon \nabla^2 \vec{u} \tag{2.2.1}$$

Where u is the velocity vector, ρ is the density, p is the static pressure and υ is the kinematic viscosity. The Reynolds number is defined as:

$$\mathrm{Re} = \frac{UD_{eq}}{\upsilon} \tag{2.2.2}$$

Where (D_{eq}) is the equivalent diameter of the cross-sectional area, U is the flow velocity computed from the bulk flow rate and υ is the kinematic viscosity of the air.

2.2.2 Numerical methods

The governing equations are non-linear partial differential equations, analytic solutions for which are very difficult to obtain. Therefore, a numerical technique for solving these differential equations is necessary. There are mainly three numerical methods for approximating the solutions to differential equations: the finite difference method (FDM), the finite element method (FEM), and the finite volume method (FVM).

The finite difference method (FDM) uses finite difference equations to substitute approximately for a derivative obtained by way of a Taylor polynomial, and was widely used in the early stages of computational fluid dynamics (CFD). FDM is intuitional and easily understandable mathematically. However, the disadvantage of FDM is that it is not suitable for an unstructured mesh or for fluid flow in complex geometries.

The finite element method (FEM) divides the continuous medium (such as components, structure, etc.) into several small pieces of elements. These small elements are reconnected by nodes, which results in a set of simultaneous algebraic equations. Approximate solutions are obtained via computation of simultaneous equations, the results sufficiently accurate for small elements when enough of them are analyzed, the disadvantage being expensive computational time.

The numerical solver employed in our study is FLUENT (ANSYS 14.5), which is based on the finite volume method (FVM). Unlike the finite difference method (FDM), the finite volume method (FVM) is based on the integral form of partial differential equations (PDE). First, the computational domain must be discretized into a series of control volumes. Then the governing equations are integrated on each control volume in order to construct a number of algebraic equations for the discrete dependent variables (velocities, pressure). Subsequently, the discrete equations are linearized to form a system of linear equations. Finally, the linear equation system is solved to obtain the updated values of the dependent variables. The continuity and momentum equations should be solved simultaneously due to the flow being depicted by these equations together. However, this coupled procedure generally requires large computational resources and it is certainly time-consuming. Since the air flow in the UA is relatively low-speed incompressible flow in which the coupling degree of velocity, pressure and density is not high, we decided to use a segregated procedure in which the governing equations are solved sequentially.

The first step in the finite volume method is obtaining equivalent integral equations to partial differential equations. Generally the N-S equations have a derivative term with respect to time in addition to the space-derivative terms, but the terms are dealt with separately using different methods. The time term is widely discretized by a method similar to FDM and the space times may be via FVM. So for a typical quantity, the integral form of the governing equation for a control volume V without time term can be written as

$$\int_S \rho\phi v \cdot \mathbf{n} dS = \int_S \Gamma \nabla\phi \cdot \mathbf{n} dS + \int_V q_\phi dV \tag{2.2.3}$$

where ρ is the density, v is the velocity vector, S is the surface area, Γ is the diffusion coefficient for ϕ, $\nabla\phi$ is the gradient of ϕ and q_ϕ is the source of ϕ per unit volume. On the left is the convectional term, and on the right the dissipative term followed by the source term.

The space in FVM is divided into several small control volumes (CVs), on which the equation (2.2.3) is discretized into an algebraic equation. There are two methods for storing data define the CV: the cell-centered scheme, in which the flow quantity is stored at the centroids of the grid cells which serve as CVs, and the cell-vortex scheme, in which the data is stored at the points of the grid cells, and the CVs are either a combination of the grid cells sharing the same point or the volume whose centroid is the point. We focus on the cell-centered scheme, more widely used in CFD. Discretization of the equation (2.2.3) on a given cell is as follows:

$$\sum_S^{N_S} \rho_S \phi_S v_S \bullet A_S = \sum_S^{N_S} \Gamma (\nabla\phi)_n \bullet A_S + q_\phi V \tag{2.2.4}$$

where NS is the number of faces close the cell, ϕ_S is the value of ϕ convected through face S, A_S is the area of face S, the multiplying term $\rho_S \phi_S v_S$ represents the mass flux through the face. $(\nabla\phi)_n$ is the magnitude of $\nabla\phi$ normal to face, and V is the cell volume. The discrete value of ϕ is stored at the cell centers. The face value ϕ_S should be interpolated from the cell center values by the upwind scheme, which means that the face value ϕ_S is derived from quantities in the upstream cell, or "upwind," relative to the direction of the normal velocity v_n in Equation (2.2.4). There are four upwind schemes for selecting: first-order upwind, second-order upwind, power law, and QUICK. When the flow is aligned with the grid, the first-order upwind discretization may be selected. When the flow is not aligned with the grid, the first-order upwind discretization increases the numerical discretization error (numerical diffusion). For triangular (2D) and tetrahedral grids (3D), since the flow is not aligned with the grid, the second-order discretization should be more accurate than the first-order discretization. Even for quad/hex grids, second-order discretization means second-order accuracy and will obtain better results especially for complex flows such as the flow in the UA.

Even the QUICK discretization scheme is quite suitable for rotating or swirling flows in which it may provide slightly better accuracy than the second-order scheme on the same mesh structure. As for the power law scheme, it generally has the same accuracy as the first-order scheme, and so in this study we select the second-order upwind scheme. The diffusion term in equation (2.2.4) is discretized by a central-differencing scheme which also is second-order accurate. Following discretization, the discrete equations should be linearized to a set of algebraic equations and then calculated numerically.

2.3 Turbulence model

Because the airflow characteristics in the OSA UA are highly complex, a different turbulence model will be adopted so as to balance accuracy and time consumption. At present, there are two methods of numerical simulation, namely direct numerical simulation (DNS) and non-direct numerical simulation.

DNS means numerical solving of N-S and continuity equations directly, with no reductions or assumptions required in the solving process. Theoretically, the data from DNS can be considered equivalent to data gained experimentally. However, when dealing with turbulent flow, in order to resolve all turbulent phenomena at all length and time scales by DNS, the smallest length, time and velocity scales need to be simulated. The size of calculation region should be capable of holding the large eddy. A huge number of grid nodes is thus required, a limiting factor on current computer technology. So only a low flow field with low Reynolds number can be simulated, which means DNS is hard to utilize for UA simulation.

The non-direct numerical simulation includes Reynolds-Averaged Navier-Stokes Simulation (RANS) and Large-Eddy Simulation (LES).

For RANS models, in which the Reynolds equation are solved for the mean velocity field. The Reynolds stresses which are unknown in the Reynolds equations, are determined by the turbulence model, either through the turbulent viscosity hypothesis (standard *k*-*ε* model, the *k*-*ω* model and the SST *k*-*ω* model) or directly from modelled

Reynolds-stress transport equations. However, these turbulence models are not adequate for predicting anisotropic flows, flows with high streamline curvature, or flows where separation occurs.

LES is a computation whereby large eddies are calculated directly, while small scale eddies are modeled. The space grid and time steps of LES are much longer than those in DNS. Hence LES is much more economical in terms of computational power required than is DNS, and is able to resolve the most energetic flow scales (entering into the inertial sub-range) and models of only the smallest dissipative scales. In human upper airway simulation, LES is a proven method for accurately capturing transitional/turbulent unsteady, separated or vortical flows (Pope 2000), and is used to reveal such relevant flow features in the flow separation region located near the minimum cross-sectional area of the airway and downstream of it (Luo et al., 2004; Mihaescu et al., 2008; Xu et al., 2006).

In the LES modeling, the filtering operation for a variable (x) is provided by:

$$\bar{\phi}(x) = \frac{1}{V}\int_V \phi(x') G(x, x') dx' \tag{2.3.1}$$

where V is the volume of a computational cell, and the filter function $G(x, x')$ is defined as:

$$G(x, x') = \begin{cases} 1 & \text{for } x' \in V \\ 0 & \text{otherwise} \end{cases} \tag{2.3.2}$$

The filtering process effectively filters out eddies whose scales are smaller than the filter width or grid spacing. Thus the filtered Navier-Stokes equations are:

$$\nabla \cdot \bar{\mathrm{u}} = 0 \tag{2.3.3}$$

$$\rho \frac{\partial \bar{\mathrm{u}}}{\partial t} + \rho \bar{\mathrm{u}} \cdot \nabla \bar{\mathrm{u}} = -\nabla \bar{P} + \mu_{eff} \nabla^2 \bar{\mathrm{u}} \tag{2.3.4}$$

where $\bar{\mathrm{u}}$ is the filtered velocity, $\bar{P}$ is the filtered pressure, t is time, and ρ is the fluid density. The μ_{eff} is the effective viscosity which is unknown and will be modeled by sub-grid scale (SGS) model.

Since the real airflow in the upper airway with OSA is transient, the results of URANS should be more accurate than the steady RANS model; therefore we compare the unsteady RANS (*k-ε*, standard *k-ω*, and *k-ω* Shear Stress Transport (SST)) and LES results with four anatomically accurate upper airway models of two OSA patients before and after surgery.

In URANS, the velocity is defined as

$$\bar{U} = \frac{1}{2T}\int_{-T}^{T} U(t)dt \tag{2.3.5}$$

$$U = \bar{U} + u''$$

where the velocity U is consisted of the mean component ($\bar{U}$) and the fluctuating component (u''). The URANS equations in incompressible form are (Lars, 2014):

$$\frac{\partial \overline{U}_i}{\partial t} + \overline{U}_j \frac{\partial \overline{U}_i}{\partial x_j} = -\frac{1}{\rho}\frac{\partial \overline{P}}{\partial x_i} + \nu \frac{\partial^2 \overline{U}_i}{\partial x_j \partial x_j} - \frac{\partial \overline{u_i^{"} u_j^{"}}}{\partial x_j}$$

$$\frac{\partial \overline{U}_i}{\partial x_i} = 0 \qquad (2.3.6)$$

where the mean dependent variables in (2.3.6) are not only a function of space, but a function of time.

$$\overline{U}_i = \overline{U}_i(x, y, z, t),\ \overline{P} = \overline{P}(x, y, x, t) \text{ and } \overline{u_i^{"} u_j^{"}} = \overline{u_i^{"} u_j^{"}}(x, y, x, t). \qquad (2.3.7)$$

From the equation 2.3.7, we can find the averaged components are still a function of time; therefore the results from URANS are unsteady.

2.4 Gradient Evaluation

Gradients are needed not only for constructing values of a scalar at the cell faces, but also for computing secondary diffusion terms and velocity derivatives. The gradient ∇φ of a given variable φ is used to discretize the convection and diffusion terms in the flow conservation equations. Most of the methods for gradient are based on the Green-Gauss theorem:

When the Green-Gauss theorem is used to compute the gradient of the scalar ϕ at the cell center c0, the following discrete form is written as

$$(\nabla \phi)_{c0} = \frac{1}{\upsilon} \sum_f \overline{\phi_f} \overrightarrow{A_f} \qquad (2.4.1)$$

where ϕ_f is the value of ϕ at the cell face centroid, computed as shown in the sections below. The summation is over all the faces enclosing the cell.

2.4.1 Green-Gauss Cell-Based Gradient Evaluation

In this method, the face value $\overline{\phi_f}$ in equation 2.4.1 is taken from the arithmetic average of the values at the neighboring cell centers, ie.,

$$\overline{\phi_f} = \frac{\phi_{c0} + \phi_{c1}}{2} \tag{2.4.2}$$

2.4.2 Green-Gauss Node-Based Gradient Evaluation

Alternatively, $\overline{\phi_f}$ can be computed by the arithmetic average of the nodal values on the face.

$$\overline{\phi_f} = \frac{1}{N_f} \sum_{n}^{N_f} \overline{\phi_n} \tag{2.4.3}$$

where N_f is the number of nodes on the face.

The nodal values $\overline{\phi_n}$ in Equation 2.4.3, are constructed from the weighted average of the cell values surrounding the nodes. This scheme reconstructs exact values of a liner function at a node from surrounding cell-centered values on arbitrary unstructured meshes by solving a constrained minimization problem, preserving a second order spatial accuracy.

The node-based gradient is known to be more accurate than the cell-based gradient, particularly on irregular unstructured meshes (skewed and distorted elements);

however, it is relatively more expensive to compute than the cell-based gradient scheme and not applicable to polyhedral meshes.

2.4.3 Least Squares Cell-Based Gradient Evaluation

In this method (Fig. 2.11) the solution is assumed to vary linearly. The change in cell values between cell c0 and ci along the vector r_i from the centroid of cell c0 to cell ci, can be expressed as

$$(\nabla\phi)_{c0} \cdot \Delta r_i = (\phi_{ci} - \phi_{c0}) \tag{2.4.4}$$

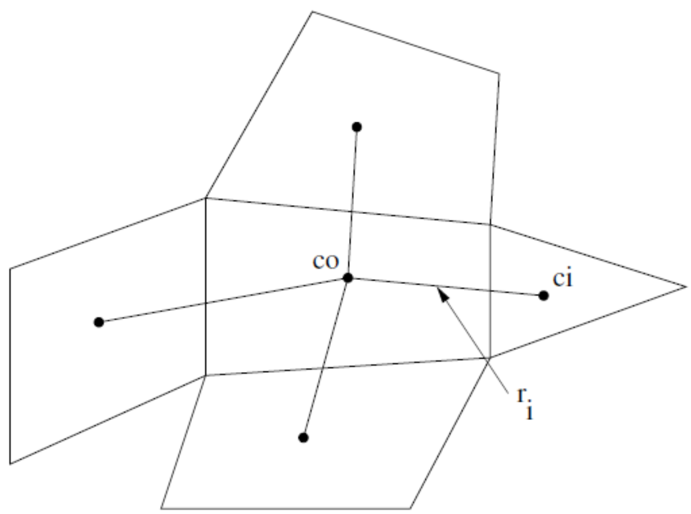

Fig.2.11. Cell centroid evaluation.

The similar equations for each cell surrounding, the cell c0 can be written as:

$$[J](\nabla\phi)_{c0} = \Delta\phi \tag{2.4.5}$$

Where [J] is the coefficient matrix, a purely geometric function.

The objective here is to determine the cell gradient $\nabla\phi_0 = \phi_x \hat{I} + \phi_y \hat{J} + \phi_z \hat{K}$) by solving the minimization problem for the system of the non-square coefficient matrix in a least-squares sense.

The above system of linear equations is over-determined and can be solved by decomposing the coefficient matrix using the Gram-Schmidt process. This decomposition yields a matrix of weights for each cell. Thus for our cell-centered scheme this means that the three components of the weight (W_{i0}^{x}, W_{i0}^{y}, W_{i0}^{z}) are produced for each of the faces of cell c0.

It is therefore possible to compute the gradient at the cell center by multiplying the weight factors by the difference vector: $\Delta\phi = (\phi_{c1} - \phi_{c0})$,

$$(\phi_x)_{c0} = \sum_{i=1}^{n} W_{i0}^{x} \cdot (\phi_{ci} - \phi_{c0}) \tag{2.4.6}$$

$$(\phi_y)_{c0} = \sum_{i=1}^{n} W_{i0}^{y} \cdot (\phi_{ci} - \phi_{c0}) \tag{2.4.7}$$

$$(\phi_z)_{c0} = \sum_{i=1}^{n} W_{i0}^{z} \cdot (\phi_{ci} - \phi_{c0}) \tag{2.4.8}$$

On irregular unstructured meshes, the accuracy of the least-squares gradient method is comparable to that of the node-based gradient (and both are much more superior compared to the cell-based gradient). However, it is less expensive to compute the least-squares gradient than the node-based gradient, though still more expensive than the cell-based gradient.

2.5 Boundary Conditions

For this complex unsteady flow, the User-Defined inlet velocity is specified normal to the boundary plane (nostril), according to the tidal volume of 700ml and the inlet nasal area. The outlet boundary condition is static pressure, which is set to zero. The outlet boundary condition is static pressure which is set to be zero. No-Slip boundary condition is imposed on all the solid walls.

The flow governing equations are discretized on the computational domain using second-order finite-volume schemes, and a second-order implicit scheme is employed for the time integration. Coupling between pressure and velocity is achieved using the SIMPLE scheme. The Wall-Adaption Local Eddy-Viscosity (WALE) model is selected as the Subgrid-Scale model for returning the correct wall asymptotic (y^3) behavior for wall bounded flows.

2.6 Experiment approaches

2.6.1 Physical model method

Rapid prototyping (RP) is a group of techniques which use three-dimensional computer aided design (CAD) data to quickly fabricate part or assembly physical models. RP is also known as: digital fabrication, 3D printing, solid imaging, solid free form fabrication, layer based manufacturing, laser prototyping, free form fabrication, and additive manufacturing. RP has been widely used in key medical specialty areas, such as orthopedic and spinal surgery, maxillofacial and dental surgeries, ancology and reconstruction surgeries, customized joint replacement prostheses, patient specific instrumentation, patient specific orthoses, implant design testing and validation and teaching tools (Bagaria et al., 2011).

In this study we choose 3D printing to generate a physical model for our experiment. 3D printing is a process which consists of making a three-dimensional physical model from a 3D printable file (STL file). Layers of materials (liquid, powder, paper or sheet material) are laid down successively in order to build the physical model from a number of cross sections under computer control (Fig. 2.12).

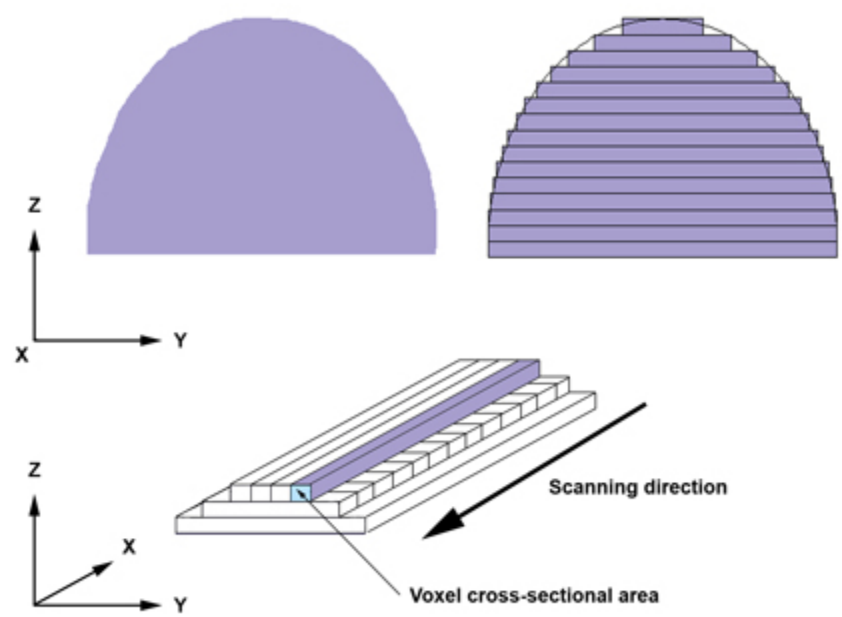

Fig. 2.12. 3D model slicing. (reprinted from wikipedia.org/wiki/3D_printing)

2.6.2 Inner velocity measurement

Two 1:1 scaled in vitro airway physical models were fabricated by a rapid prototyping method 3D printing technology (3500 HD Max-3D System, USA) which uses an engineered plastic material that provides a true look and feel for a vast array of prototyping applications. The thickness of the airway wall was a uniform 0.5 mm. Transition extension parts were added both at the inlet and outlet of the airway models to provide uniform flow outside the models.

A Laser Doppler Anemometer (LDA) system (Dantec Dynamics, Denmark) was utilized to measure the internal flow velocity of the physical airway model. Since the laser beam diameter is 2.2 mm, the velocity near the wall (about 3mm distance) could not be captured. The seeding particles were smoke generated by the Atomizer Aerosol Generator (TSI 3079) using DEHS oil and inhaled through two soft tubes into inlets (nostrils) of the airway models. Air was supplied by a pump connected to the airway outlet at the tracheal side. A flow valve was used to control the flow rate, this measured by a flow meter with a range of 0 to 30 L/min.

The selected region (orophyarnx) was cut and covered with high light transmittance plastic film to facilitate laser beam penetration while acquiring inner velocity. Experiments were performed with an inspiratory flow rate of 700mm/s (16.8L/min) followed by the numerical flow. Five start points with 1mm distance for each point were located along the posterior side of the airway wall prior to surgery. Similarly, three groups each of which included five start points were located along the posterior side of the wall after surgery. The measurement extended horizontally from a start point in the posterior side of the wall to the anterior side of the wall. The horizontal distance between points was 1.5mm and the sample time for each point was 60s.

2.7 SR phenomenon experiment

Stochastic resonance is a phenomenon whereby an optimal amount of added noise results in maximum enhancement, with further increases in noise intensity resulting only in degraded signal quality (Moss et al. 2004). This is the signature of stochastic resonance. The most common way to quantify stochastic resonance is through signal-to-noise ratio (SNR). This is readily obtained from the output by forming a power spectrum which measures the frequency content of a time series (Wiesenfeld and Moss 1995). The power spectral density (PSD) exhibits the power at a certain frequency but cannot indicate quality of signal. The signal quality can be evaluated by SNR, which is a measure that compares the level of a desired signal to the level of background noise. As shown in Fig. 2.13, the SNR is defined in decibels (dB)

$$SNR = 10\log_{10}\left(\frac{S}{N_0}\right) \tag{2.6.1}$$

where S is the area enclosed above the noise background (the pink area) and N0 is the average intensity of noise background at the signal frequency (Wiesenfeld and Moss 1995). Because we have found that the volitional breathing has a much higher level of PSD over a wider frequency range, while the PSD of spontaneous breathing peaks is around 5 Hz (Liu et al. 2012), we here select identifiable peaks around 5 Hz to compute the SNR value for each subject.

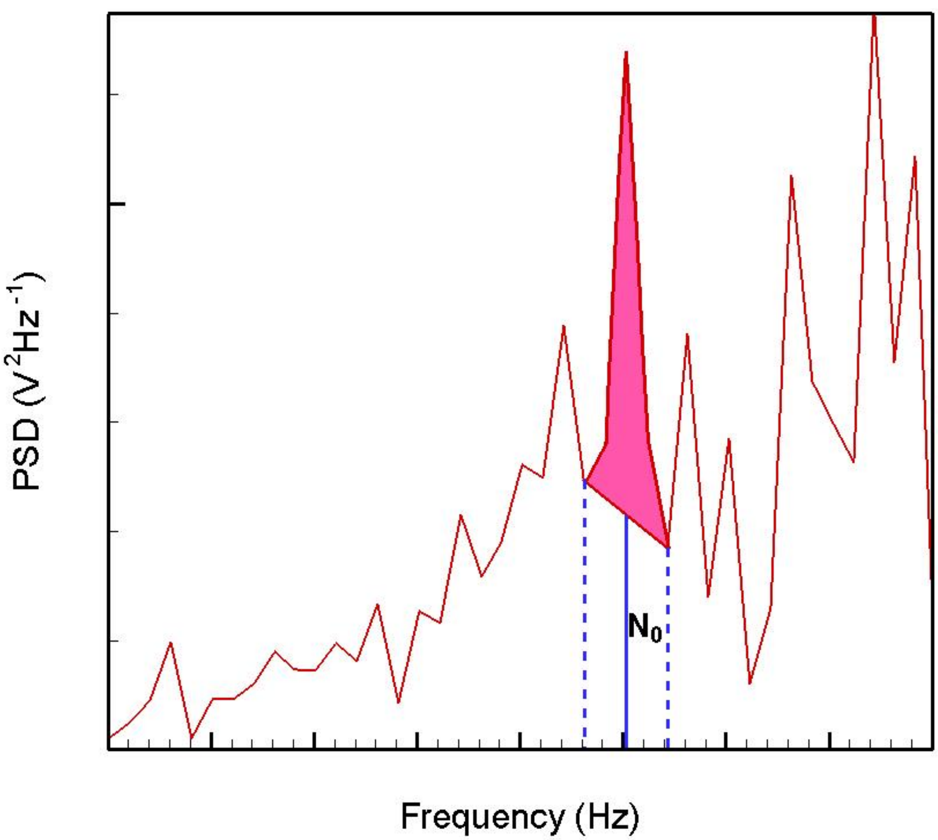

Fig. 2.13. The diagram of SNR calculation with power spectrum, the pink area is the area enclosed above the noise background and N_0 (blue solid line) means the average intensity of noise (two blue dotted line) background at the signal frequency.

.

Chapter 3 The effect of turbulent models on flow simulation in upper airway models with obstructive sleep apnea

Due to the complex morphology of the upper airway region, the flow is expected to be turbulent in the model. There are three approaches for simulation of turbulent flows, i.e., direct numerical simulation (DNS), large-eddy simulation (LES), and Reynolds-averaged Navier-Stokes (RANS) models. DNS is the most accurate technique and resolves turbulent eddies at all scales (Pope, 2003), but it is too expensive to simulate the upper airway turbulent flows. RANS does not resolve any turbulent eddy structures and uses a turbulence model to predict the dynamics of these eddies. It is based on a time averaging of the flow field, and cannot capture the flow field unsteadiness that is particularly important in case of internal flow separation in complex regions (Wilcox, 1998). LES divides the flow field into large and small scales by a filtering procedure. It can directly solve the equations that describe the evolution of a large range of turbulence scales, only the smallest scales are modeled by LES using Sub-Grid-Scale (SGS) models.

Several researchers studied the flow in human upper airway and lung airways (Ball, et al., 2008; Freitas & Schröder, 2008; Luo & Liu, 2008; Luo, et al., 2007; Große, et al., 2007; Lin, et al., 2007). Nithiarasu et al. (2008) studied the steady flow through a realistic upper airway and found large shear and pressure forces in the oropharynx and laryngopharynx. They suggested that these locations should be the focus of any study aimed at understanding human upper airway collapse in a patient-specific manner. Xu et al. (2006) carried out CFD simulation of the upper airway of children with OSA in steady flow. Model geometry was reconstructed from magnetic resonance images (MRI) obtained during quiet tidal breathing, and the unsteady Reynolds-averaged Navier-Stokes equations were solved with steady flow boundary conditions in inspiration and expiration, using a two-equation low-Reynolds number turbulence model. The results suggested that pharynx pressure drop strongly correlated to airway area restriction, and that pharyngeal airway shape in children with OSA significantly affected internal pressure distribution compared to nasal resistance. Sung et al. (2006) and Jeong et al. (2007) conducted numerical investigation on the flow characteristics and aerodynamic force of the upper airway of patients with OSA using CFD. To produce the important transition from laminar to turbulent flow in the pharyngeal airway, they adopted the low Reynolds number k- ω model, and found the flow comprised a turbulent jet formed by area restriction at the velopharynx. This turbulent jet caused higher shear and pressure forces in the vicinity of the velopharynx. They deduced that the most collapsible area in the pharyngeal airway of OSA patients is the velopharynx, where exist minimum intraluminal pressure and maximum aerodynamic force.

Mandibular advancement devices (MADs) bring the mandibula forward in order to increase upper airway volume and prevent total upper airway collapse during sleep. Recently, De Backer et al. (2007) examined whether an upper airway model that combines imaging techniques and CFD allows for a prediction of the treatment outcome with MADs. In a sample of 10 patients the change in upper airway volume was investigated by means of computed tomography (CT) scans. CFD simulation was based on a patient specific geometry and patient specific boundary conditions. The results indicated that a decrease in upper airway resistance and an increase in upper airway volume correlate with both a clinical and an objective improvement. They concluded that the outcome of MADs treatment can be predicted using CFD simulation.

Mihaescu et al. (2008a) used CFD to study the effect of an adenotonsillectomy on the flow behavior in the upper airway of a 15-year-old obese girl. They performed both pre- and post-surgical analyses to assess the influence of the alterations in upper airway morphology. They found that the resolution of OSA after adenotonsillectomy is associated with changes in flow characteristics that result in decreased pressure differentials across the airway walls and thus lower compressive forces that predispose to airway collapse. The researchers concluded that patient specific functional imaging using CFD could lead to a useful clinical tool in pre-operative planning procedure.

Yu et al. (2009) numerically simulated the flow fields of narrowed upper airways of two patients with OSA treated with maxillomandibular advancement. The geometry of the upper airway was reconstructed from CT scan images taken before and after surgery. The simulated results showed a less constricted upper airway, with less velocity change and a decreased pressure gradient across the whole conduit during passage of air. Less breathing effort is therefore expected to achieve equivalent ventilation with the postoperative airway. They concluded that CFD is capable of providing information for understanding the pathogenesis of OSA and the effects of its treatment. There are different views on RANS and LES for the flow simulation in human airways. Several researchers carried out CFD studies to analyze the flow in MRI/CT based upper airway models of patients with OSA (Xu, et al., 2006; Sung, et al., 2006; Jeong, et al., 2007; De Backer, et al., 2007; Vos, et al., 2007). In all these studies the CFD analyses were mostly based on RANS solvers using two-equation turbulence models. De Backer et al. (2007) explained that the low Reynolds number (LRN) k-ω model could accurately predict pressure drops and velocity profiles in the upper airway; in particular, the model is able to obtain an accurate laminar solution when turbulent viscosity approaches zero (Wilcox, 1998). Mihaescu et al. (2008b) compared the LES and RANS simulation of flow in a realistic pharyngeal airway, and gave a contrary conclusion. In their study, both the k-ε and k-ω two equation models were used in the steady RANS model, and they concluded that steady RANS may not be the proper tool to investigate flow in human airways. They further commented that, in contrast with steady RANS, LES can provide an increased level of detail and accuracy for unsteady, separated, or vortical turbulent flow situations, and that LES should be the preferred tool for capturing relevant flow features in the flow separation region located near the minimum cross-sectional area of the airway and downstream of it. In our previous study (Liu, et al., 2012), we found that the flow oscillation induced by flow separation at the larynx plays an important role in activating the mechanoreceptors in the upper airway, which is crucial for OSA subjects. We compared the flow patterns using both LES and URANS models in four OSA upper airway models for both pre- and post-surgery treatment. The results would provide useful guidance for OSA upper airway simulation and have significant influence on surgery planning.

3.1 Numerical models

Since real airflow in the upper airway with OSA is transient, the results of URANS should be more accurate than with the steady RANS model; therefore we compare the unsteady RANS (k-ε, standard k-ω, and k-ω Shear Stress Transport (SST)) and LES results with four anatomically accurate upper airway models of two OSA patients before and after surgery. The details of URANS and LES models have been discussed in chapter 2.

In this study, four upper airway models of two severe OSA subjects (Fig. 3.1) for both pre- and post- surgery are reconstructed using the Mimics^{TM} based on CT images (Figure 3.1) (Luo & Liu, 2008; Liu, et al., 2012). Severity of OSA is defined by the apnea-hypopnea index (AHI), which indicates the number of apneas and hypopneas per hour. The AHI for the four OSA models is tabulated in Table 3.1. Prior to surgery, both subjects suffered from severe OSA; after treatment, the AHI decreased significantly to 15.8 (Mild) for subject #1 and 23.9 (Moderate) for subject #2.

Table 3.1. AHI measurement of OSA subjects.

Samples	Before surgery	After surgery
Subject #1	69	15.8
Subject #2	60.7	23.9

The simulations were carried out with Fluent (ANSYS 14.5). We attempt to study the inspiratory process with a tidal volume of 700 ml and a breathing frequency of 12 cycles per minute following a sinusoid. Airflow is assumed as incompressible flow due to the very low Mach number. Second-order finite-volume schemes were employed for discretization of the flow governing equations in the computational domain. While time-integration was performed using second-order implicit discretization, coupling between the pressure and the velocity field was implemented through the SIMPLE algorithm. Initial velocity was calculated according to nostril area. The pressure boundary condition in the outlet was set at zero. No-slip boundary condition was applied on the surface of the whole airway and the time step was set at 0.001s. The WALE sub-grid scale (SGS) model was employed in the LES calculations.

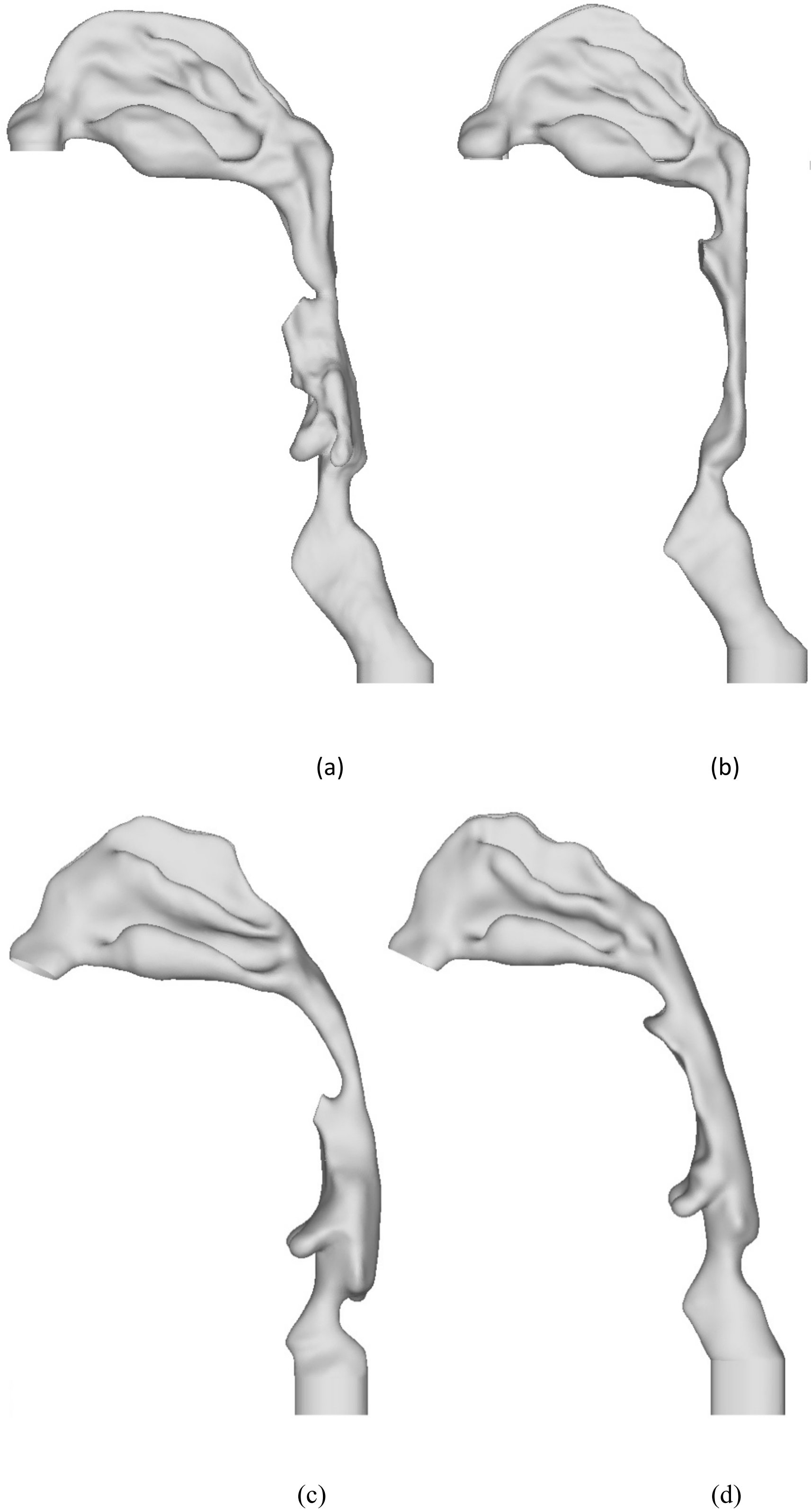

Fig.3.1. The upper airway models: (a) subject #1-before surgery; (b) subject #1-after surgery; (c) subject #2-before surgery; (d) subject #2-after surgery.

3.2 Mesh convergency

The mesh was generated using ICEM (ANASYS 14.5). The meshes are hybrid hexahedral/tetrahedral elements and a refined mesh was employed near the wall (Fig. 3.2). Mesh convergency was tested by use of three different mesh sizes for the model of subject #2 after surgery. Cell quantity was about 840,000, 2,600,000 and 3,800,000 respectively for grid 1, grid 2 and grid 3. Fig. 3.3 shows the axial velocity time series at a point near the oropharynx, and the discrepancy between grid 2 and grid 3 is quite small. Therefore a cell quantity of ~ 2,600,000 was selected for this study.

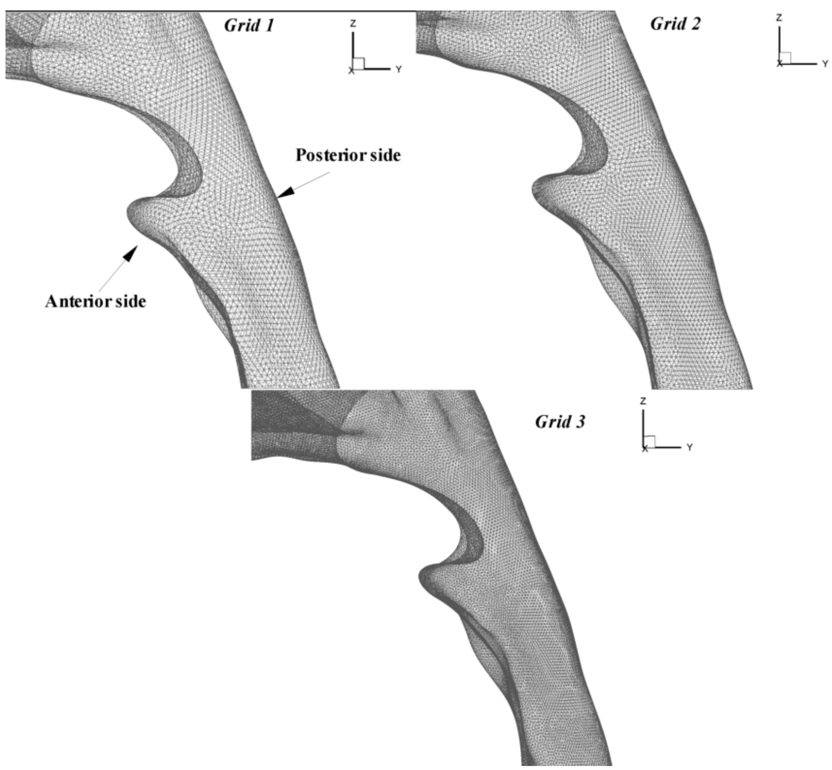

Fig.3.2. Side view details of the different refined computational grids at the region of the minimum cross-sectional area from the coarsest mesh (*Grid* 1), intermediate mesh (*Grid* 2) and the finest mesh (*Grid* 3).

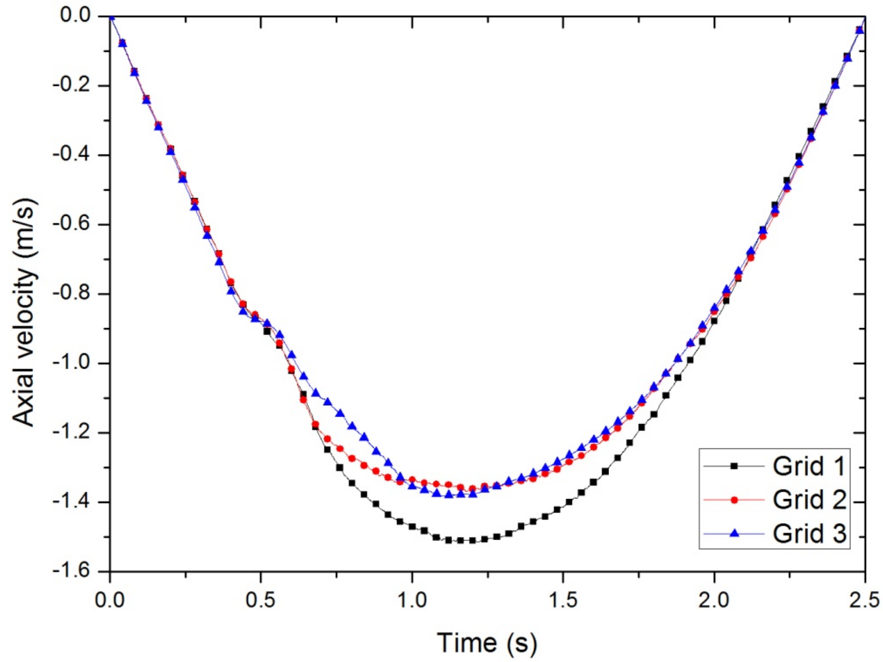

Fig.3.3. Grid sensitivity of the axial velocity in the detected point at the minimum cross-sectional area for a period.

3.3 Flow patterns

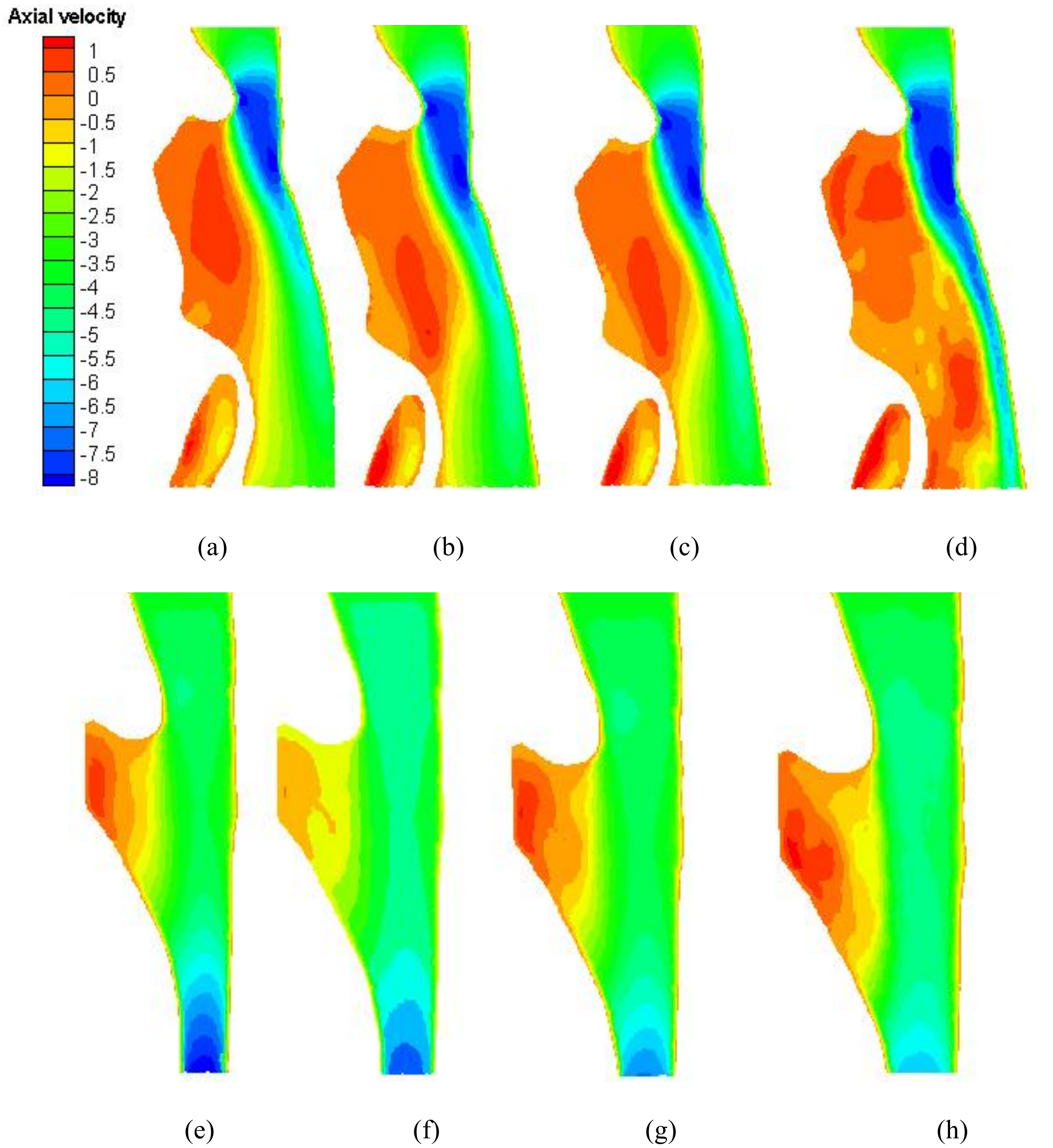

Fig.3.4. Axial velocity distribution (m/s) in the sagittal plane: (a) RANS (k-ε) solution before treatment; (b) RANS (standard k-ω) solution before treatment; (c) RANS (k-ω SST) solution before treatment; (d) LES solution before treatment; (e) RANS (k-ε) solution after treatment; (f) RANS (standard k-ω) solution after treatment; (g) RANS (k-ω SST) solution after treatment; (h) LES solution after treatment.

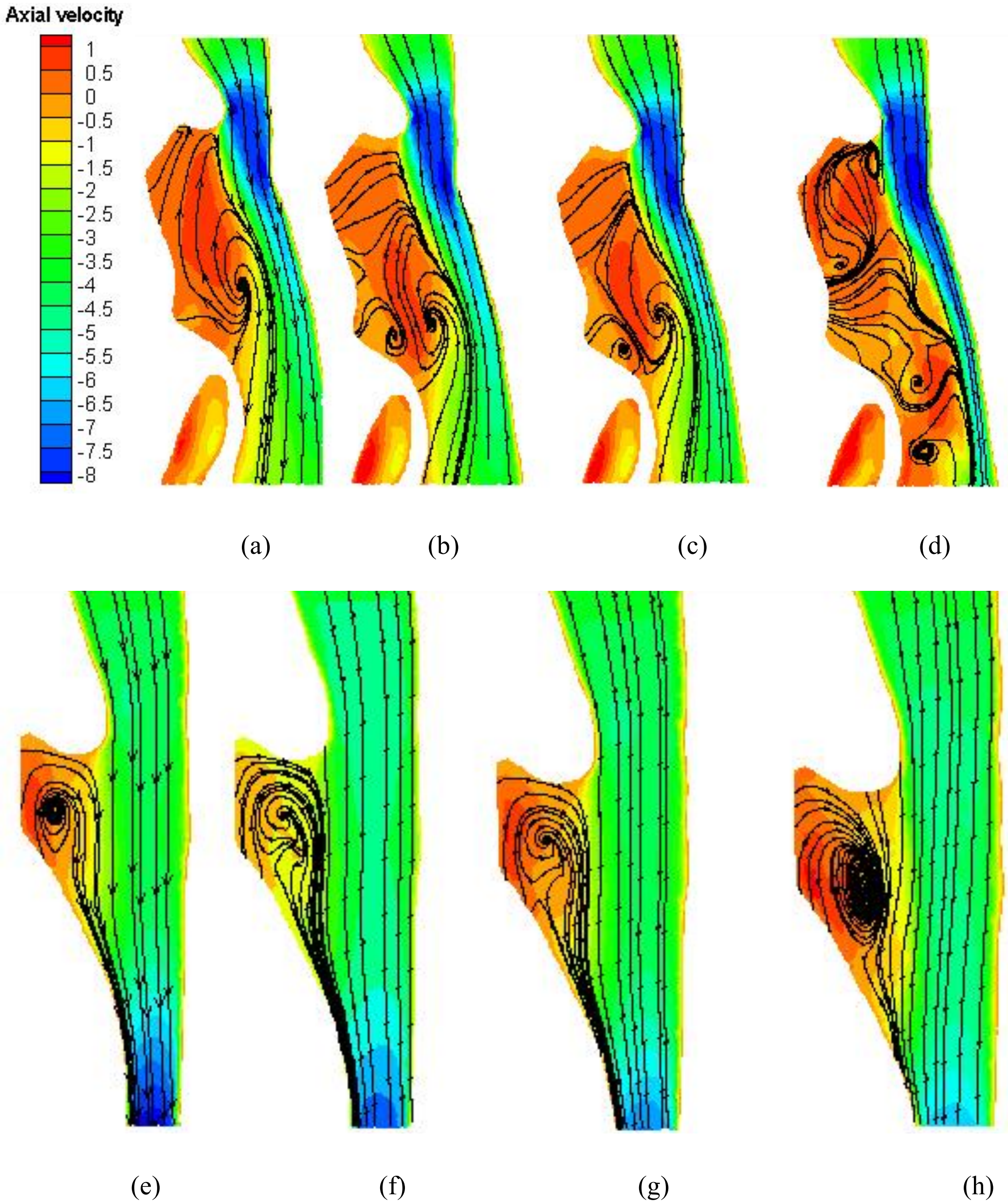

Fig.3.5. Axial velocity streamlines distribution (m/s) in the sagittal: (a) RANS (k-ε) solution before treatment; (b) RANS (standard k-ω) solution before treatment; (c) RANS (k-ω SST) solution before treatment; (d) LES solution before treatment; (e) RANS (k-ε) solution after treatment; (f) RANS (standard k-ω) solution after treatment; (g) RANS (k-ω SST) solution after treatment; (h) LES solution after treatment.

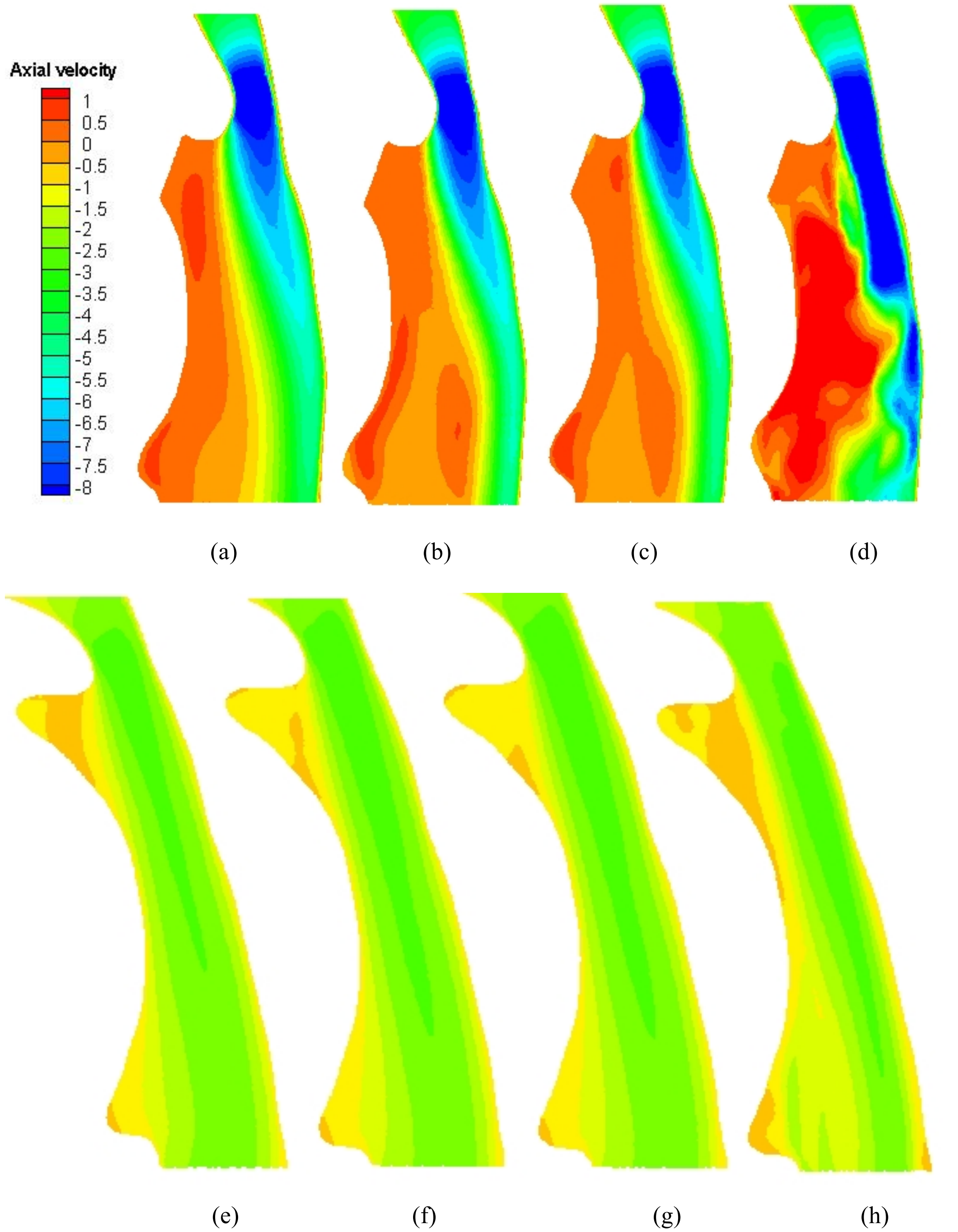

Fig.3.6. Axial velocity distribution (m/s) in the sagittal plane: (a) RANS (k-ε) solution before treatment; (b) RANS (standard k-ω) solution before treatment; (c) RANS (k-ω SST) solution before treatment; (d) LES solution before treatment; (e) RANS (k-ε) solution after treatment; (f) RANS (standard k-ω) solution after treatment; (g) RANS (k-ω SST) solution after treatment; (h) LES solution after treatment.

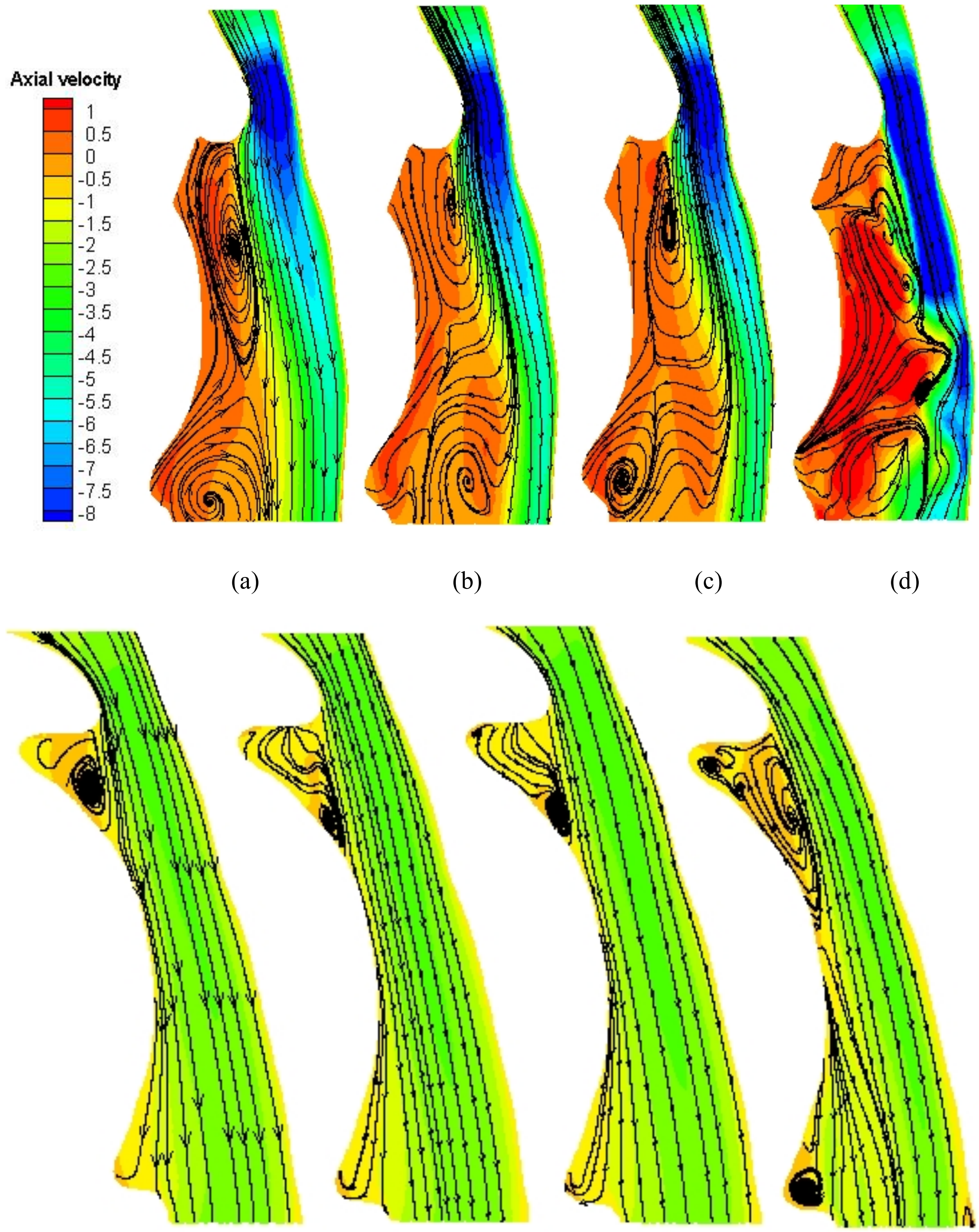

Fig.3.7. Axial velocity streamlines distribution (m/s) in the sagittal: (a) RANS (k-ε) solution before treatment; (b) RANS (standard k-ω) solution before treatment; (c) RANS (k-ω SST) solution before treatment; (d) LES solution before treatment; (e) RANS (k-ε) solution after treatment; (f) RANS (standard k-ω) solution after treatment; (g) RANS (k-ω SST) solution after treatment; (h) LES solution after treatment.

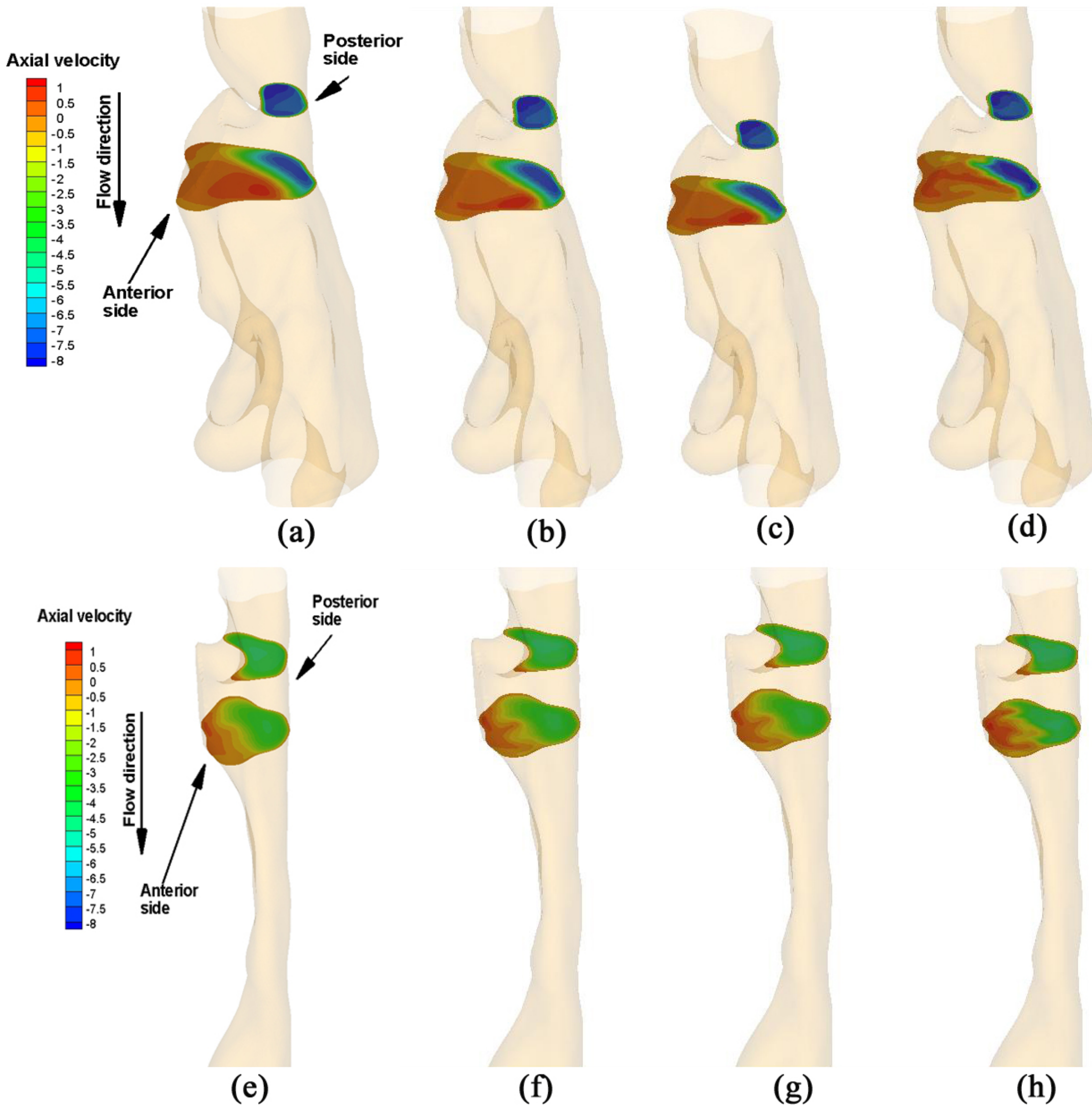

Fig.3.8. Axial velocity distribution (m/s) of the minimum cross-sectional plane (higher) and its downstream cross-sectional plane (below): (a) RANS (k-ε) solution before treatment; (b) RANS (standard k-ω) solution before treatment; (c) RANS (k-ω SST) solution before treatment; (d) LES solution before treatment; (e) RANS (k-ε) solution after treatment; (f) RANS (standard k-ω) solution after treatment; (g) RANS (k-ω SST) solution after treatment; (h) LES solution after treatment.

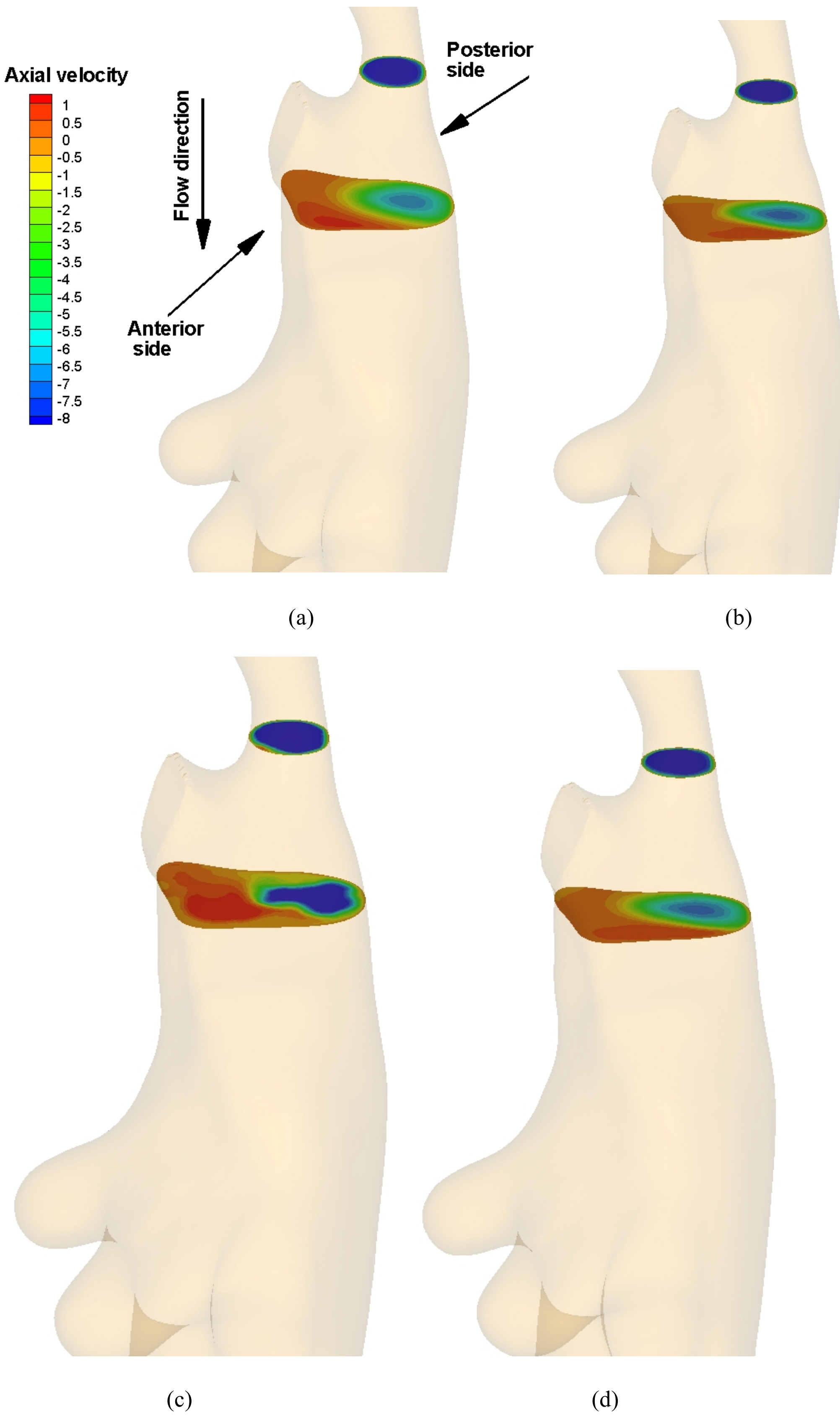
Axial velocity
1
0.5
0
-0.5
-1
-1.5
-2
-2.5
-3
-3.5
-4
-4.5
-5
-5.5
-6
-6.5
-7
-7.5
-8
Flow direction
Posterior side
Anterior side
(a)
(b)
(c)
(d)

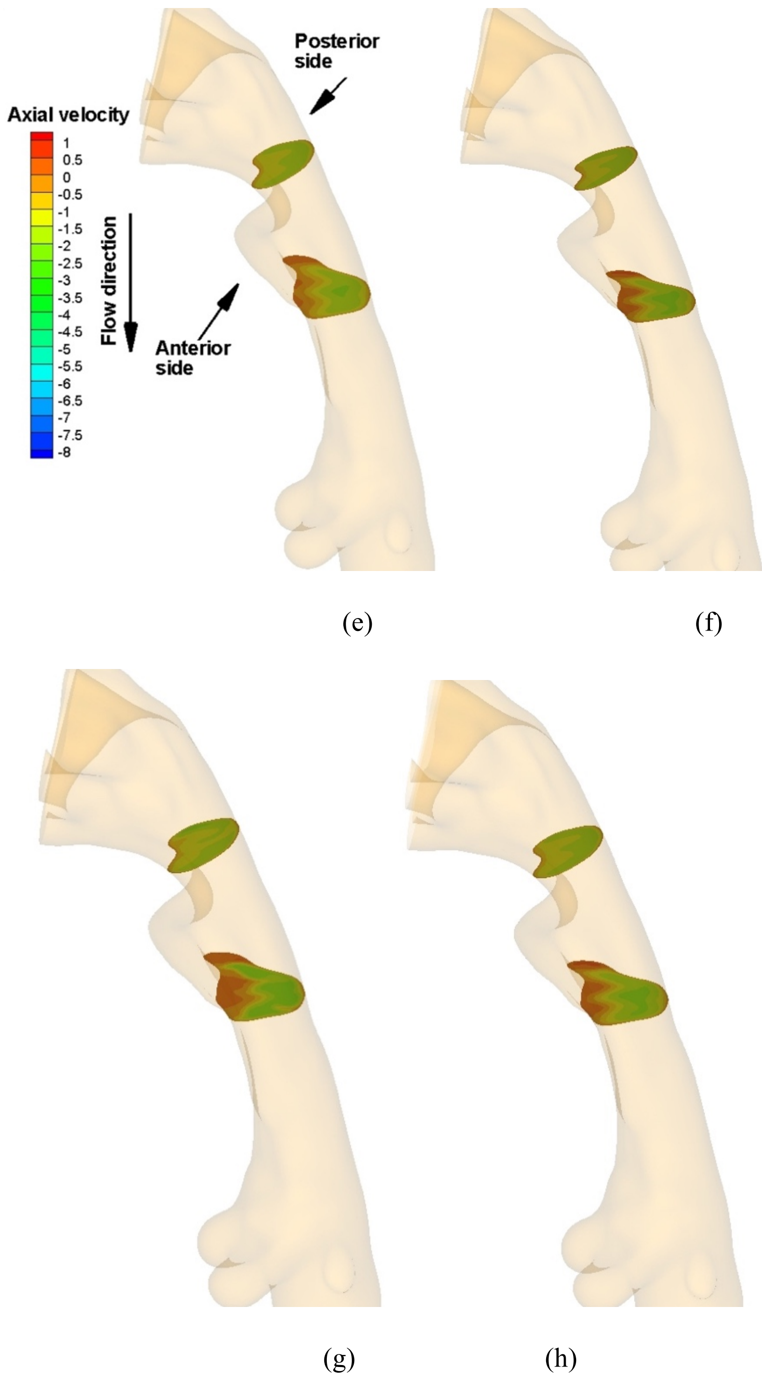

Fig.3.9. Axial velocity distribution (m/s) of the minimum cross-sectional plane (higher) and its downstream cross-sectional plane (below) subject #2: (a) RANS (k-ε) solution before treatment; (b) RANS (standard k-ω) solution before treatment; (c) RANS (k-ω SST) solution before treatment; (d) LES solution before treatment; (e) RANS (k-ε) solution after treatment; (f) RANS (standard k-ω) solution after treatment; (g) RANS (k-ω SST) solution after treatment; (h) LES solution after treatment.

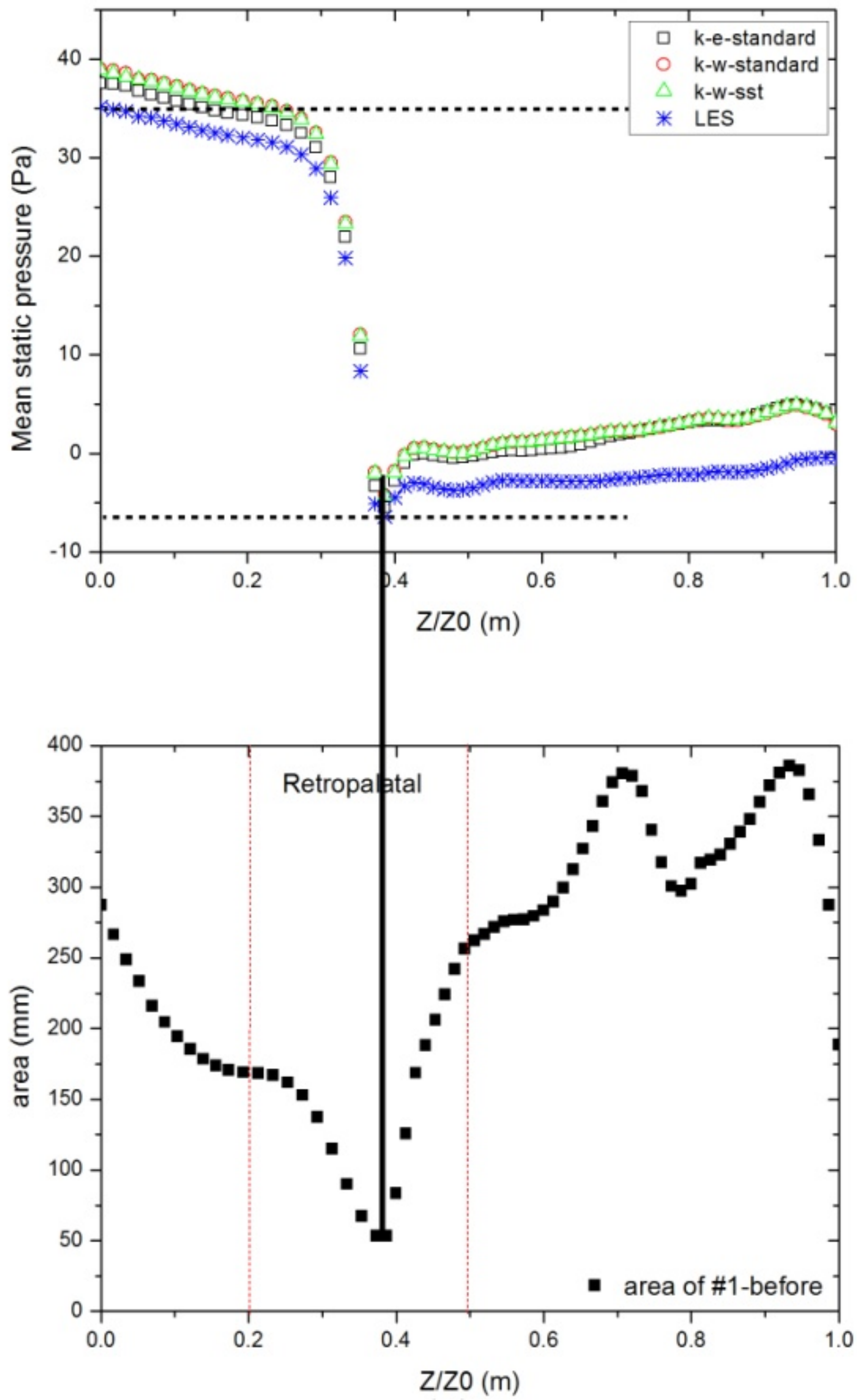

k-e-standard
k-w-standard
k-w-sst
LES
Mean static pressure (Pa)
Z/Z0 (m)
Retropalatal
area (mm)
area of #1-before
Z/Z0 (m)

(a)

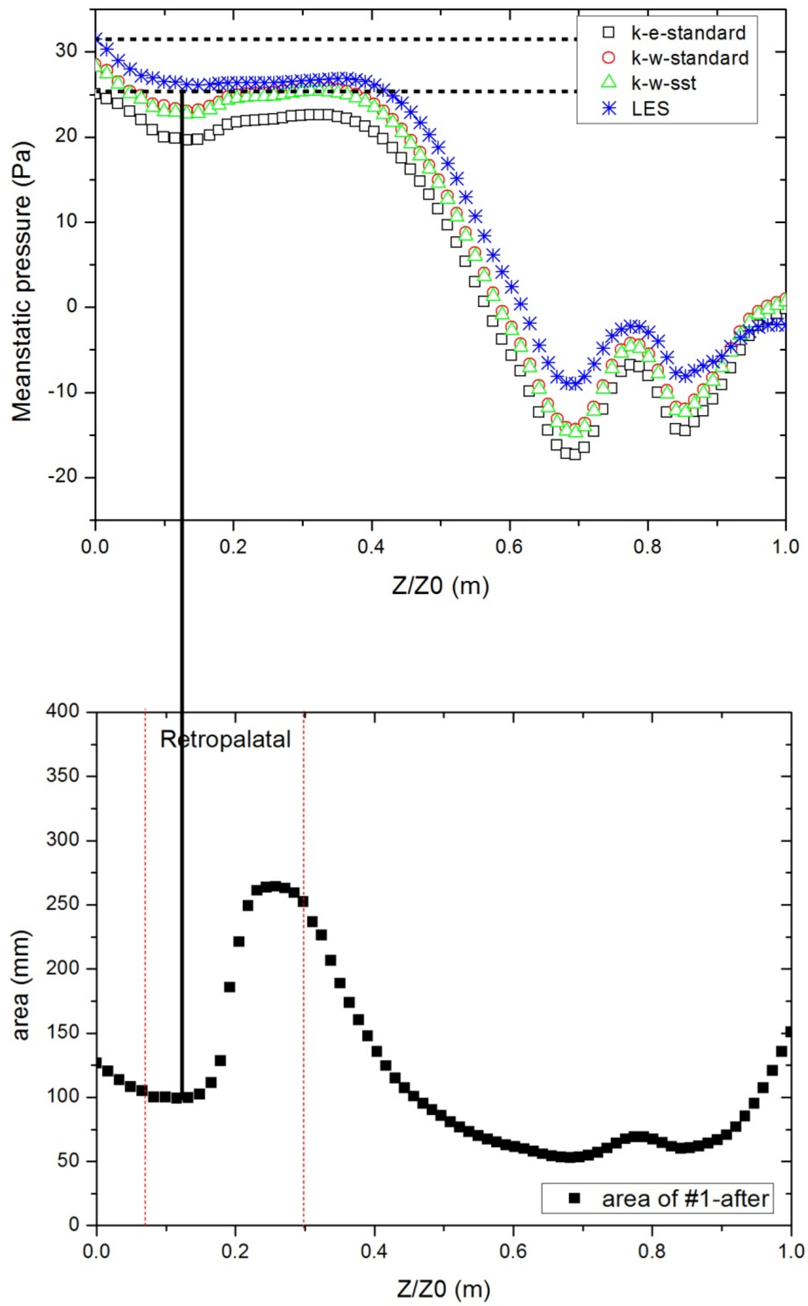

(b)

Fig.3.10. LES and URANS comparisons of cross-sectional area and mean static pressure distribution from nasopharynx to epiglottis for subject #1: (a) before surgery and (b) after surgery.

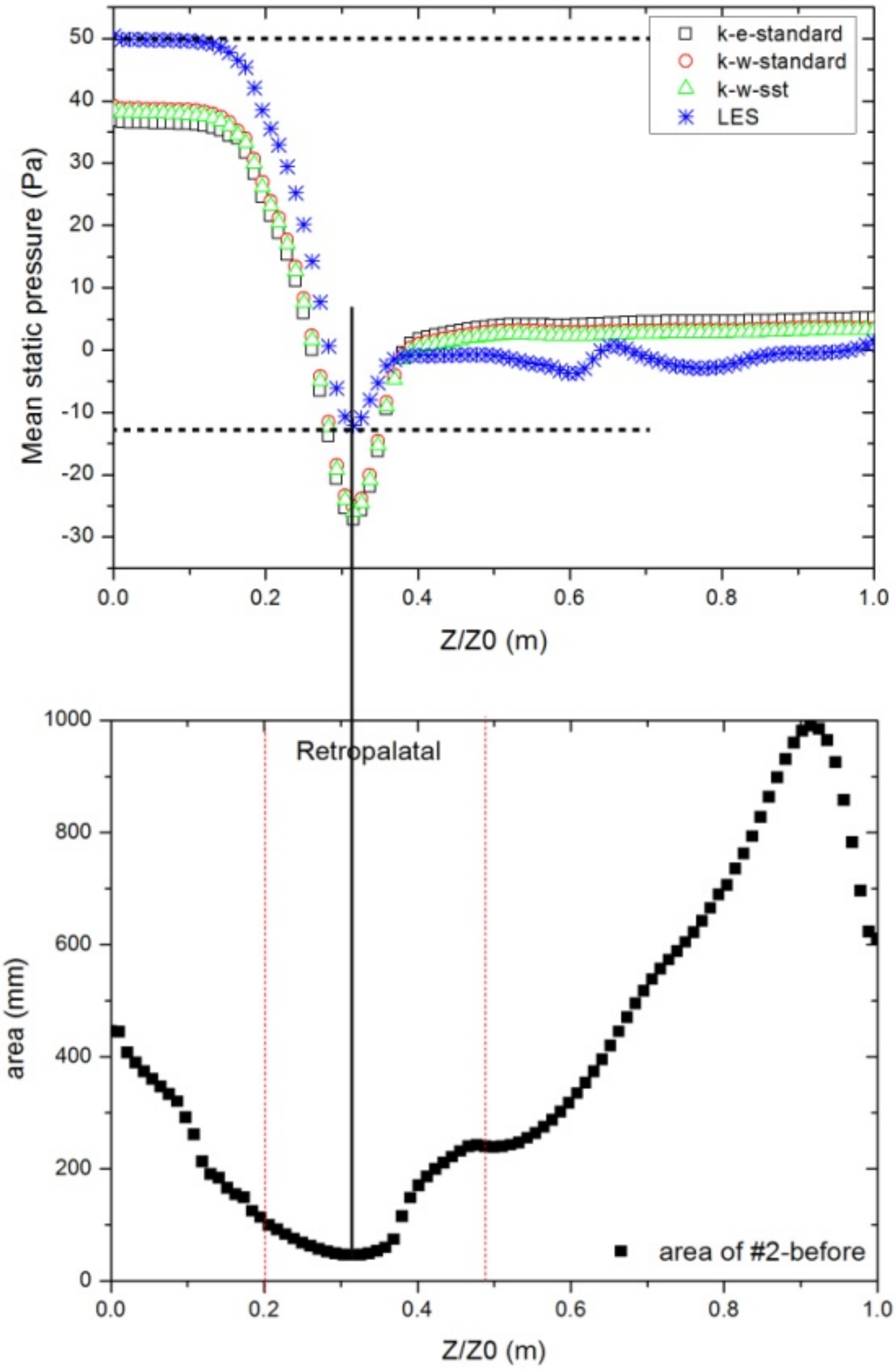
k-e-standard
k-w-standard
k-w-sst
LES
Mean static pressure (Pa)
Z/Z0 (m)
Retropalatal
area (mm)
area of #2-before
Z/Z0 (m)

(a)

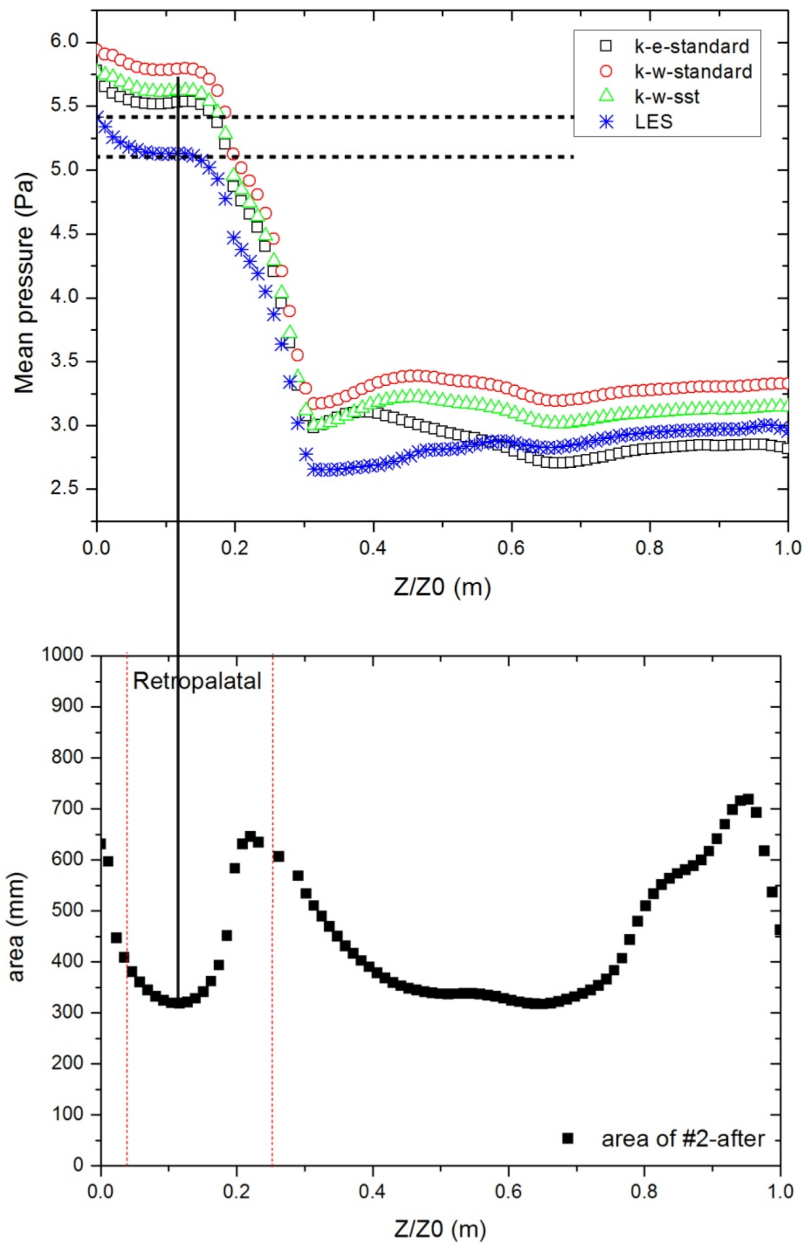

(b)

Fig.3.11. LES and URANS comparisons of cross-sectional area and mean static pressure distribution from nasopharynx to epiglottis for subject #2: (a) before surgery and (b) after surgery.

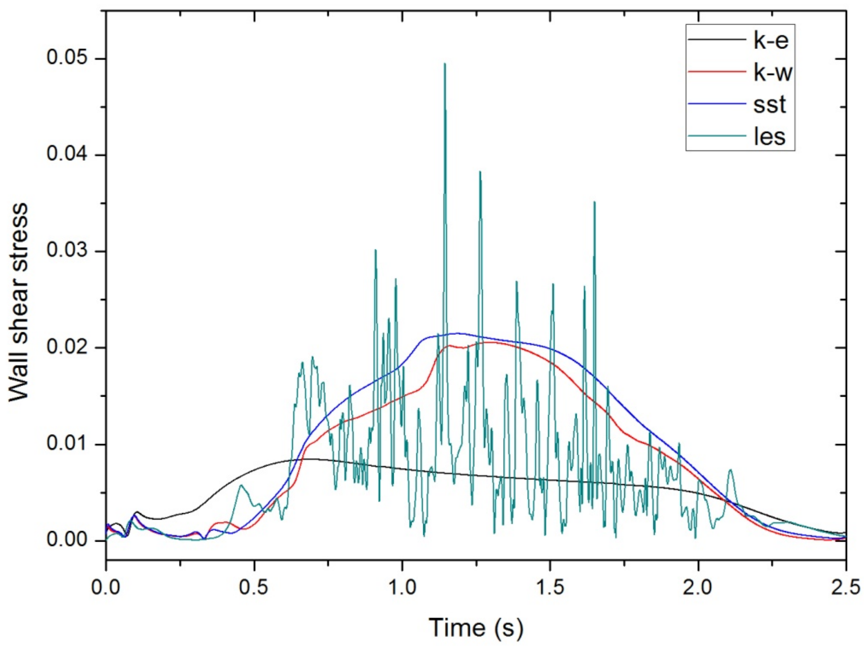

(a)

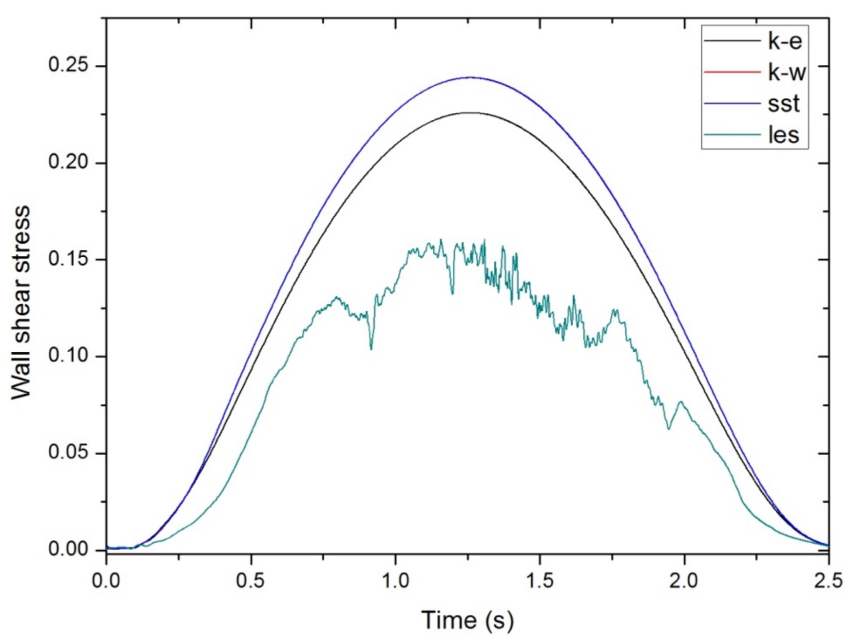

(b)

Fig.3.12. LES and URANS comparisons of wall shear stress in a point located on the anterior side downstream of the minimum cross-sectional area in: (a) subject #1-before surgery; (b) subject #1-after surgery.

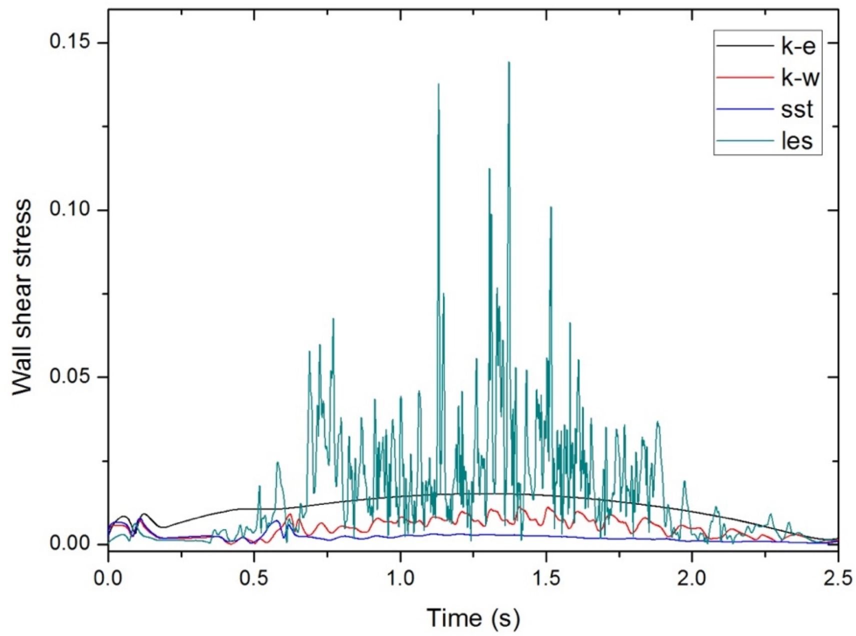

(a)

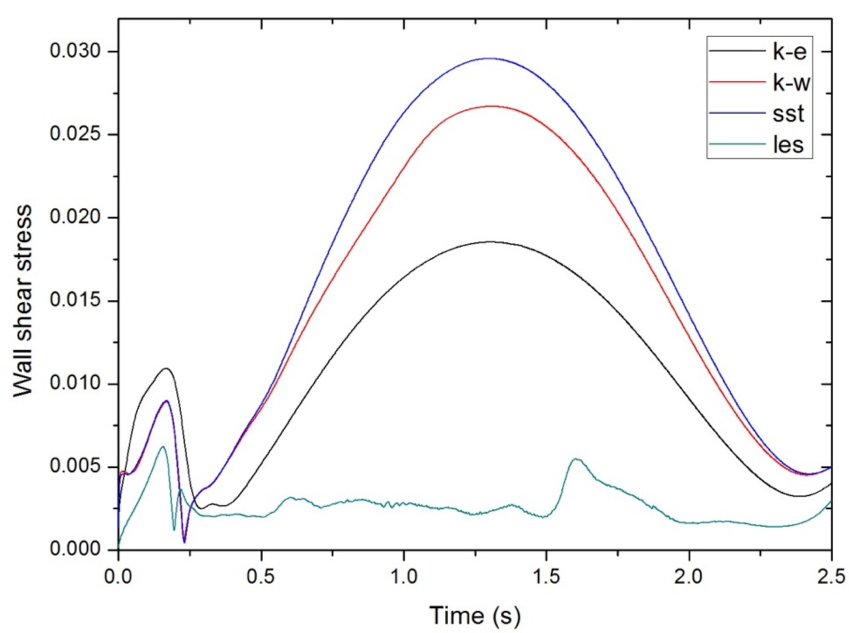

(b)

Fig.3.13. LES and URANS comparisons of wall shear stress in a point located on the anterior side downstream of the minimum cross-sectional area in: (a) subject #2-before surgery; (b) subject #2-after surgery.

The axial velocity distribution during inspiration along a sagittal-plane (Fig. 3.4 and Fig. 3.6) indicated that all turbulence models are able to capture a jet-like axial velocity, which increased from the minimum cross-sectional area due to the anatomically narrowed airway near the soft-palate before surgery. The discrepancies were mainly found in the axial velocity distributions downstream of the minimum cross-sectional area: before surgery, LES was able to capture more than two vortexes (Fig. 3.5d and Fig. 3.7d), which are considered an important factor in airway occlusion in the anterior side (Liu, et al., 2012). However, only two vortexes could be found for the k-ω results (Fig. 3.5b-c) and just one for the k-ε results (Fig. 3.5a) in subject #1. For subject #2, all three URANS models were able to get two large vortexes near the downstream of the minimum cross-section area and epiglottis (Fig. 3.7a-c), while the results using LES illustrated more small random vortexes and a longer axial velocity increasing region along the posterior side of the sagittal plane (Fig. 3.5d and Fig. 3.7d). After surgery, due to changes in airway morphology, the differences emerged in the anterior side: all four models were able to capture a large vortex downstream of the minimum cross-sectional area as illustrated in Figure 3.5e-h and Figure 3.7e-g, but an additional vortex was found near the epiglottis (Fig. 3.7h).

Fig. 3.8 and 3.9 show the axial velocity contour at two cross-sectional planes in the whole airway. The maximum axial velocity can be observed by all four turbulence models at the minimum cross-sectional area (near the retro-palatal pharynx), and the patterns in this plane seem similar for all four models. For the downstream plane, it is found that the patterns obtained by the URANS models, especially for the subject before surgery, are quite different in the location of the flow separation region from that by LES (Fig. 3.8a-d and Fig. 3.9a-d). However, for the results after surgery, though the k-ε results still differ in flow separation region from those by LES, the patterns shaped by the k-ω appear to be close to the results of LES simulation (Fig. 3.8e-h and Fig. 3.9e-h).

Changes in cross-sectional area and mean static pressure distribution from nasopharynx to epiglottis for both subjects are shown in Fig. 3.10 and 3.11. For subject #1 (Fig. 3.10), surgery led to significant change in upper airway morphology: the minimum cross-sectional area in the retro-palatal (collapse region for OSA) was widened from 50 mm^2 to 250 mm^2, but the reconstructed narrowest cross-sectional area moved upward and became 100 mm^2 after reconstruction of airway. The minimum cross-sectional area in the retro-palatal was enlarged by a factor of two (50 mm^2 to 100 mm^2). Pressure drop from the nasopharynx to the minimum cross-sectional area was reduced significantly from about 40 Pa to about 5 Pa for all four turbulence models. This indicates that all the turbulence models are able to capture the pressure drop, this considered an important factor in evaluation of upper airway collapse. For subject #2, before treatment, the pressure drop in the area from the nasopharynx to the minimum cross-sectional area was quite large (about 60 Pa) due to the large negative pressure induced by high speed jet flow. After treatment, the pressure drop reduced significantly, to less than 1 Pa, which may be because the minimum cross-sectional area was surgically widened by a factor of six (from 47 mm^2 to 300 mm^2) (Fig. 3.11). It can be clearly observed that, even though the pressure value differs with turbulence model, the pressure profile along the airway is nearly the same for all four turbulence models, leading to a similar pressure drop across the airway.

It is known that the central respiratory pattern generator requires an external stimulus to activate respiratory events (Taylor, et al., 1999), and that input signals emanate not only from chemoreceptors but also from mechanoreceptors in the upper airway (Miller, 2014). Oscillating pressure may trigger reflex in the respiratory muscles (Henke & Sullivan, 1993). In our previous work, we have found that there exists a flow oscillation in the upper airway which is induced by flow separation downstream of the minimum cross-sectional area, this oscillation being stronger in normal subjects and OSA subjects with successful treatment, but weak in OSA subjects prior to treatment (Liu, et al., 2012). This oscillating signal may be an external stimulus to the mechanoreceptors or a reflection of the upper airway dilator muscles in the upper airway. Fig. 3.12 and Fig. 3.13 compare the time history of wall shear stress at one point located in the anterior side downstream of the minimum cross-sectional area. It is clear that LES is well able to capture flow oscillation, while the URANS model captures comparatively little wall shear stress oscillation (flow oscillation). This may be due to the mean component of the velocity in the URANS models in chapter 2.

3.3 Conclusions

In the past years, many researchers have used CFD to understand airflow features in the upper airway with OSA. However, the complexity of the geometrical models makes accurate prediction, and so too application, a challenge. Since upper airway flow is unsteady and turbulent, proper selection of turbulence model is crucial to obtain with accuracy a sufficient number of flow features in order better to predict surgery outcome and so facilitate surgery planning. In this study, we numerically simulated the turbulent flows in four different OSA upper airway models with three URANS two-equation turbulent models (unsteady k-ε, standard k-ω, and k-ω Shear Stress Transport) and one LES model. The simulation results suggest the following conclusions:

(1) For all four OSA upper airway models, the URANS models and the LES model are able to obtain the same pressure drop across the airway, proving that the URANS models have the same capacity for mean pressure simulation compared with the LES model.

(2) Due to the anatomical narrowing of the OSA upper airway model before surgery, a strong jet flow was induced, resulting in several complex recirculation zones downstream of the minimum cross-sectional area. The LES model is able to capture much more of these recirculation zones, while unsteady standard k-ω and k-ω SST can usually capture two recirculation zones, and the unsteady k-ε model can capture only one.

(3 For OSA upper airway models after surgery, the airway is widened and jet flow is attenuated; consequently, the separation induces a main recirculation flow downstream of the minimum cross-sectional area. All four turbulence models are able to capture this main recirculation zone.

(4) Flow oscillation may play an important role in evaluation of OSA severity. An LES model can well simulate flow oscillation, while only a little flow oscillation can be captured by the URANS models.

(5) The purpose of CFD simulation in an OSA upper airway is to predict surgery outcome and help with surgery planning based on the correct and accurate flow features obtained. An LES model is capable of capturing flow patterns and flow oscillation, and is good for prediction of OSA surgery. Even URANS can attain the correct pressure distribution along an airway, though it may not be appropriate for use in prediction of surgery outcome.

Chapter 4 Comparison between experimental measurement and CFD simulation

Obstructive sleep apnea (OSA) is a common disorder characterized by partial or complete narrowing of the pharyngeal airway during sleep, (Mihaescu et al., 2011), affecting up to 20% of adults and recognized as an independent risk factor for a range of conditions including diabetes, hypertension and stroke. (McCabe and Hardinge, 2011). The pathogenesis of this disorder is not, however, as yet fully understood, and a better understanding of OSA pathophysiology is required in order to guide treatment planning.

Accurate models of the upper airway are crucial for understanding the mechanisms of OSA, but due to the complex geometry of the upper airway, it is expensive and difficult to study experimentally, be it in vivo or in vitro. Recently, due to its non-invasive nature, Computational Fluid Dynamics (CFD) analysis has been utilized to characterize flow features in human upper airway models. Malhotra et al. (2002) created simple 2D male and female upper airway models and suggested that an increased length of vulnerable airway, together with increased soft palate size, results in a male predisposition to pharyngeal collapse. Martonen et al. (2002) generated a

3D upper airway model based on the medical school teaching model, and suggested that airflow patterns were mainly dependent on flow rate values for a prescribed phase of breathing. Nithiarasu et al. (2008) carried out numerical simulation using the Reynolds-Averaged Navier-Stokes (RANS) method based on a CT-scanned upper airway model, and their numerical technique was validated against the measurement in an idealized oropharynx from Heenan et al. (2003). Jeong et al. (2007) studied numerically the flow in a CT-scanned upper airway using a low Reynolds number k–ε model, and found the turbulent jet which formed at the velopharynx due to area restriction to be the most noteworthy feature in the pharyngeal airway of patients with OSA. In real situations, flow in the human upper airway is unsteady, and time-averaged turbulence models (Nithiarasu et al., 2008; Jeong et al., 2007; Cheng et al., 2013) are unable to capture characteristics of anisotropic flow, such as the adverse pressure gradients or turbulent velocity fluctuations generated in these irregular upper airway models. (Wilcox, 1998). Direct numerical simulation (DNS) is the best way to compute flow characteristics in the upper airway, but it is too expensive for upper airway flow at high Reynolds numbers. Hence, Large Eddy Simulation (LES), a compromise model between RANS and DNS, is much more feasible in terms of computational power required than DNS, and can resolve the most energetic flow scales (entering into the inertial sub-range) while modelling only the smallest dissipative scales. More and more CFD computations on upper airways with OSA are using LES, which has become the preferred tool for capturing relevant flow features. (Luo et al., 2004; Mihaescu et al., 2008; Mihaescu et al., 2011; Liu et al., 2012).

To validate the suitability of CFD modeling methods, several experiments were carried out under various conditions. Due to advancements in rapid prototyping technology, the anatomical in vitro airway model of subjects with OSA can be fabricated according to numerical geometry models. Kim et al. (2009) investigated respiratory airflow in the human airway by use of PIV, providing quantitative results for the full airway model under physiological flow conditions. Xu et al. (2006) studied the effect of airway geometry on internal pressure in the upper airways of children with OSA by using a two-equation low-Reynolds number turbulence model with steady flow boundary conditions in inspiration and expiration. To validate their CFD results, the researchers fabricated a physical airway model at 85% scale, measured the pressure at several locations, and found a good agreement between pressure measurements and CFD calculations. Mylavarapu et al. (2009) investigated the expiratory flow in a realistic human upper airway model constructed from MRI scans. They used LES, steady RANS with two-equation turbulence models (k-ε, standard k-ω, and k-ω Shear Stress Transport (SST)) and a Spalart-Allmaras one-equation turbulence model. To validate their CFD results, they fabricated a 2:1 scale mechanical airway model and measured wall pressure and mean velocity at inlet. They found a good agreement between computation and measurement, and suggested that CFD could be used to investigate flow characteristics of the upper airway with accuracy. Zhao et al. (2013) studied both numerically and experimentally the effect of mandibular advancement splints (MAS) treatment on flow in an upper airway model with OSA. They used the k-ω SST turbulence model, and validated the numerical method against the pressure measured on a 1:1 flexible upper airway model fabricated using 3D stereolithography.

All of the in vitro experiments conducted above were focused on pressure measurements by means of pressure taps located along the airway walls, and velocity profile, though important, was typically ignored due to the difficulty and complexity of such measurements. On the basis of our preliminary study (Lu et al., 2014), both the RANS and LES models are able to capture similar pressure distribution along the upper airway, but there is significant discrepancy in velocity profile among different turbulence models. It is therefore necessary to evaluate the accuracy of turbulence models in simulations of velocity profile in OSA upper airways. Since flow features such as flow separation downstream of the minimum cross-sectional area are key factors in the upper airway occlusion of OSA subjects, accurate prediction of velocity distribution is of significant interest if we wish thoroughly to understand the pathogenesis and treatment of OSA. In this study, we carried out experimental measurements using laser Doppler anemometry (LDA), as well as numerical simulation using an LES model in the upper airway model of an OSA subject before and after surgery, and found excellent agreement between the measured and calculated velocity profiles in both upper airway models.

4.1 Method

4.1.1 Construction of upper airway model

A male OSA patient (38 years old, BMI 25.7, 76 kg) who experienced a successful uvulopalatopharyngoplasty (UPPP) surgery was selected. Surgery had enlarged the area of minimum cross section near the soft palate from 47.4 mm² to 226.7 mm², a fourfold increase. The apnea-hypopnea index (AHI) fell from 60.7 before to 23.9 after surgery. The 3-D anatomically accurate upper airway models were reconstructed from CT-scan images obtained six months following surgery using the image processing software Mimics. The CT images feature an axial plane with a resolution of 0.7×0.7 mm², and a slice thickness of 0.625 mm (Fig. 4.1). Airway extraction was performed using a combination of thresholding and region growing segmentation criteria.

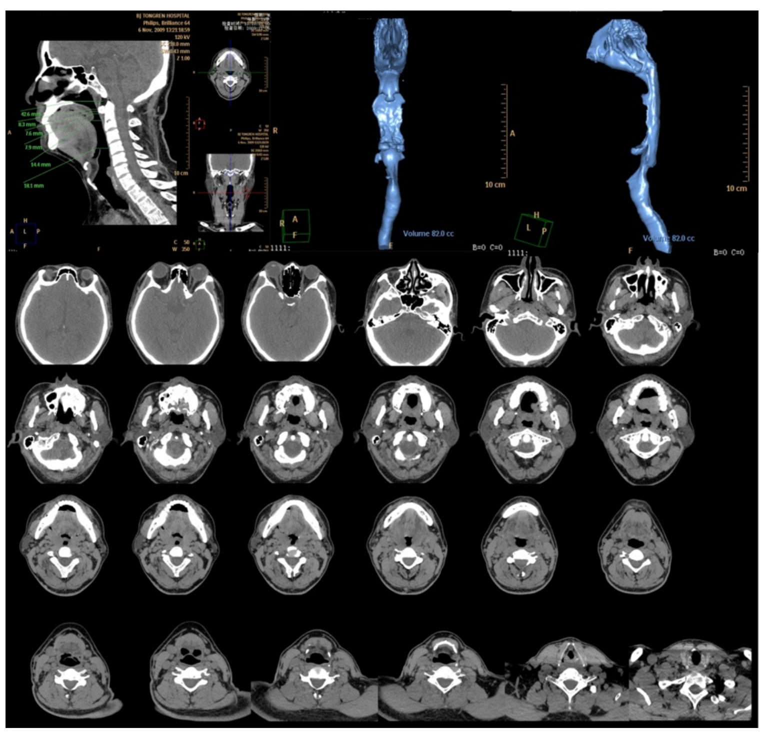

Fig.4.1. Some of the CT scan images after surgery.

4.1.2 Experimental model

Two 1:1 scaled upper airway models were produced by way of a 3-D printing technique (3500 HD Max-3D System, USA) with uniform wall thickness (0.5 mm), as shown in Fig. 4.2. The material used in the models is VisiJet$^{®\ M3}$ Crystal, which is USP Class VI certified for approved medical applications. The inlet and outlet were extended to minimize the velocity boundary effect. The LDA system (Dantec Dynamics, Denmark), with its <1% uncertainty, was utilized to measure the velocity profile inside the model. Since the laser beam diameter is 2.2 mm, the velocity within 3 mm of the wall cannot be captured. The seeding particles were smoke, generated by the Atomizer Aerosol Generator (TSI 3079) using DEHS oil and inhaled through two soft tubes into the inlet (nostril) of the airway models. The air pump as the air supply was connected with the airway outlet from the tracheal side. Flow rate was controlled by a valve, and measured by a flow meter (DryCal DC-2) ranging from 0 to 30 L/min, with an allowable deviation of 1% (Fig. 4.3). Experiments were conducted at a flow rate of 16.8L/min according to bodyweight (5-10 ml/kg) (Gregory and Andropoulos, 2012).

A transparent window was made in the orophyarnx wall to measure velocity profiles before surgery (15×15 mm) and after surgery (20×20 mm) (Fig. 4.2) at the region where the reversed flow most likely existed. After cutting, the window was covered with a very thin transparent film (thickness< 0.01mm) so that there would be minimal effect on flow. For the model before surgery, five cross sections with 1 mm spacing were chosen, and at each cross-section only one measuring line could be selected due to the narrowed airway (BC1-BC5), as shown in Fig. 4.2a. For the model after surgery, we similarly chose five cross-sections with 1 mm spacing (Fig. 4.2b). Since the morphology changed, and the transparent window could be enlarged, at each cross-section three measuring lines were chosen with spacing of 1.5 mm. The measurement was made from the posterior side to the anterior side of the airway with horizontal movement, with a sampling time of 60s for each point.

4.1.3 Numerical method

The flow field was resolved by CFD solver Fluent (ANSYS 14.5) and the mesh convergence has been discussed in chapter 3. The time-integration was performed using second-order implicit discretization and the coupling between the pressure and the velocity field was implemented through the SIMPLE algorithm. The inlet velocity is 0.8 m/s which is calculated based on the flow rate and the nostril cross-sectional area. The pressure boundary condition in the outlet is set as zero. No-slip boundary condition is applied at the wall of airway and the time step is 0.001 s. The LES turbulent model is employed with WALE sub-grid scale (SGS).

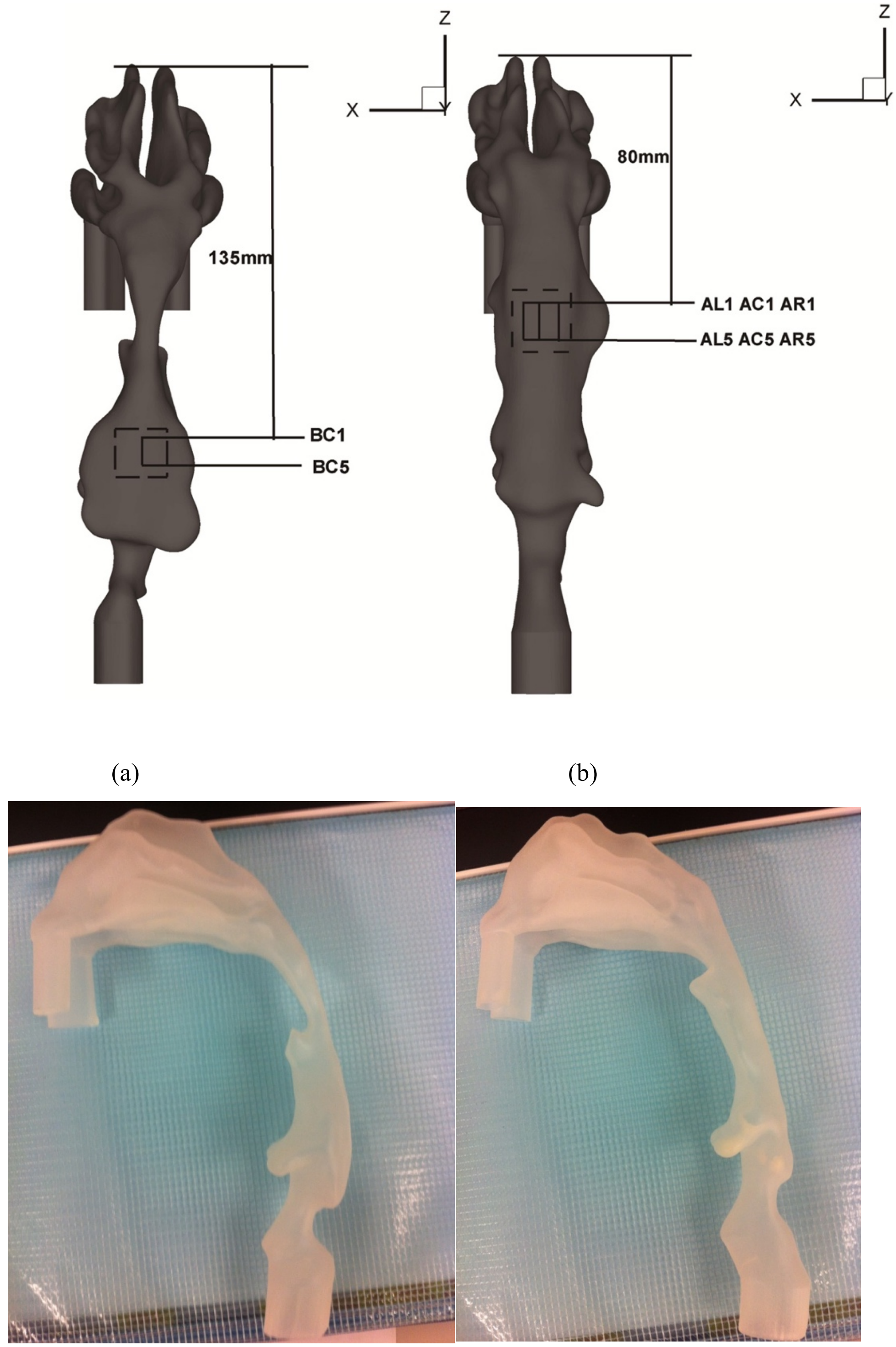

(c) (d)

Fig.4.2. Upper airway models. (a) before surgery, where B indicating before surgery and C center, the dash line is the transparent window- 15×15 mm. (b) after surgery, where A indicating after surgery, L left, and R right, the dash line is the transparent window-20×20 mm. (c) experimental model before surgery. (d) experimental model after surgery.

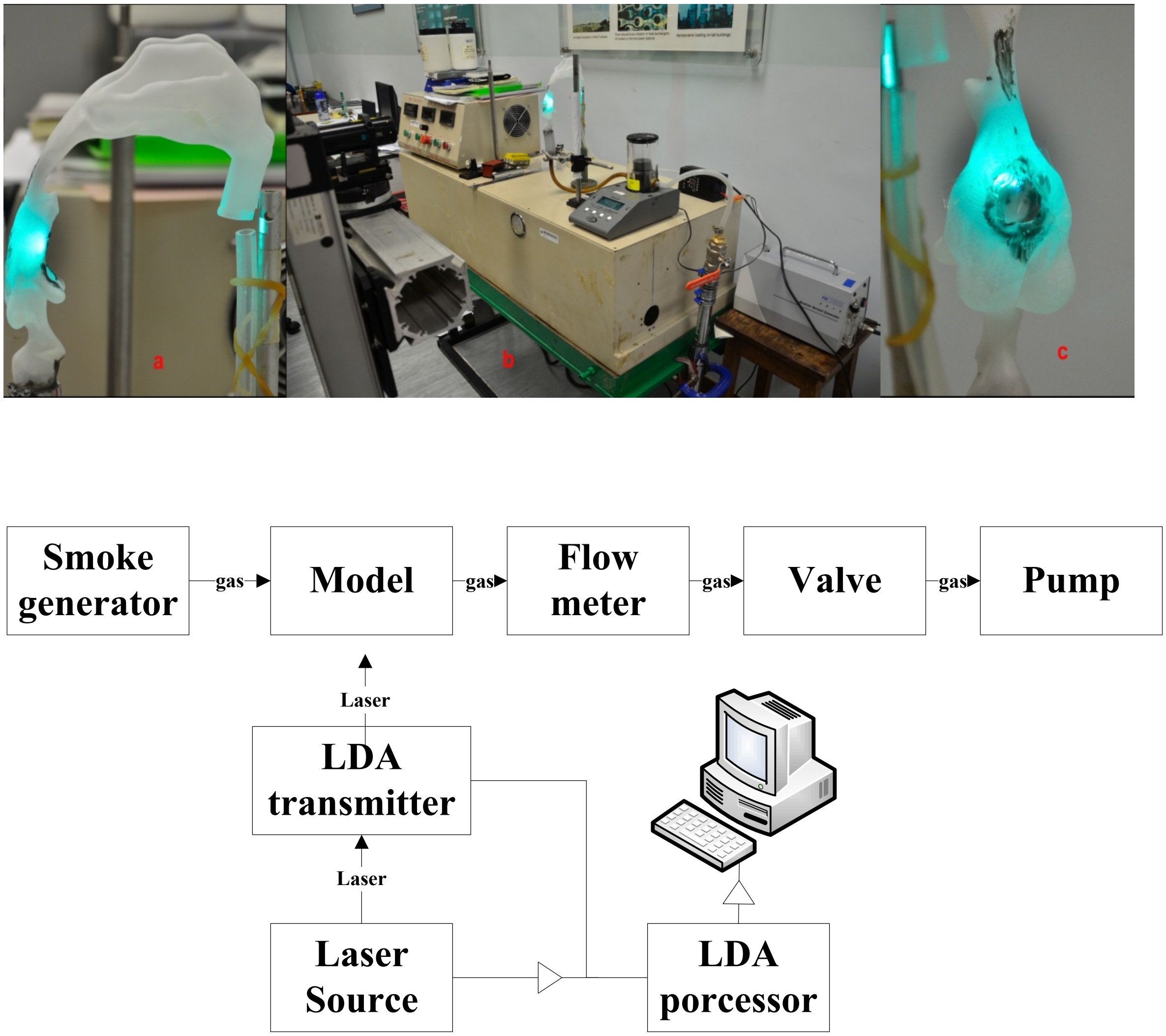

d

Fig.4.3. The experimental setup for LDA velocity measurement: (a) zoom of the inlet; (b) experiment setup for the whole system (c) zoom of the transparent window; (d) the schema of the experiment.

4.2 Results

4.2.1 Simulation results

Fig. 4.4 shows the calculated pressure distribution along the walls of the pre- and post-surgery models. For the model before surgery, a large negative pressure (-7.1 Pa), which is considered the main feature for airway collapse, existed near the retro-palate; for the model after surgery, this negative pressure disappeared and the pressure across the minimum cross-section area decreased significantly from 30 to 4.5 Pa, indicating a significant reduction in flow resistance.

The axial velocity (z direction) contours at different cross sections along the upper airway are shown in Fig. 4.5. For the model before surgery, axial velocity at the minimum cross section was very large due to narrowing of the airway, resulting in a "pharyngeal jet" flow that skewed towards the posterior wall downstream of the minimum cross section. For the model after surgery, due to widening of the upper airway, pressure increased, flow velocity became low and uniform (Bernoulli equation), and a weak "pharyngeal jet" formed downstream of the minimum cross section.

The axial velocity pattern can more clearly be seen from the sagittal plane along the upper airway, as shown in Fig.4.6. For the model before surgery, the flow path line shows that there exist several small recirculations near the oropharynx downstream of the minimum cross section, the patterns being irregular; for the model after surgery, a strong dominant recirculation stands, and flow pattern is regular.

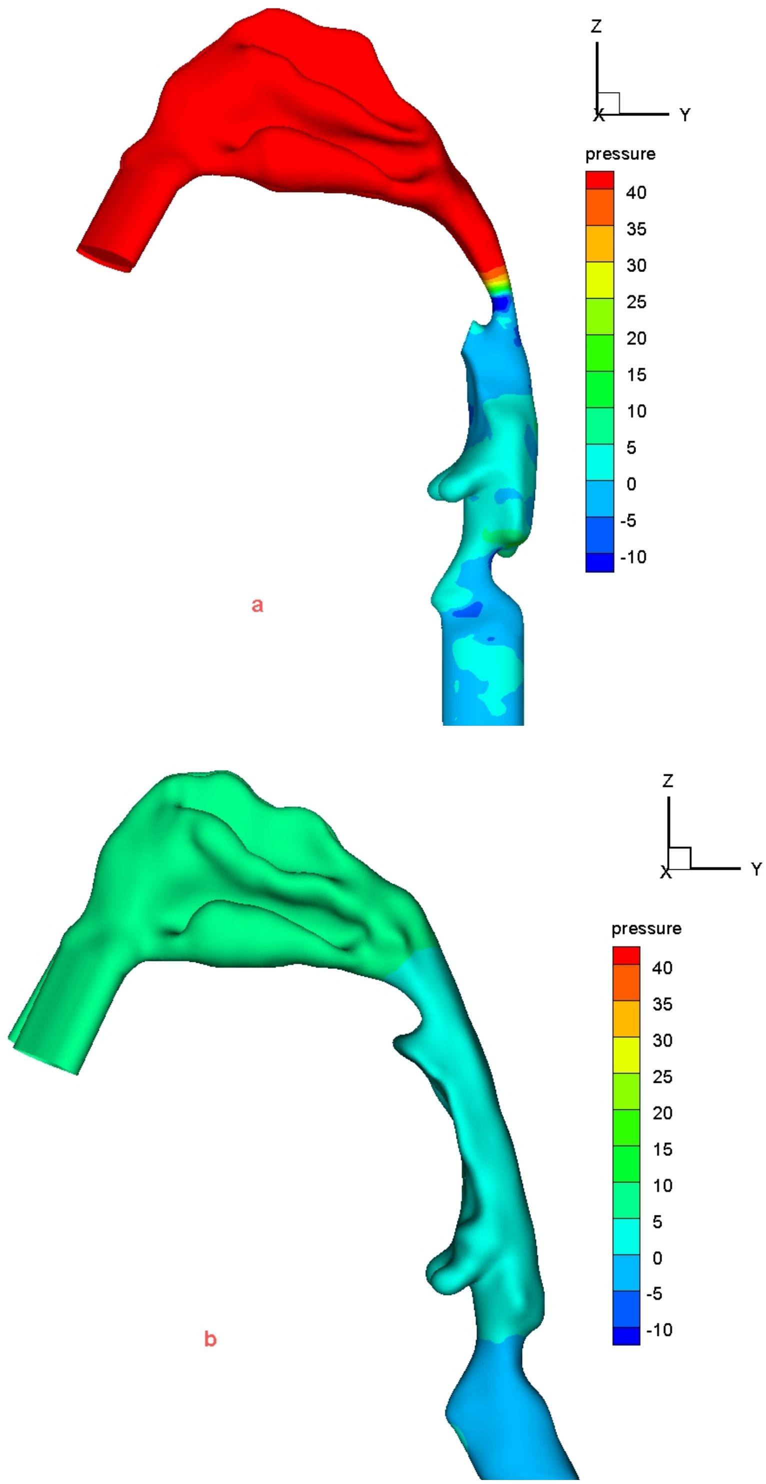

Fig.4.4. The wall pressure distribution for both models: (a) before surgery and (b) after surgery.

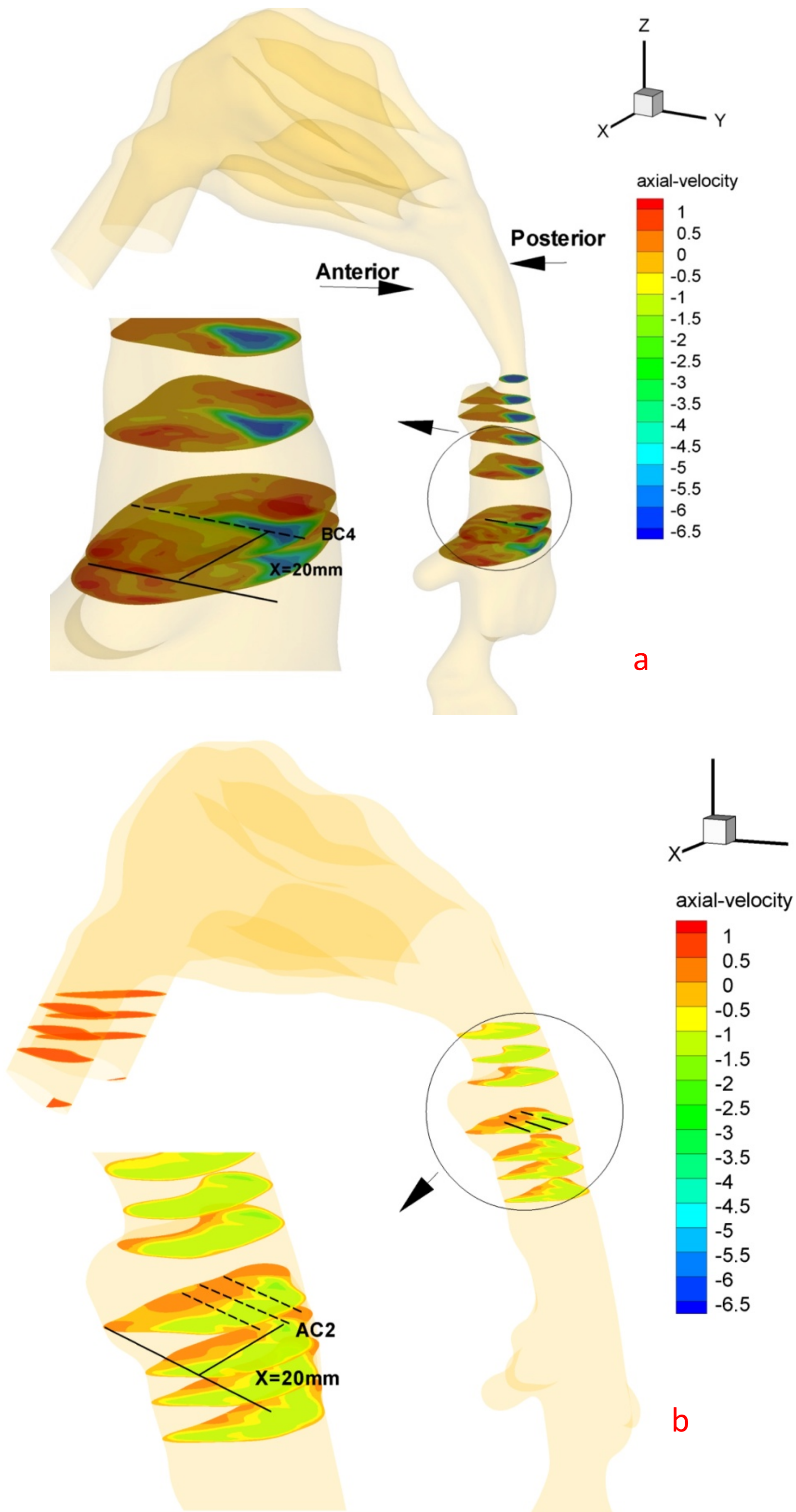

Fig.4.5. The axial velocity contours for both models: (a) before surgery and (b) after surgery. The dash line is the location of LDA measurement.

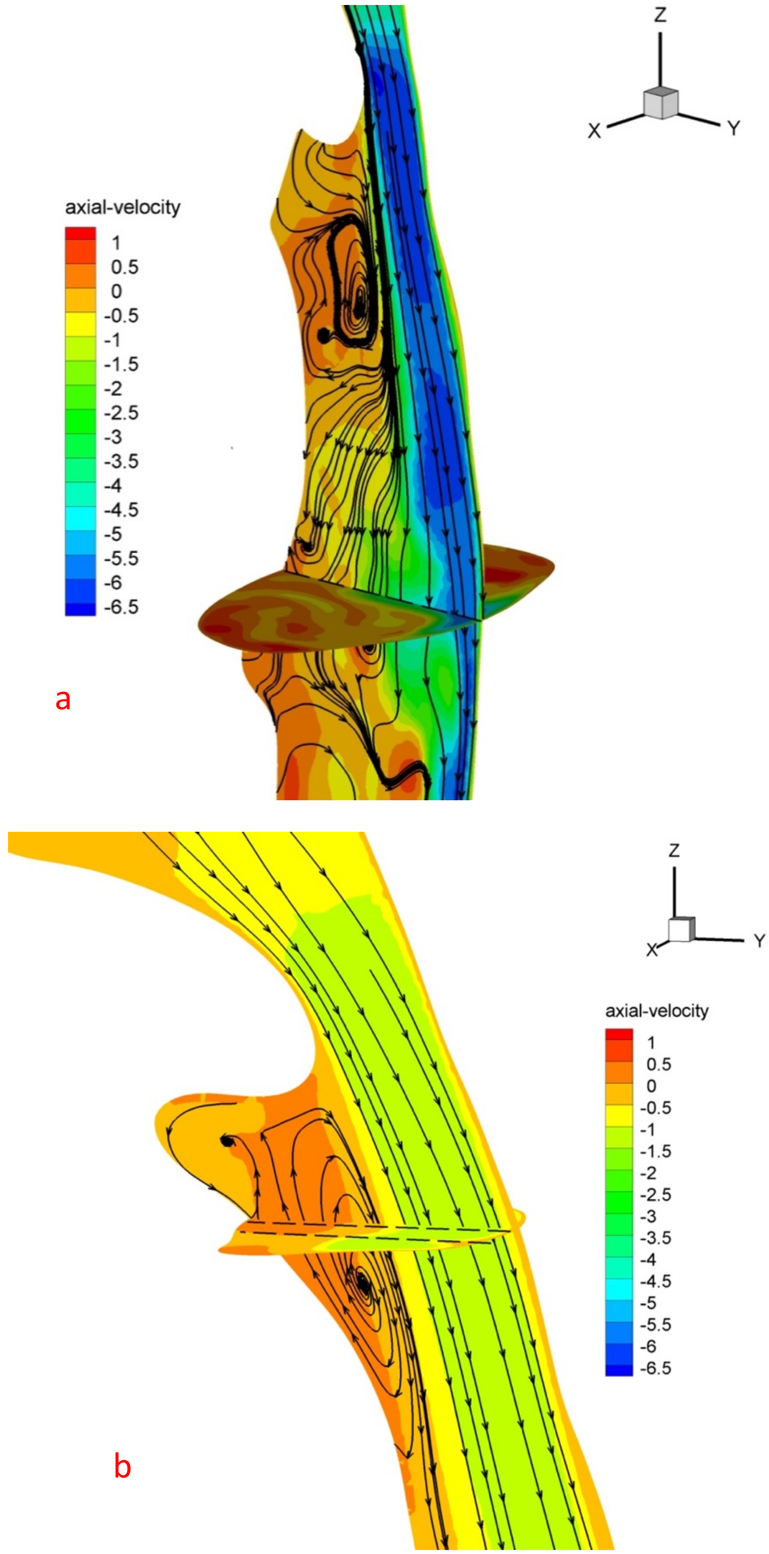

Fig.4.6. The axial flow pattern in the sagittal plane and cross section for both models: (a) before surgery and (b) after surgery. The cross-line between sagittal plane and cross section is the location of LDA measurement.

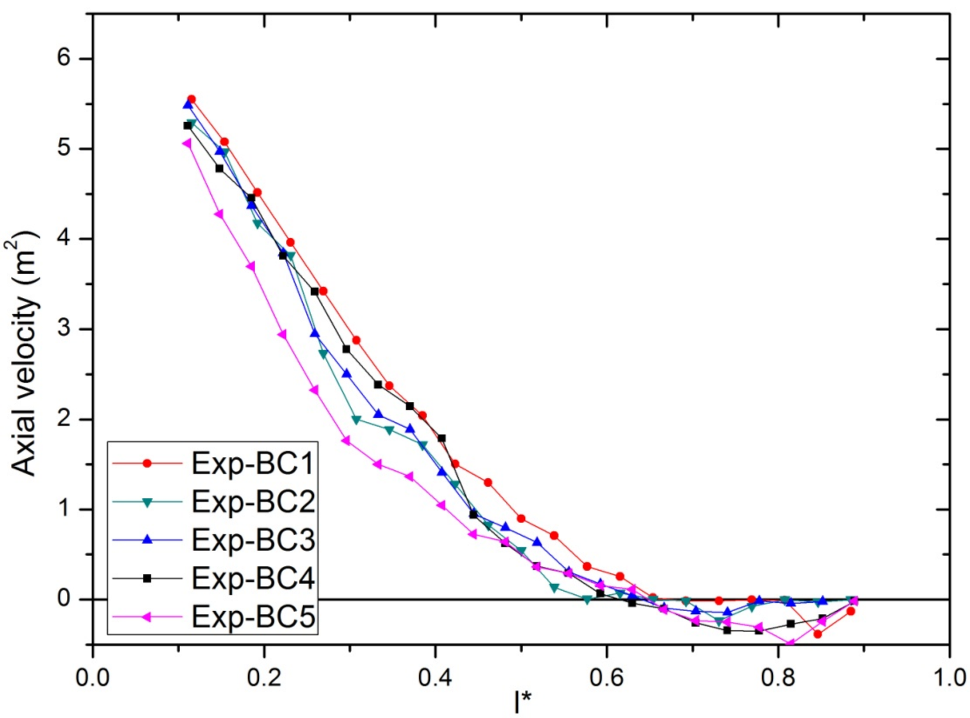

Axial velocity (m2)
l*
Exp-BC1
Exp-BC2
Exp-BC3
Exp-BC4
Exp-BC5
0.0
0.2
0.4
0.6
0.8
1.0
0
1
2
3
4
5
6

(a)

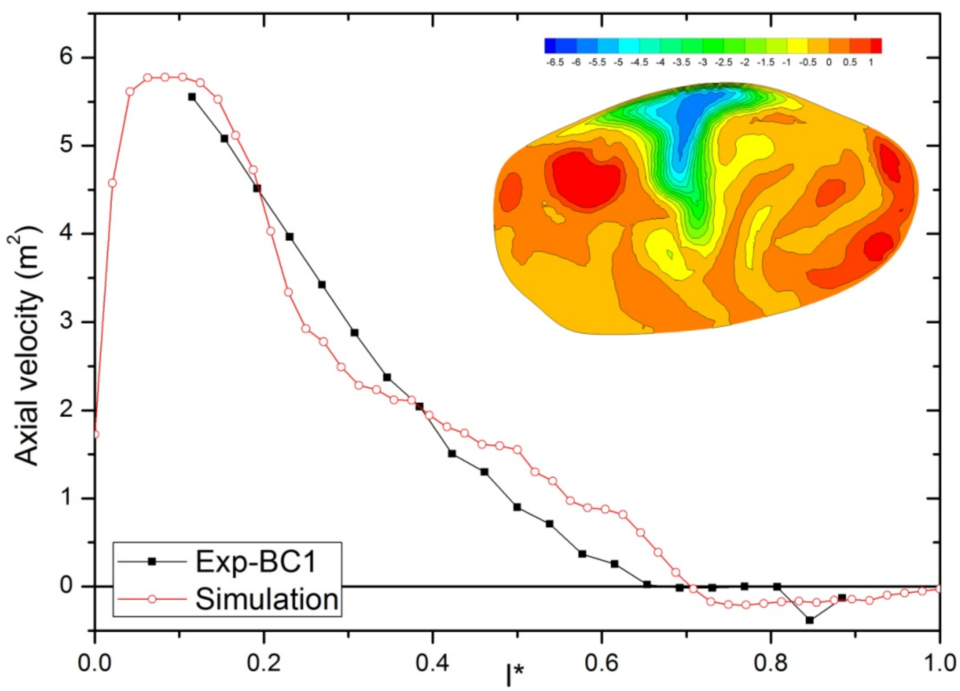

Axial velocity (m2)
l*
Exp-BC1
Simulation
-6.5 -6 -5.5 -5 -4.5 -4 -3.5 -3 -2.5 -2 -1.5 -1 -0.5 0 0.5 1
0.0
0.2
0.4
0.6
0.8
1.0
0
1
2
3
4
5
6

(b)

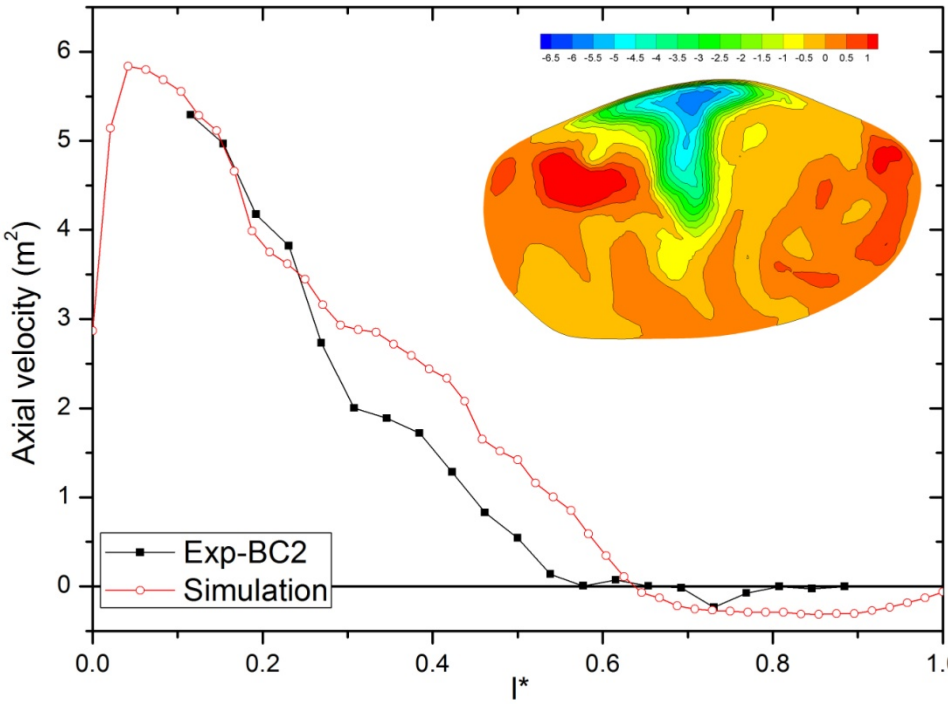

-6.5 -6 -5.5 -5 -4.5 -4 -3.5 -3 -2.5 -2 -1.5 -1 -0.5 0 0.5 1
Axial velocity (m^2)
Exp-BC2
Simulation
l*

(c)

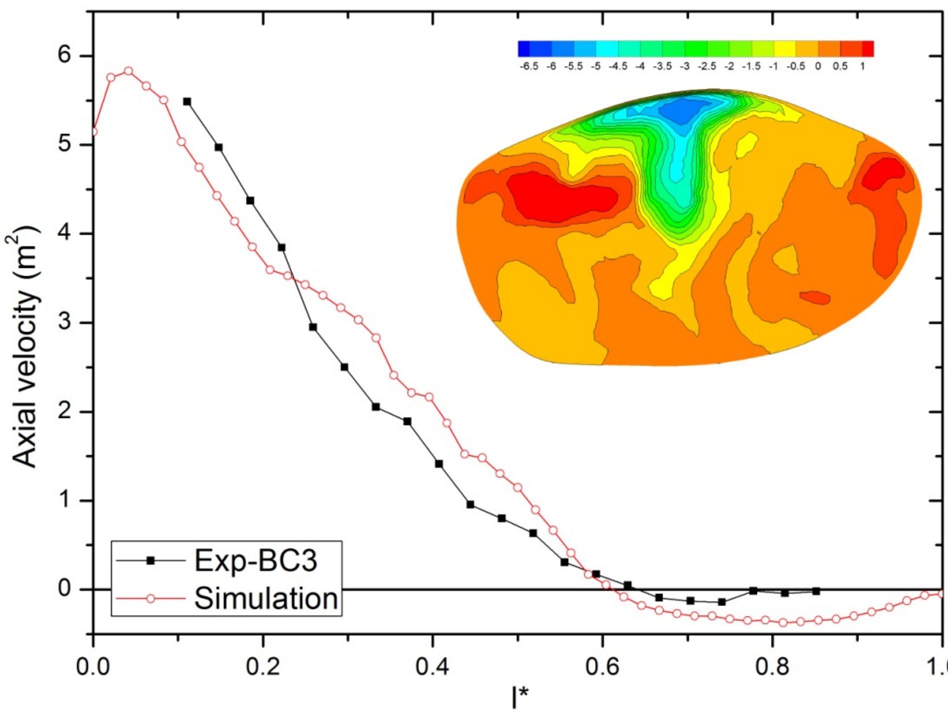

-6.5 -6 -5.5 -5 -4.5 -4 -3.5 -3 -2.5 -2 -1.5 -1 -0.5 0 0.5 1
Axial velocity (m^2)
Exp-BC3
Simulation
l*

(d)

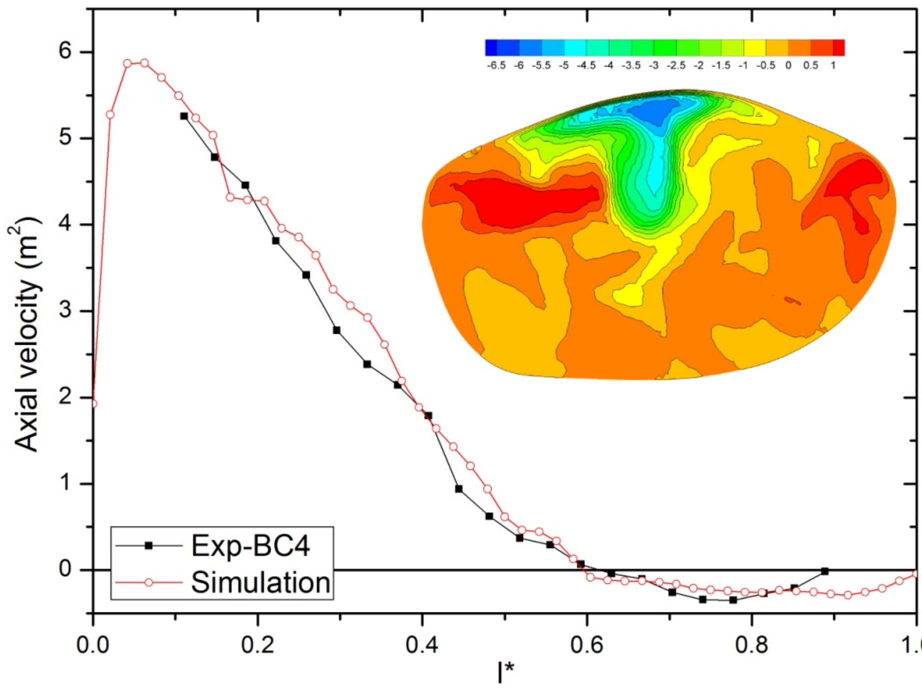

(e)

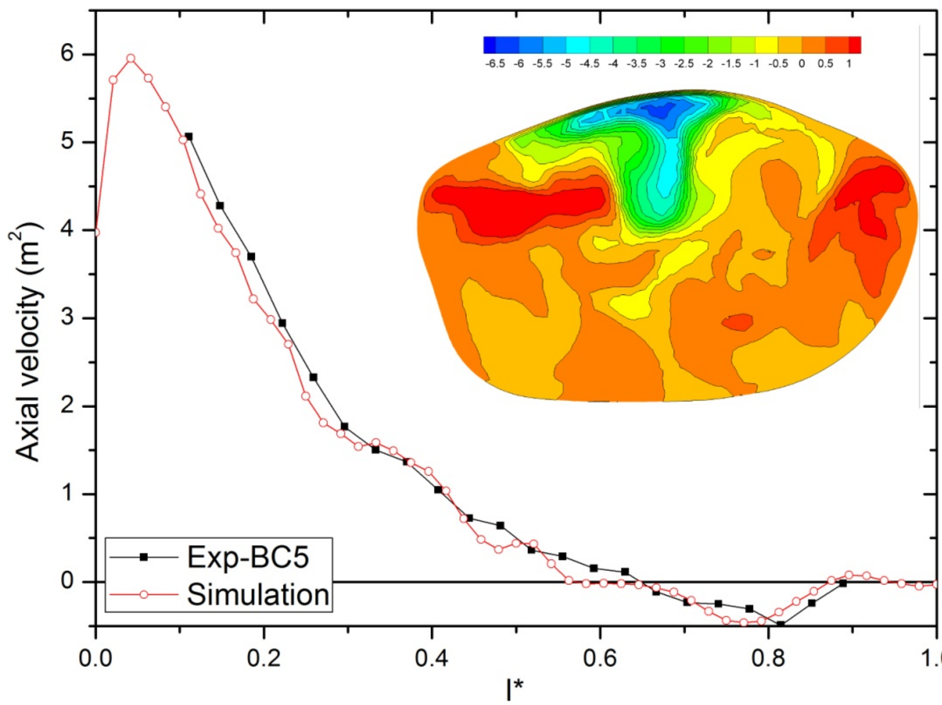

(f)

Fig.4.7. (a) The measured axial velocity profiles in five cross-sections for model before surgery; (b-f) The comparison between measured and calculated velocity profile (BC1-BC5); l is the length of the measured and simulated line, * denotes normalization of the length for experimental and computational lines into the same interval (0~1).

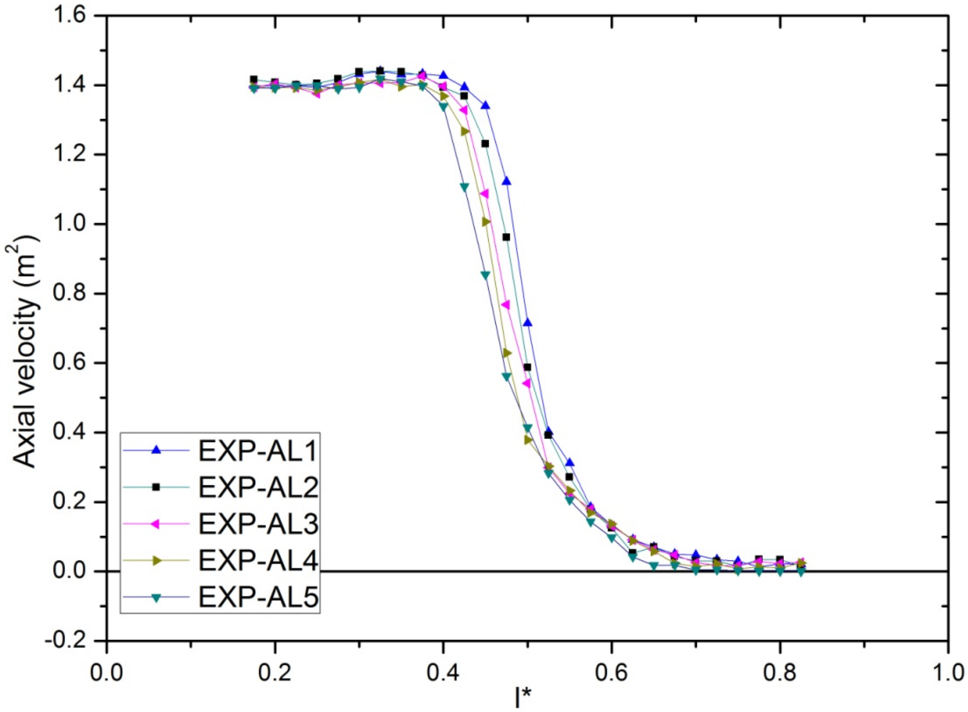

Axial velocity (m^2)
l*
EXP-AL1
EXP-AL2
EXP-AL3
EXP-AL4
EXP-AL5

(a)

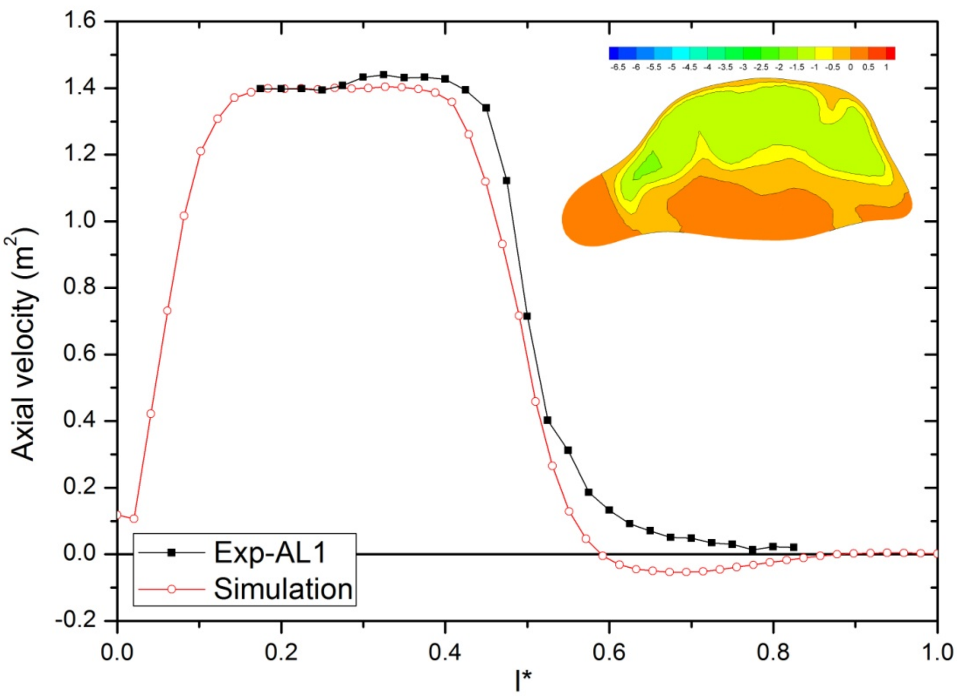

Axial velocity (m^2)
l*
Exp-AL1
Simulation

(b)

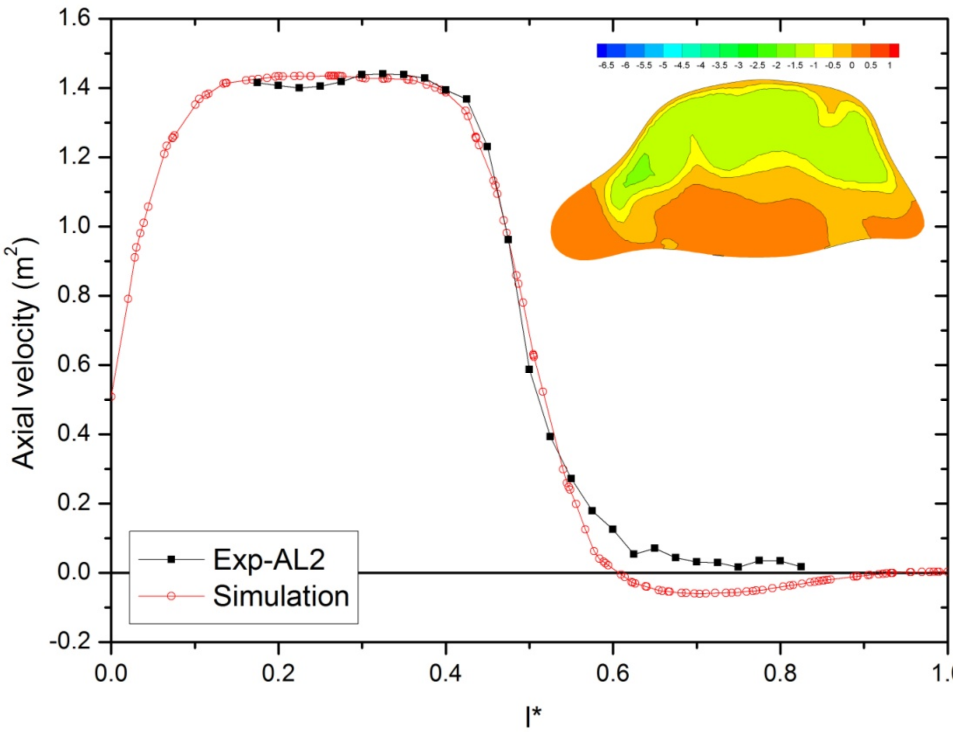
Axial velocity (m2)
l*
Exp-AL2
Simulation
-6.5 -6 -5.5 -5 -4.5 -4 -3.5 -3 -2.5 -2 -1.5 -1 -0.5 0 0.5 1

(c)

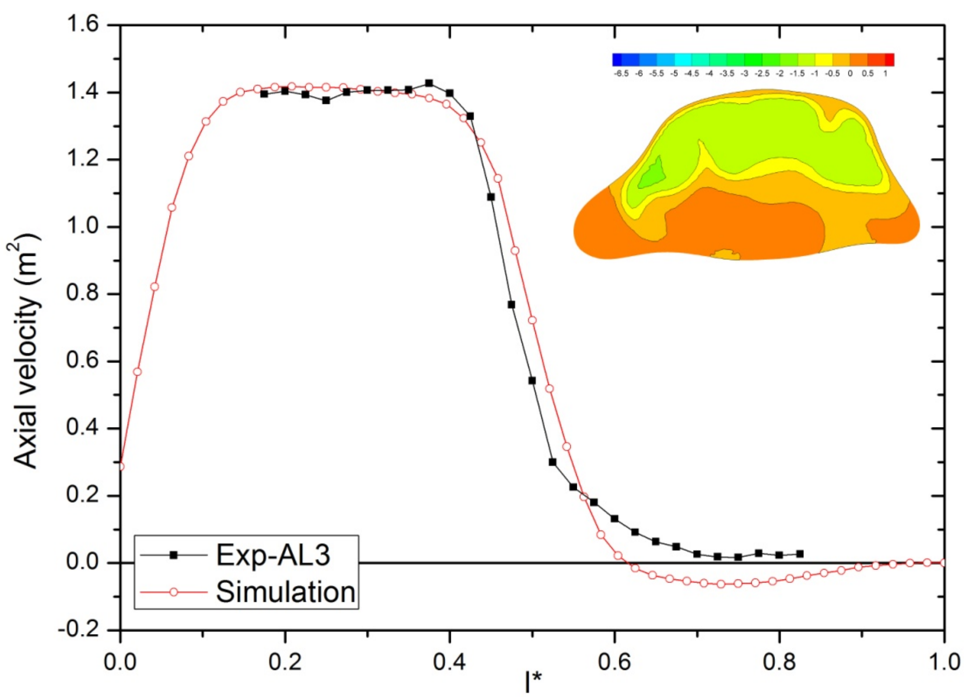
Axial velocity (m2)
l*
Exp-AL3
Simulation
-6.5 -6 -5.5 -5 -4.5 -4 -3.5 -3 -2.5 -2 -1.5 -1 -0.5 0 0.5 1

(d)

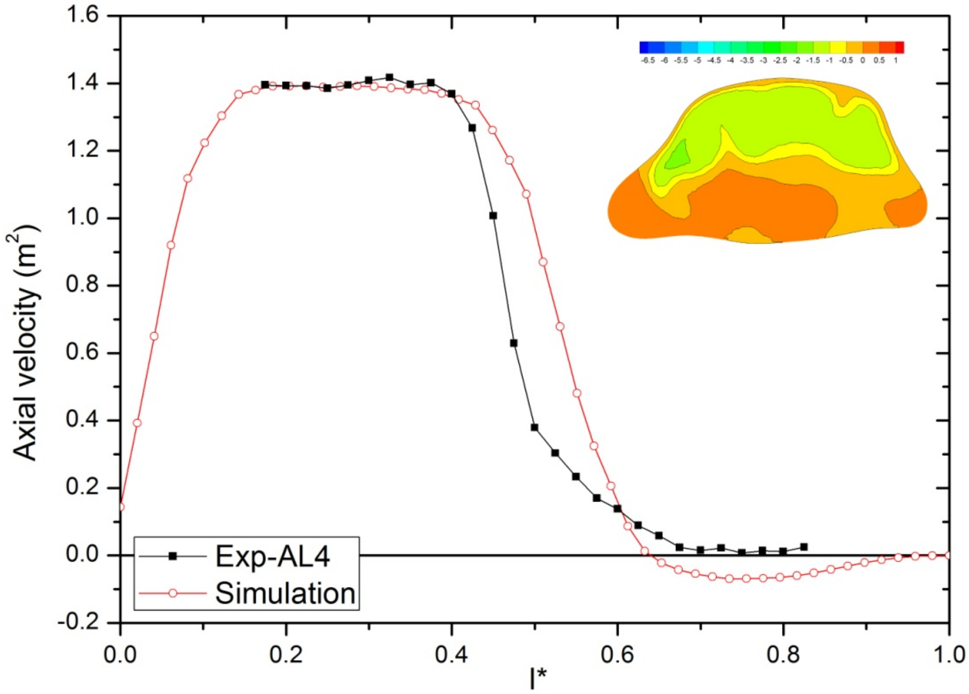

(e)

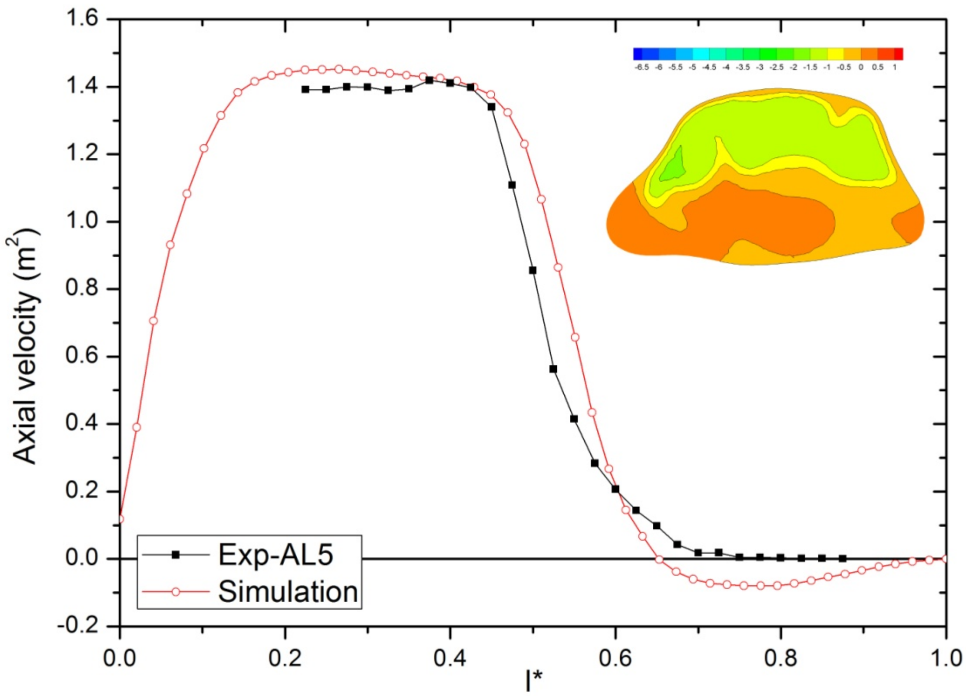

(f)

Fig.4.8. (a) Measured axial velocity profiles at left measuring line in five cross-sections; (b-f) comparison between measurement and calculation at five left measuring line (AL1-AL5).

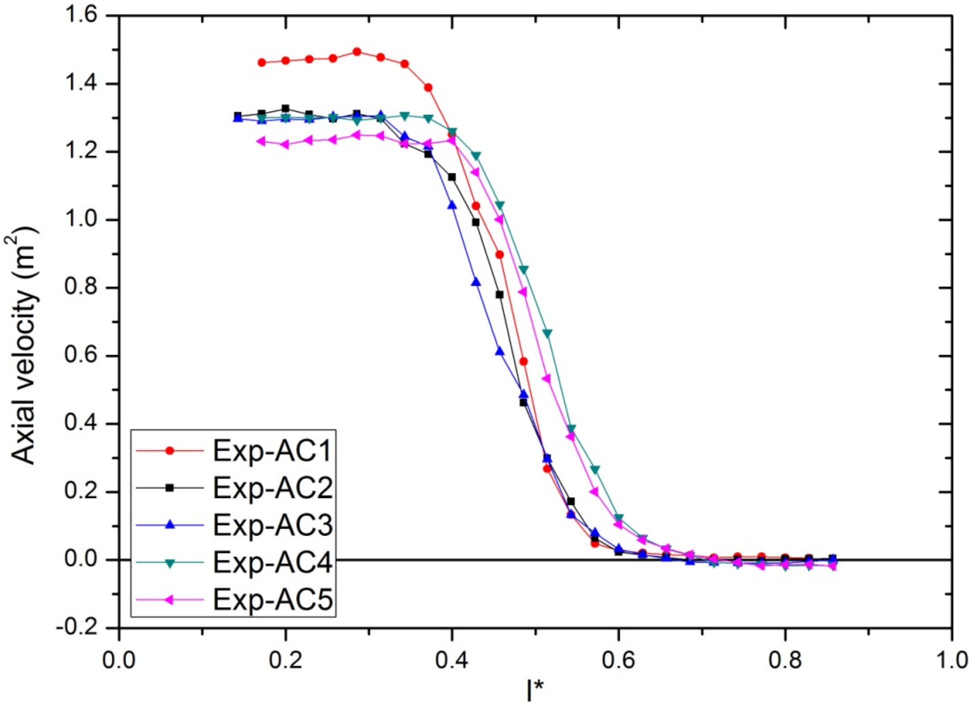
Axial velocity (m^2)
l*
Exp-AC1
Exp-AC2
Exp-AC3
Exp-AC4
Exp-AC5
-0.2
0.0
0.2
0.4
0.6
0.8
1.0
1.2
1.4
1.6
0.0
0.2
0.4
0.6
0.8
1.0

(a)

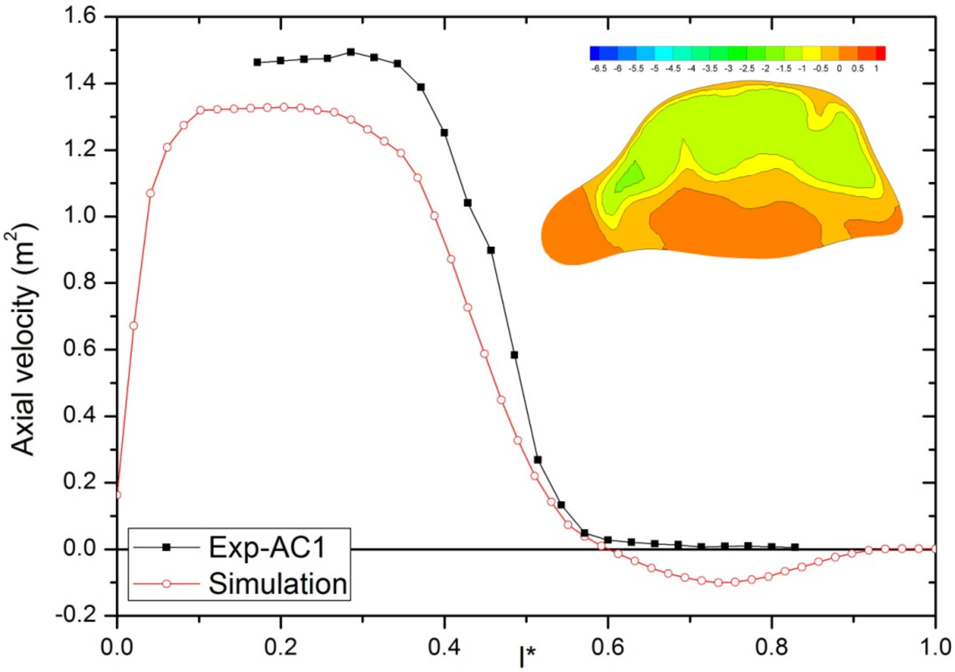
Axial velocity (m^2)
l*
Exp-AC1
Simulation
-6.5 -6 -5.5 -5 -4.5 -4 -3.5 -3 -2.5 -2 -1.5 -1 -0.5 0 0.5 1
-0.2
0.0
0.2
0.4
0.6
0.8
1.0
1.2
1.4
1.6
0.0
0.2
0.4
0.6
0.8
1.0

(b)

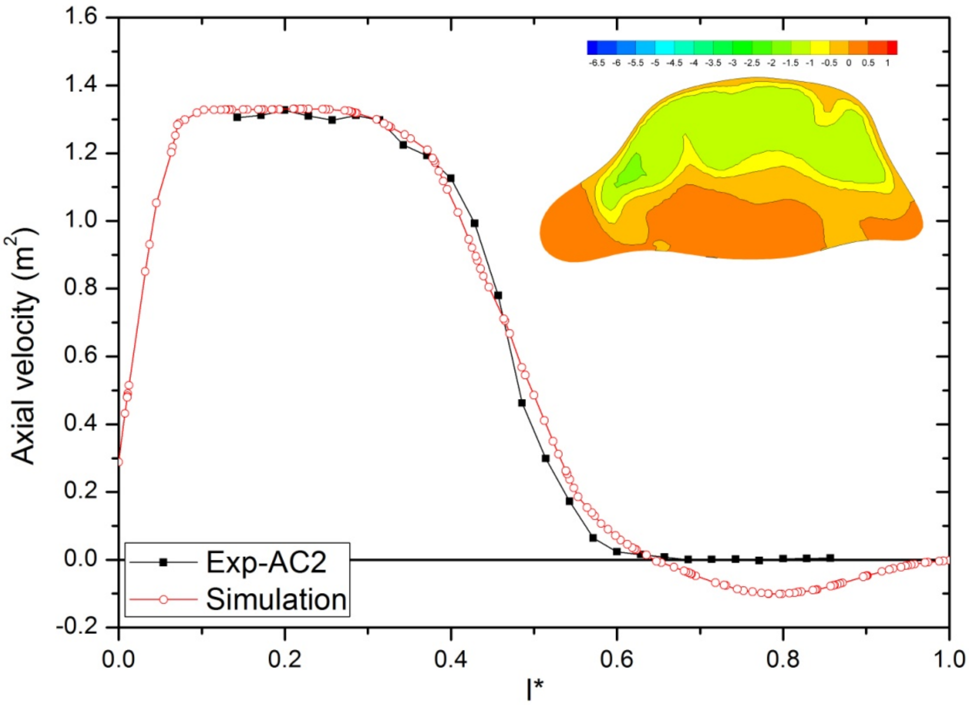

Axial velocity (m2)
l*
Exp-AC2
Simulation

(c)

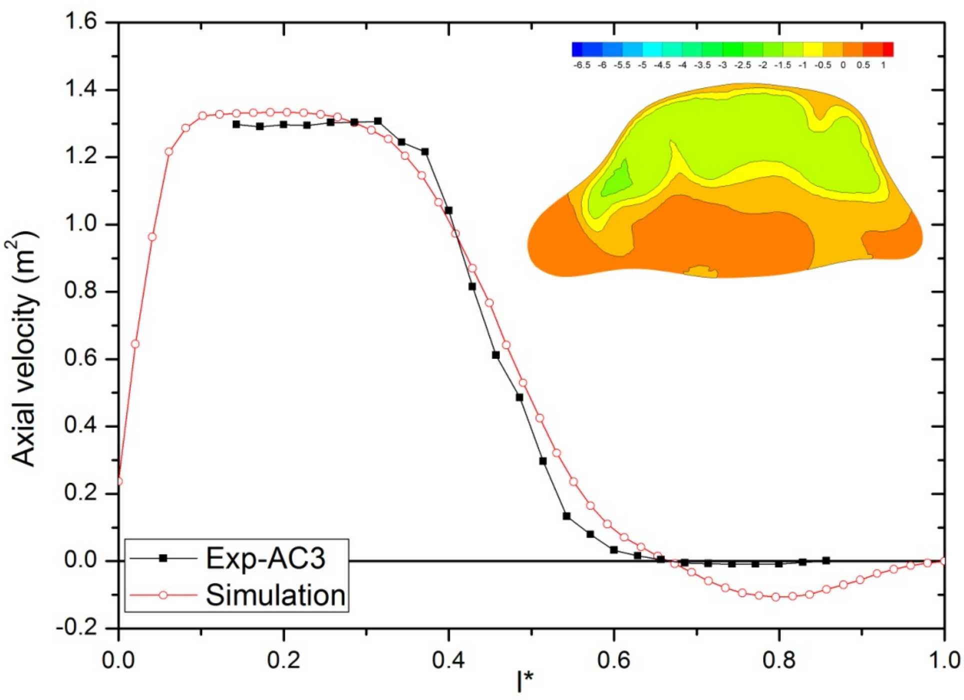

Axial velocity (m2)
l*
Exp-AC3
Simulation

(d)

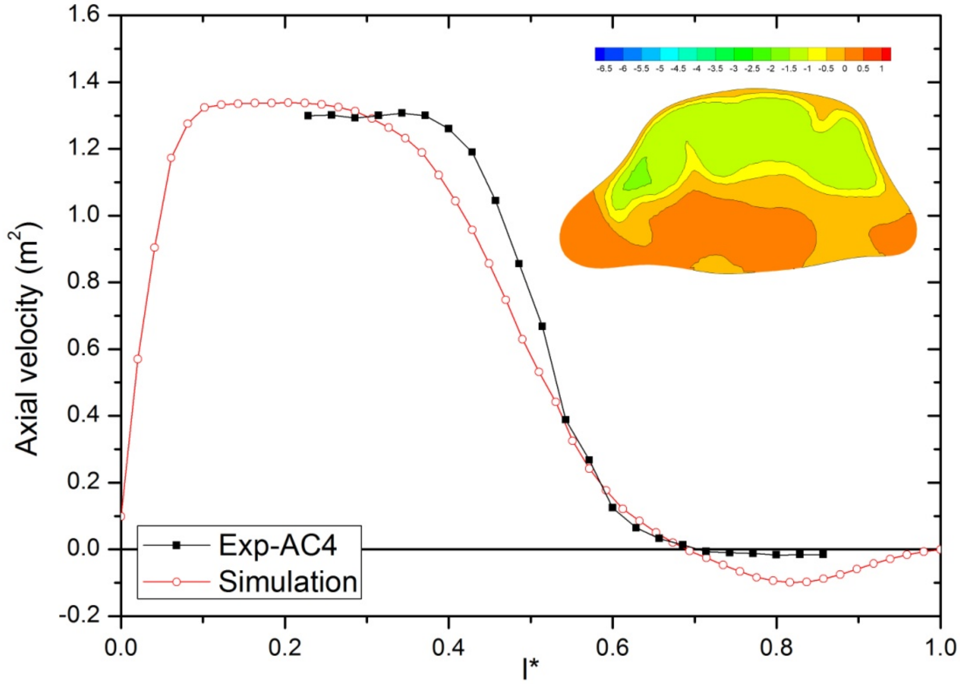

(e)

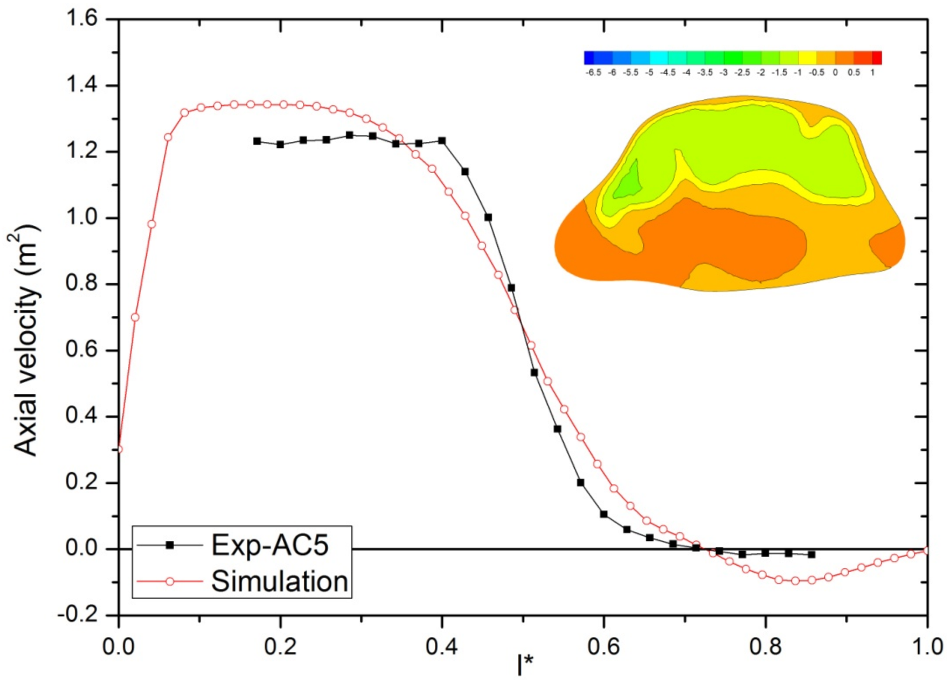

(f)

Fig.4.9. (a) Measured axial velocity profiles at central measuring line in five cross-sections; (b-f) comparison between measurement and calculation at five left measuring line (AC1-AC5).

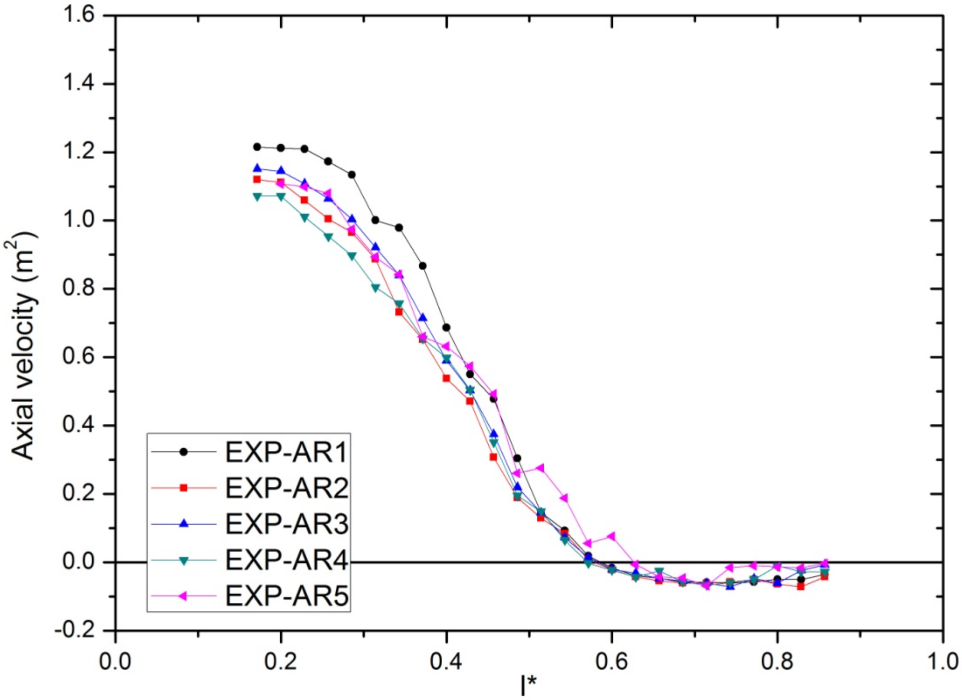

1.6
1.4
1.2
1.0
0.8
0.6
0.4
0.2
0.0
-0.2
0.0
0.2
0.4
0.6
0.8
1.0
Axial velocity (m2)
l*
EXP-AR1
EXP-AR2
EXP-AR3
EXP-AR4
EXP-AR5

(a)

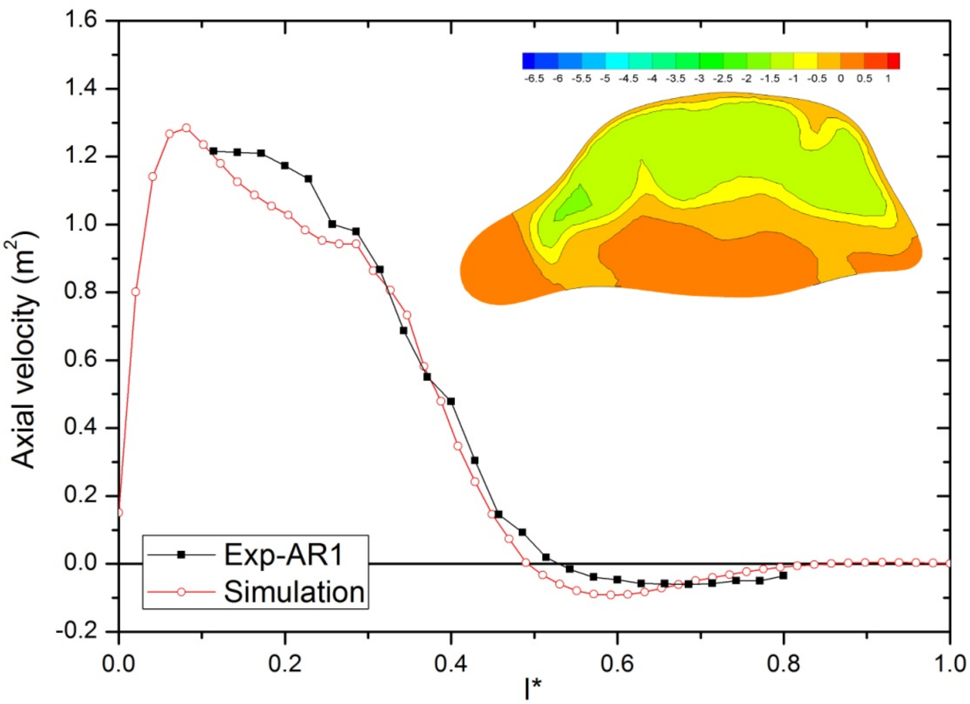

-6.5 -6 -5.5 -5 -4.5 -4 -3.5 -3 -2.5 -2 -1.5 -1 -0.5 0 0.5 1
1.6
1.4
1.2
1.0
0.8
0.6
0.4
0.2
0.0
-0.2
0.0
0.2
0.4
0.6
0.8
1.0
Axial velocity (m2)
l*
Exp-AR1
Simulation

(b)

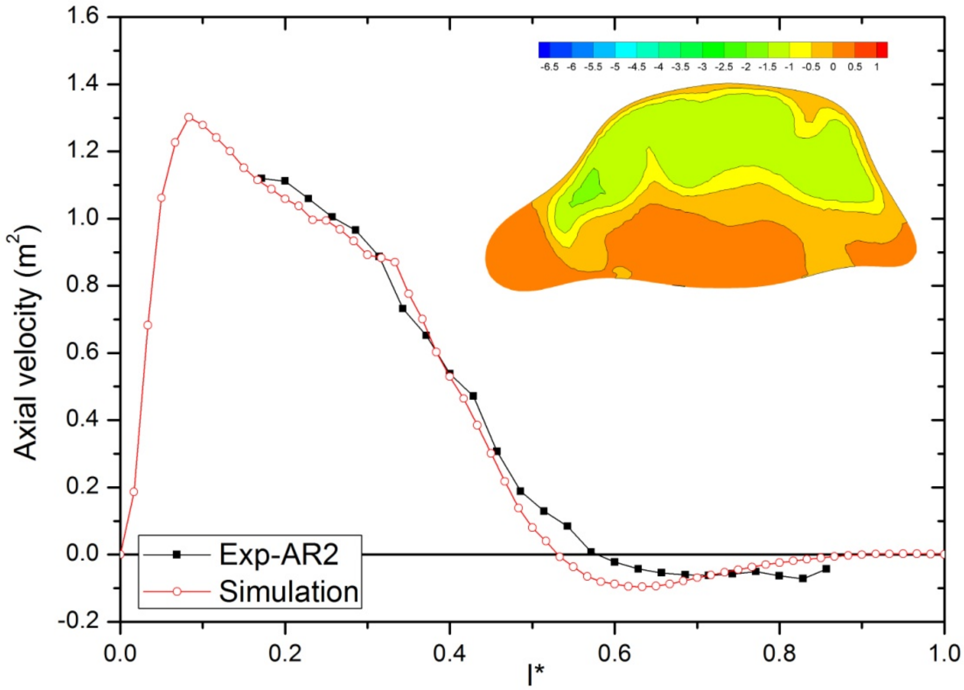

Axial velocity (m^2)
l*
Exp-AR2
Simulation
-6.5 -6 -5.5 -5 -4.5 -4 -3.5 -3 -2.5 -2 -1.5 -1 -0.5 0 0.5 1

(c)

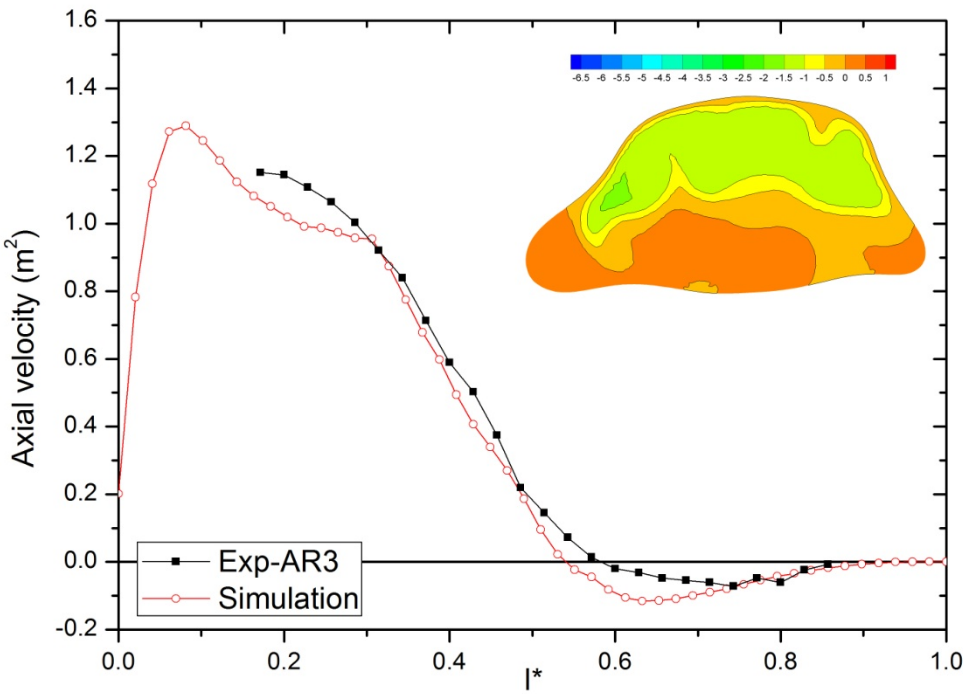

Axial velocity (m^2)
l*
Exp-AR3
Simulation
-6.5 -6 -5.5 -5 -4.5 -4 -3.5 -3 -2.5 -2 -1.5 -1 -0.5 0 0.5 1

(d)

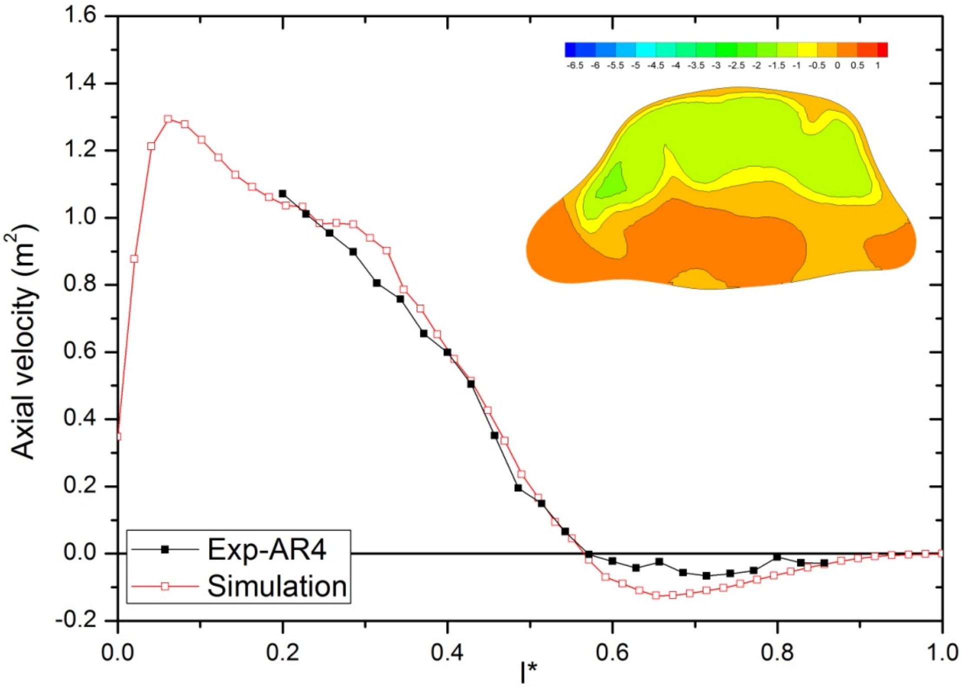

(e)

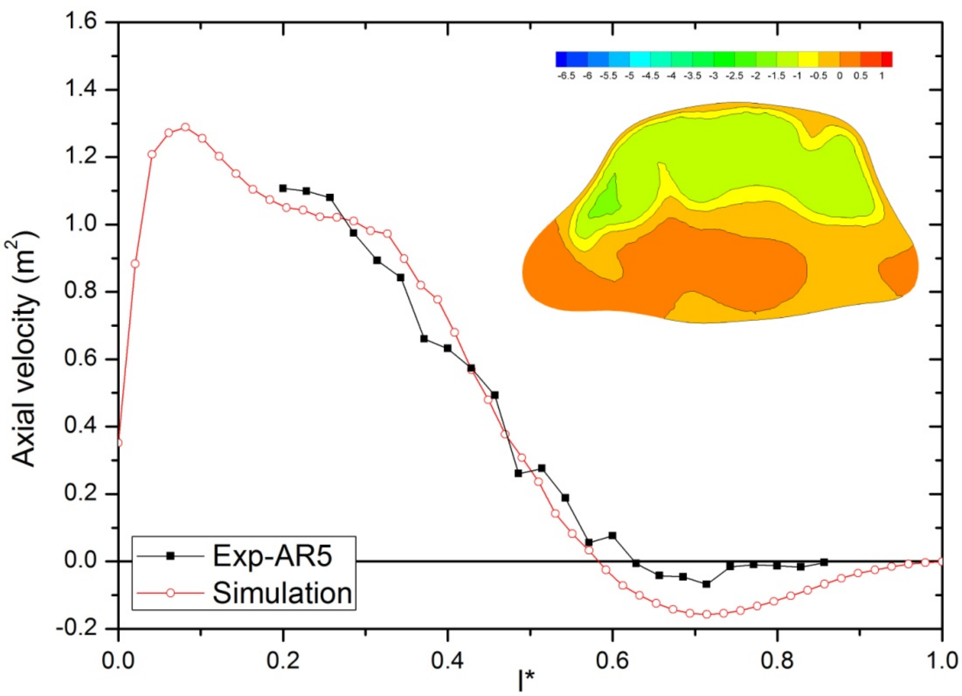

(f)

Fig.4.10. (a) Measured axial velocity profiles at right measuring line in five cross-sections; (b-f) comparison between measurement and calculation at five left measuring line (AR1-AR5).

4.2.2 Comparison between calculated and measured results

Velocity profiles were measured by LDA, and measurement locations are indicated in Figs. 4.5 and 4.6. Fig. 4.7a shows the measured velocity profiles in the model before surgery. The axial velocity distributions at five cross-sections illustrate a similar profile: it is higher near the posterior side due to the strong "pharyngeal jet" effect, and becomes weak and negative near the anterior wall induced by the reversed flow. Peak velocity was 5.8 m/s. Figs.9b-f compare experimental and simulated results in the five cross sections where radial distance has been normalized. Agreement of velocity profiles was in general excellent. The comparison of BC2 (Fig. 4.7c) shows the largest discrepancy near the interface of the main stream velocity and the reverse velocity, the most complex region. Due to the limitations of the technique, LDA measurements cannot capture velocity in close proximity to the wall, but show the same profile and value as calculated over the entire measurable region. LDA measurement is particularly able to capture reversed flow near the anterior wall as indicated by the weak and negative velocity, even though the discrepancy between calculation and measurement is large when very low velocity increases uncertainty of measurement.

For the model after surgery, there are five cross-sections, with three measuring lines at each cross-section. Figs. 4.8a, 4.9a and 4.10a show the measured velocity profiles along the measuring lines. At each cross-section, the velocity distributions along the left measuring lines show the same profile, as plotted in Fig. 4.8a. The highest velocity is about 1.4 m/s, and the profile exhibits a plateau indicating a uniform and weak "pharyngeal jet" flow. An inspection of Figs. 4.8b-f shows excellent agreement between measurement and simulation along the left measuring lines. The discrepancies are mainly in two regions: the first is found near the interface of the main stream velocity and the reverse velocity, the second discrepancy is at the reversed flow region due to the uncertainty of LDA measurement at very low velocity range. At the center and right measuring lines in each cross-section, as shown in Figs. 4.9b-f and Figs. 4.10b-f, the measured velocity profiles exhibit a similar trend, and the calculated velocity profile is quite consistent with that of LDA measurement. Most of the discrepancies are the same as in the left lines, except for the discrepancy at AC1 (Fig. 4.9b), in which the maximum velocity measured from the experiment is much higher than that from the simulation.

4.3 Discussion

The upper airway is very complex, and it is difficult to conduct in vivo measurements in the upper airway of OSA subjects. Even for in vitro measurements, there are many constraints when measuring the detailed velocity field, and most of the in vitro measurements have had to focus solely on pressure measurements. CFD is therefore a feasible method for studying the mechanism of OSA due to its non-invasive characteristics. Earlier work on CFD simulation in OSA upper airways used simplified geometry models and 1D/2D analysis, which could not predict flow features accurately. In the past years, simulations in realistic upper airway models based on CT/MRI scans have shown the potential of CFD in gaining a better understanding of flow characteristics and the pathogenesis of OSA. Many of the simulations used different turbulence models, including RANS and LES, to investigate airflow in OSA upper airways. The key barriers to simulation results are accuracy and reliability. Very few studies have managed to validate their simulation results against the measured pressure distribution, and velocity comparisons were not conducted owing to the difficulty of measuring velocity profiles in the upper airway. It was found that different turbulence models would produce a similar pressure distribution but totally different velocity fields (Lu et al., 2014). The current study is the first comparison of velocity profile between simulation and measurement in realistic upper airways with OSA. We have compared velocity profiles at different locations and cross-sections in OSA upper airway models for both before and after surgery. For the model before surgery, the simulation shows a strong "pharyngeal jet" flow downstream of the minimum cross section, and the LDA measurement captures the same velocity jump along the same measuring line. For the model after surgery, the "pharyngeal jet" flow becomes weak and uniform due to the widened airway, and LDA obtains the same velocity plateau along the same measuring line. The agreement in velocity profile between simulation and measurement is excellent, and gives us confidence in the CFD simulation in the upper airway, though the work still has some limitations. One potential limitation is the inability to capture flow near the wall (about 3mm), due to the intrinsic features of LDA analysis, and another is the discrepancy between measurement and simulation at reversed flow region, which is most likely caused by the uncertainty of LDA at low velocity range.

4.4 Conclusion

This study simulated flow using LES in OSA upper airway models for before and after surgery, and measured velocity profiles at different locations and cross-sections using LDA in the same 3-D printed upper airway models. The simulation and measurement have led to the following conclusions:

1. In the OSA upper airway model before surgery, there is a strong "pharyngeal jet" flow downstream of the minimum cross section. The LES simulation and LDA measurement can capture the same velocity jump along the same measuring line, even though there are discrepancies in value between simulation and measurement in the interface of the main stream velocity and the reverse velocity, which may be due to flow complexity, and in reversed flow region, which may be caused by uncertainty of LDA analysis at low velocity range.
2. In the model after surgery, the "pharyngeal jet" flow becomes weak and uniform, and simulation and measurement can produce the same velocity plateau in the same measuring line, even though there are some discrepancies in the reversed flow region and in the interface of the main stream velocity and the reverse velocity.
3. The LES simulation is consistent with the experimental measurement, and can be a reliable method for predicting the flow characteristics associated with OSA upper airways.

Chapter 5 Comparison of flow patterns between successful and failed surgeries

In this chapter, we have carried out CFD simulation using LES model in upper airway models of one normal subject and four OSA subjects in which three of them had successful surgery and one was failed in UPPP surgery. The objective is to investigate the reason of surgery failure in fluid mechanics point of view, further understand the mechanism of OSA, and provide useful guideline for surgical treatment planning.

5.1 Method

The investigation has been approved by the local ethics committee and is performed in accordance with the Declaration of Helsinki, and the subjects are provided with written informed consent forms.

Four severe OSA subjects were selected to carry out the study, among them three had successful UPPP surgery and one had failed surgery. The variation of AHI of each subject before and after surgery are tabulated in Table 5.1, where Subject #4 had failed surgery whose AHI increased from 46.1 to 81.7.

5.1.1 Construction of upper airway model

All the four OSA subjects were adult males who were suffered severe OSA before treatment, and whose parts of soft palate or uvula were removed by UPPP surgery. CT-scan was performed using a single-slice helical CT scanner (Phillips, Brilliance 64) in the affiliated Beijing Tongren Hospital, Capital Medical University. The images were obtained in the axial plane with a resolution of 0.7×0.7 mm2, and slice thickness was 0.625 mm. The three-dimensional point cloud data of upper airway models were reconstructed using the image processing software Mimics from nasal cavity to the laryngopharynx .

5.1.2 Numerical Method

The flow field is solved by a CFD solver Fluent (ANSYS 14.5) with LES model. The air flow is assumed as incompressible flow due to the very low Mach number (Mach < 0.3). Only inspiratory process with tidal volume measured with spriometry is studied and the breathing frequency is 12 cycles per minute following a sinusoid. Six periods (about 15 seconds) was simulated and flow pattern analysis was conducted by selecting the data in the time of peak flow (5.5s). The inlet and outlet were extended to minimize the velocity boundary effect, the inlet velocity profile is fitted from the real inhaled data and the outlet pressure boundary condition is set as zero. No-slip boundary condition is applied on the wall of airway and the time step is 0.001s. Second-order finite-volume schemes were employed for discretizing the flow government equations on the computational domain. The time-integration was performed using second-order implicit discretization, the coupling between the pressure and the velocity field was implemented through the SIMPLE algorithm.

The local Reynolds number ($Re=UDeq/\upsilon$) ranged from 900 to 3200 according to the equivalent diameter (Deq) of the cross-sectional area, the flow velocity (U) computed from the bulk flow rate and the kinematic viscosity of the air (υ). The Reynolds number represents that the flow is from laminar to turbulent. Therefore, the WALE sub-grid scale (SGS) model is employed in the LES modeling because of its better ability for predicting the transition from laminar to turbulent regimes (Weichert et al. 2010).

The mesh was generated using ICEM (ANASYS 14.5). The meshes are hybrid hexahedral/tetrahedral elements and refined mesh has been employed near the oropharynx and the numerical results of velocity are mesh-convergent to within a prescribed tolerance (~0.2%). The number of mesh element is around 3.0 million depending on the size of each upper airway.

5.2 Results

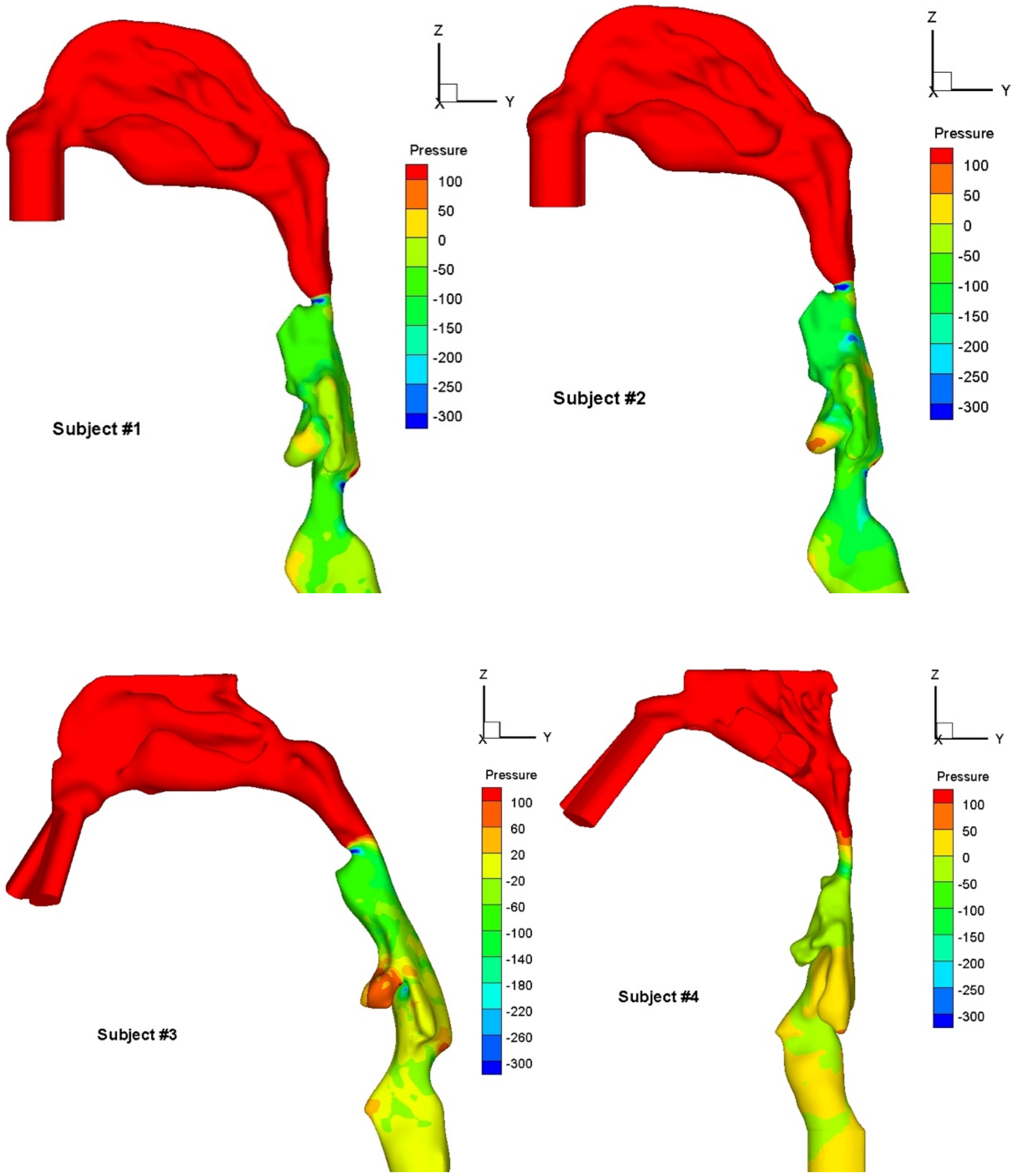

Fig.5.1. The wall pressure distribution in the four models before surgery.

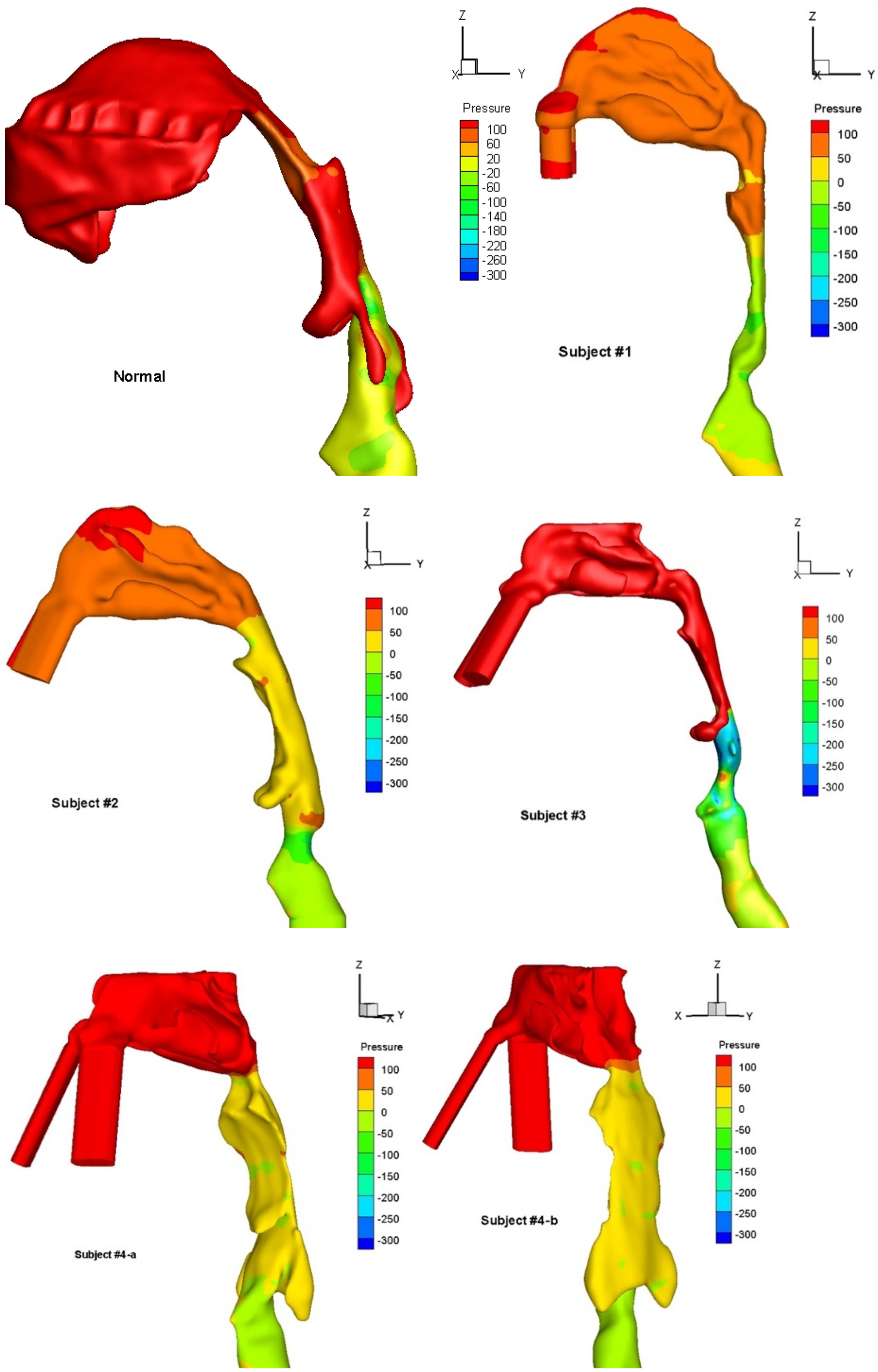

Fig.5.2. The wall pressure distribution in normal subject and four OSA subjects after surgery, the last two patterns represent two different views of subject #4.

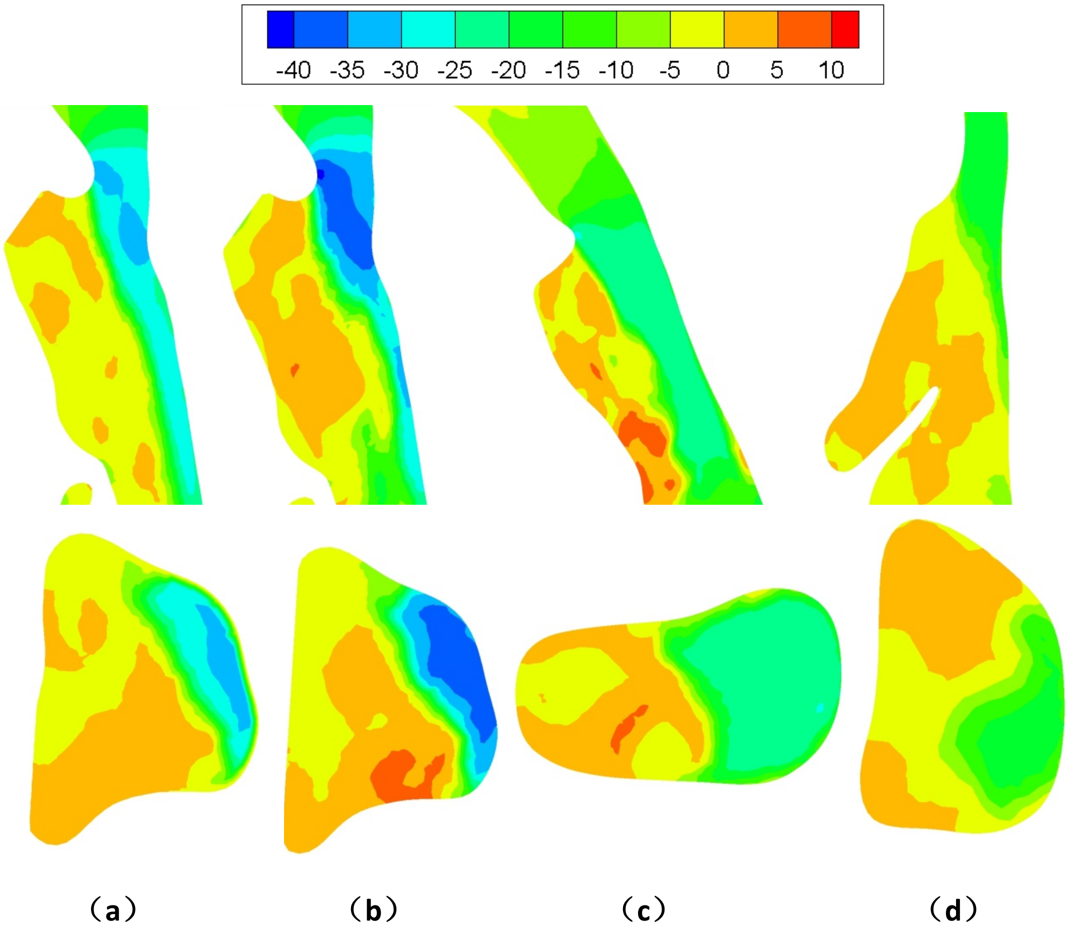

Fig.5.3. The axial velocity distribution and path-line along the sagittal plane and the axial velocity pattern of a cross section plane marked in the sagittal plane for all subjects before surgery.

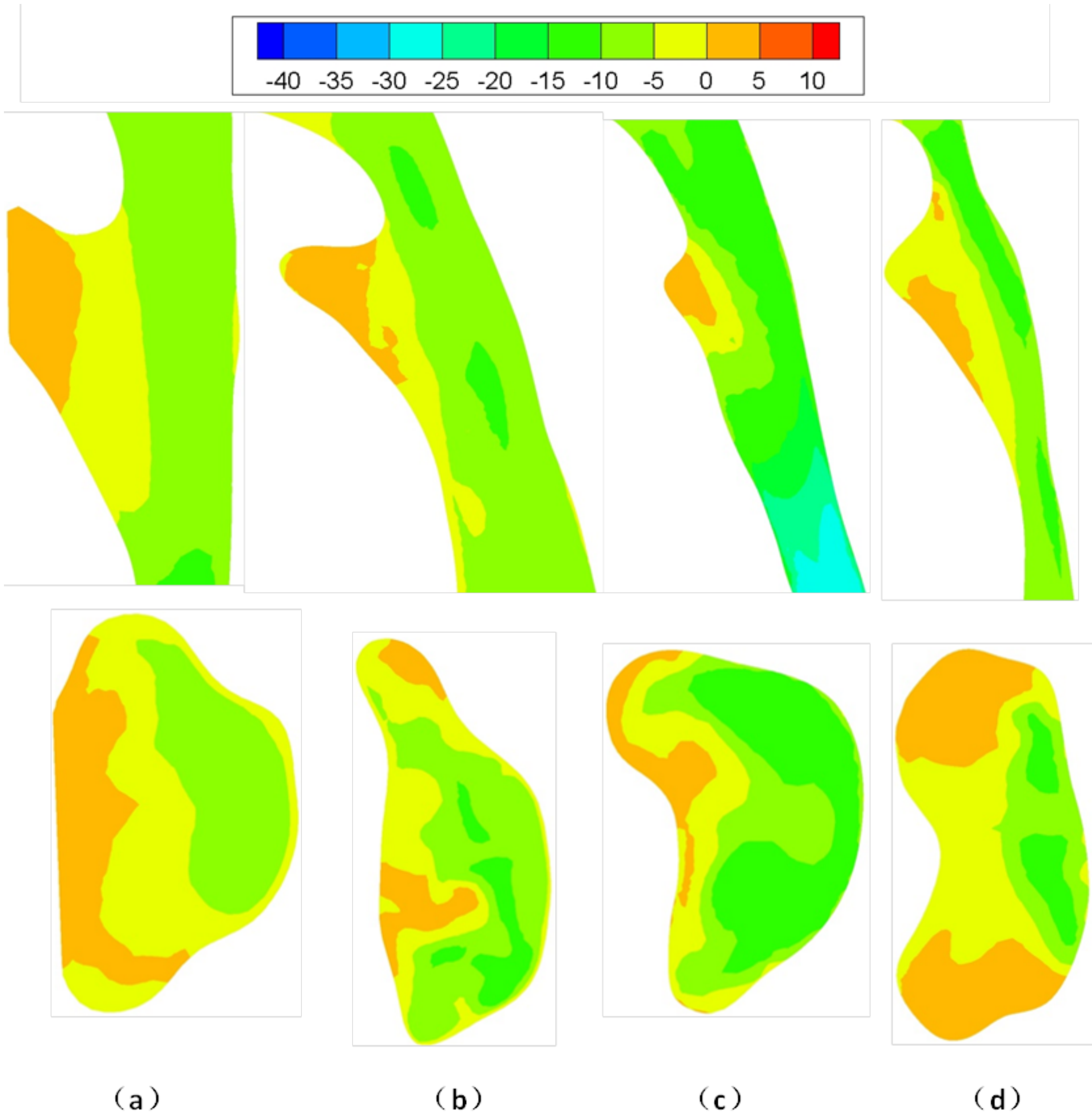

Fig.5.4. The axial velocity distribution and path-line along the sagittal plane and the axial velocity pattern of a cross section plane marked in the sagittal plane for all subjects after surgery.

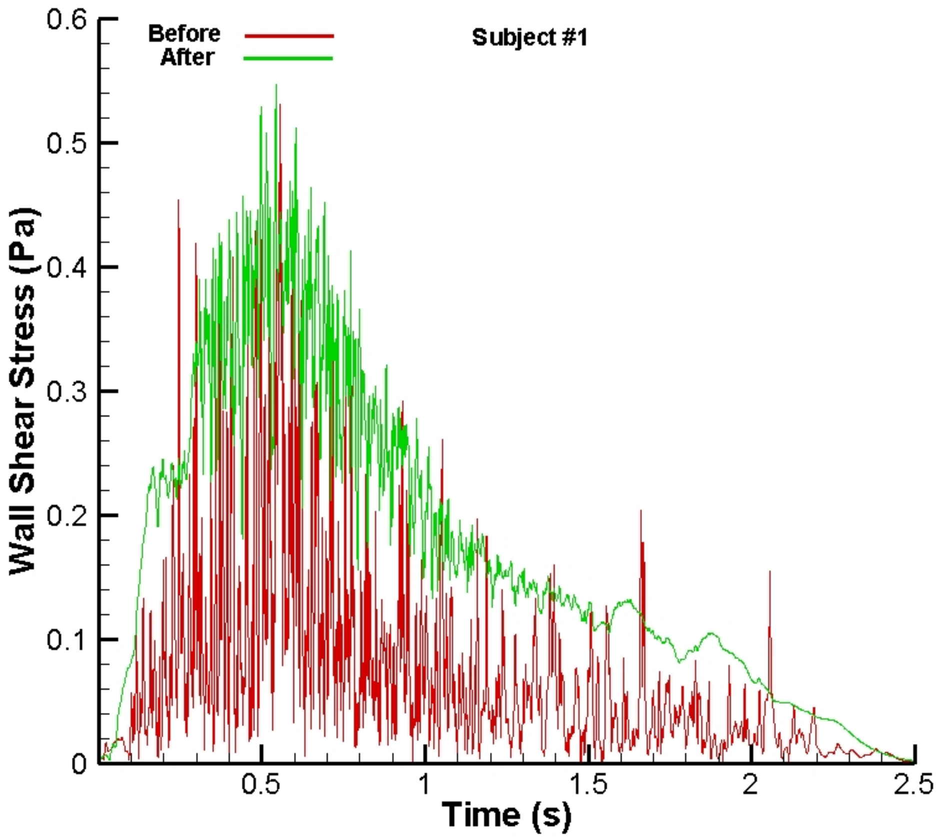
Before
After
Subject #1
Wall Shear Stress (Pa)
0
0.1
0.2
0.3
0.4
0.5
0.6
0.5
1
1.5
2
2.5
Time (s)

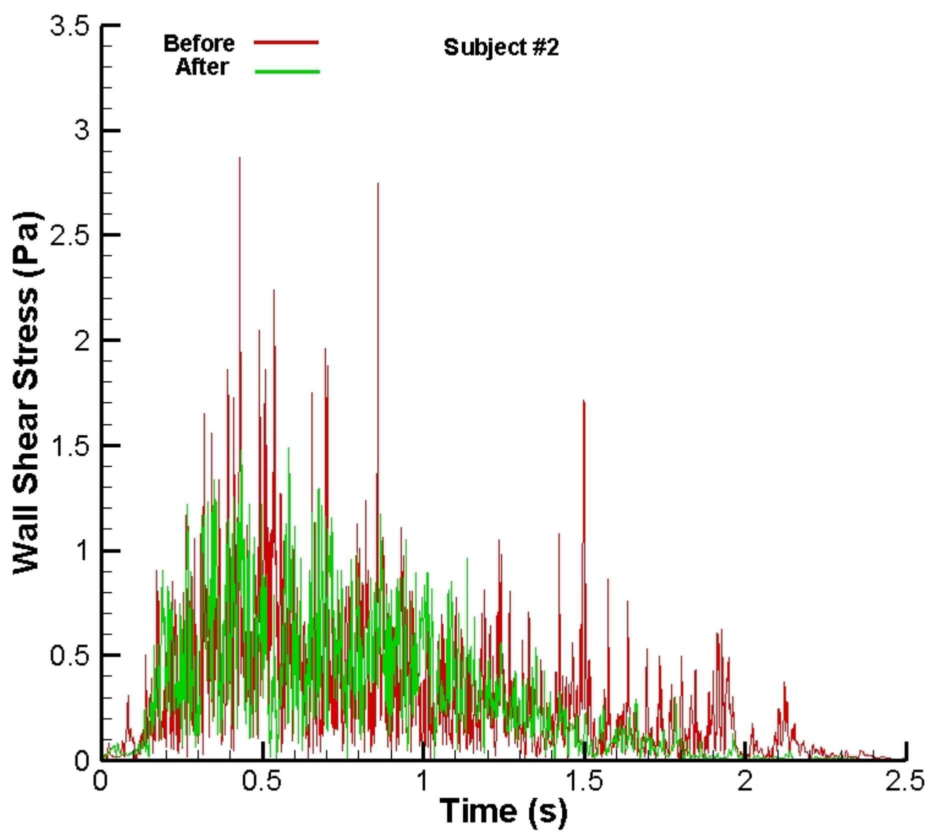
Before
After
Subject #2
Wall Shear Stress (Pa)
0
0.5
1
1.5
2
2.5
3
3.5
0
0.5
1
1.5
2
2.5
Time (s)

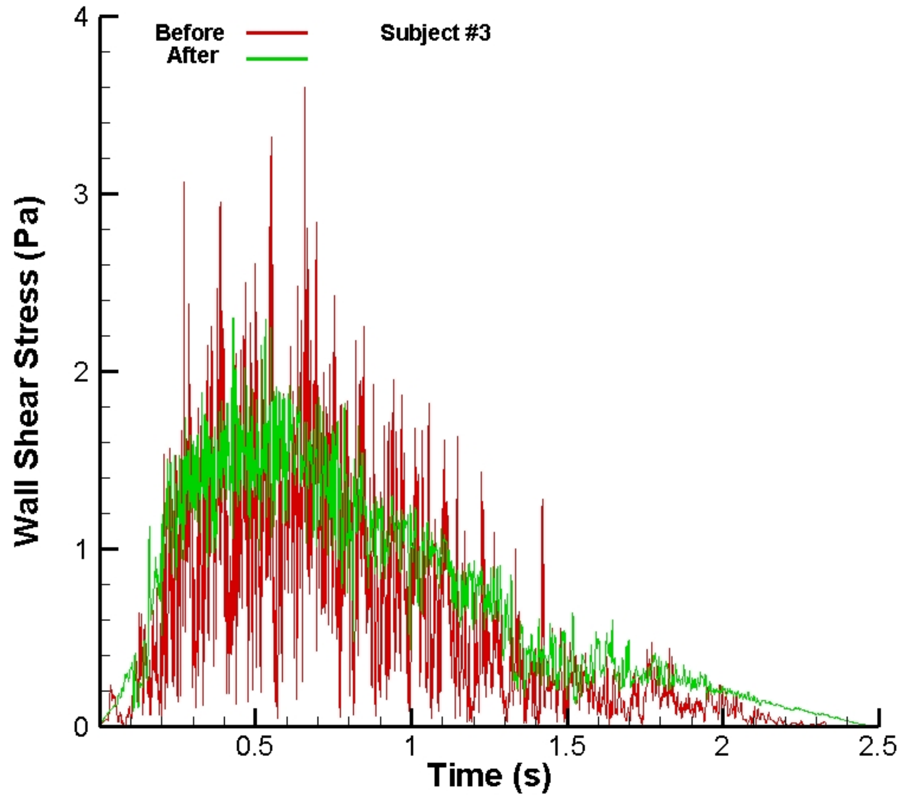

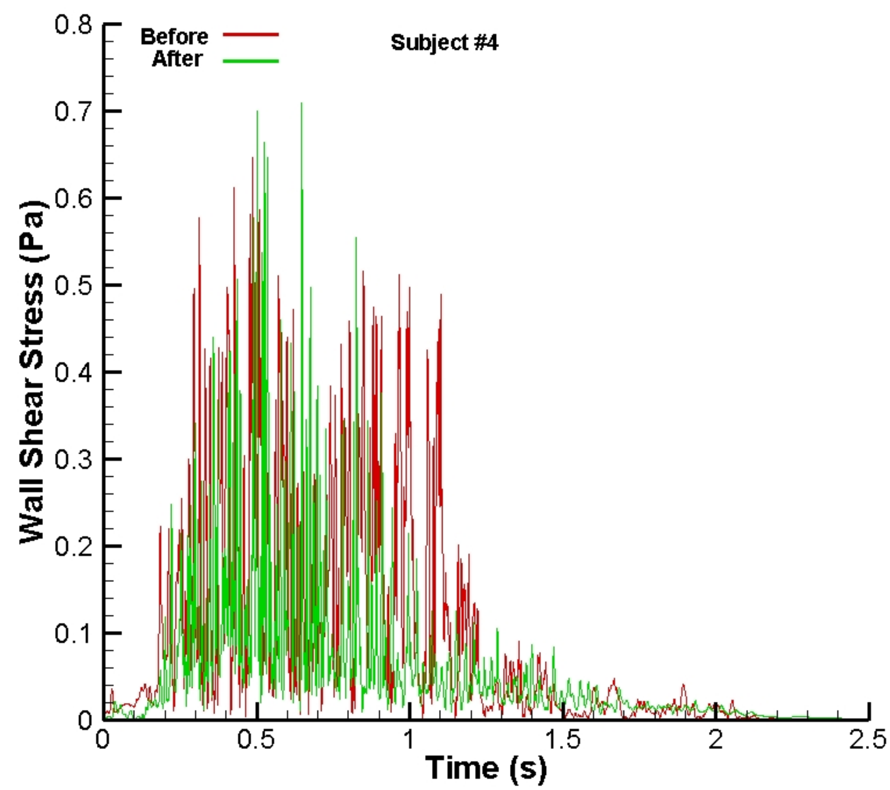

Fig.5.5. Comparison of wall shear stress time series at the oropharynx for all the subjects.

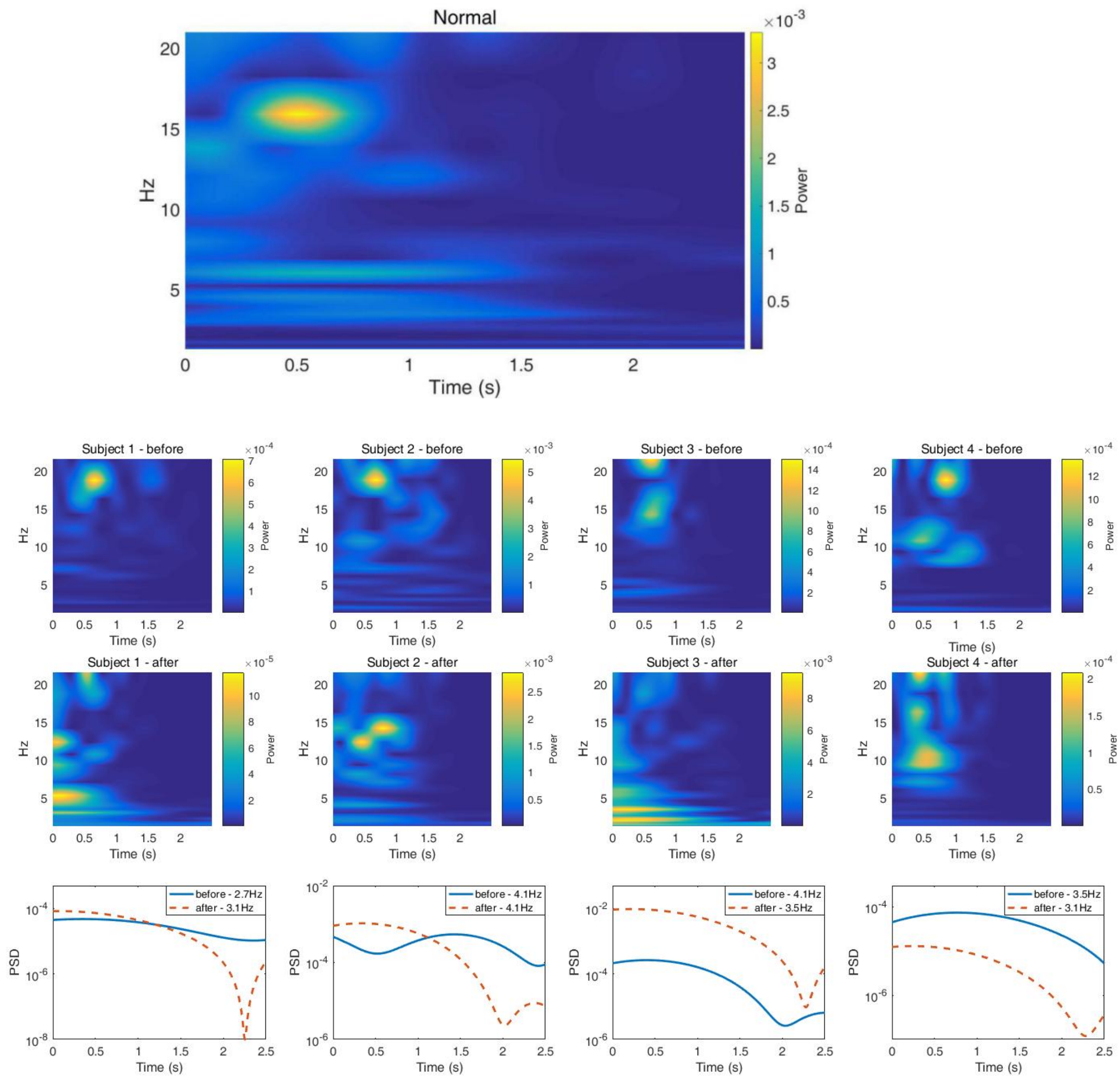

Fig.5.6. Wavelet analysis of wall shear stress time series at oropharynx for all the subjects, pre- and post- treatment.

Table 5.1 AHI measurement of OSA subjects

	Before surgery	After surgery
Subject #1	64.8	15.8
Subject #2	60.7	23.9
Subject #3	41.1	2.9
Subject #4	46.1	81.7

Table 5.2 AHI, minimum cross-section area near the retro-palate, maximum cross-section area in the oropharynx, area ratio (AR) (min/max) and the AR change (after/before).

	AHI	Min Area (mm^2)	Max Area (mm^2)	Area-Ratio (AR=Min/Max)	AR Change (After/Before)
Subject #1	64.8	53.2	256.4	0.21	2.00
	15.8	111.1	264.1	0.42	
Subject #2	60.7	46.1	241.8	0.19	2.58
	23.9	318.1	645.0	0.49	
Subject #3	41.1	66.7	149.2	0.45	1.67
	2.9	250.7	336.3	0.75	
Subject #4	46.1	49.5	191.7	0.26	0.96
	81.7	92.6	370.9	0.25	

In upper airway with OSA, the most apparent feature for collapsing is a large negative pressure occurs in the minimum cross-section near the retro-palate. Fig. 5.1 shows that there exists a large negative pressure in the anterior side of the wall in the models before surgery for all subjects. The maximum pressure drop from choanae to the minimum cross-section is 680 Pa, 980Pa, 790 Pa and 320 Pa for subject #1 to #4, respectively, indicating a high flow resistance.

After the surgical treatment, it is shown in Fig. 5.2 that the large negative pressure is changed to positive near the retro-palate in the models of subject #1 - #3 who had successful surgery which is similar to the normal subject. However, for the model of subject #4 who had failed surgery, the negative pressure still exists near the retro-palate and extended to the wall of oropharynx for both the anterior and posterior side. This would cause two collapse regions: one is near the retro-palate, and the other could be found in the oropharynx. The failed elimination of the negative pressure near the retro-palate should cause the failure of surgery while the additional negative pressure in the oropharynx would make it worse. The maximum pressure drop from choanae to the cross-section near the retro-palate is 47 Pa, 100Pa, 120 Pa and 140 Pa respectively for subject #1 to #4 (Fig. 5.2). To quantified the results, the Pearson's correlation analysis was conducted, and a statistically significant correlation (Altman, 1991) was found (r = -0.723, p = 0.043 < 0.05) between AHI and the maximum pressure drop from choanae to the cross-section near the retro-palate.

Fig. 5.3 shows the axial velocity distribution at the sagittal-plane and cross-section at downstream of minimum area for OSA upper airway models before surgery. A strong jet-like axial velocity represented by dark blue color develops behind the soft-palate for all subjects due to the anatomical narrowing of the upper airway. According to the

Bernoulli equation, this high momentum axial velocity would result in a low pressure when the pressure reach to a critical value, it will below zero and change into a negative pressure as is shown in Fig. 5.1. From contours at cross-sections, the high momentum flow occupies only small portion of the airway, and the induced reversed flow occupies most of the airway.

After surgical treatment, the jet flow in subject #1 - #3 has been weakened significantly as a result of widening airway as shown in Fig. 5.4. From contours at cross-sections, the jet flow occupies most of the airway, and there is a single main reversed flow region which occupies less than half of the airway. However, the jet flow is still strong for subject #4 even it becomes weaker than that before surgery, and there are two main reversed flow regions due to the morphological change. For four upper airway models before surgery, the flow path-lines show that the high momentum jet flow induces several small recirculations and circulation patterns are irregular. For subject #1 - #3 after surgery, a single dominant recirculation stands near the wall and the pattern is regular. It is indicated that the successful surgery would change the morphology of upper airway to result in a single dominant recirculation. For subject #4 after surgery, there are two dominant recircualtions even the patterns are regular.

The wall shear stress time series is shown in Fig. 5.5, with the monitor point at the anterior side of cross-section in the oropharynx. For subject #1 - #3, before surgery, the wall shear stress time series does not follow the breathing pattern and exhibits irregular behavior; after surgery, the time series follows closely the breathing curve and exhibits regular pattern. For subject #4, the time series of both before and after surgery does not follow the breathing curve and exhibits irregularly. It is found that for subjects before surgery, the flow separation before the larynx induced several small reverse flows, every of which is quite weak, consequently results a lower wall shear stress. For successful surgery, a single dominant reverse flow becomes quite strong results a higher wall shear stress. .

Because characteristics of air flow signals change continuously, it is better to perform spectral analysis using the wavelet transform. A wavelet is a function with zero mean and that is localized in both time and frequency domain (Torrence C, 1998). This feature allows us to determine both the dominant modes of BFO and how those modes vary in time. Wavelet transform of a signal yields a three-dimensional structure above the time-frequency plane. Usually, the wavelet amplitude and power spectrum can be defined as the absolute values of the wavelet transform and their squares, respectively (Torrence C, 1998). For upper airway air flow signals, Morlet wavelet is a good choice, since it provides a good balance between time and frequency localization.

As In the windowed Fourier transform, one begins with a window function, which called a mother wavelet $\Psi(u)$. This function introduces a scale (its width) into the analysis. Commitment to any particular scale is avoided by using not only $\psi(u)$, but all possible scaling of $\psi(u)$. The mother wavelet is also translated along the signal to achieve time localization. Thus, a family of generally nonorthogonal basis functions:

$$\Psi_{s,t} = |s|^{-p}\psi(\frac{u-t}{s}) \qquad (5.2.1)$$

Where p is an arbitrary nonnegative number. The prevailing choice in the literature is p=1/2 (I.Daubechies, 1992). The use of scaled and translated version of a single function was proposed by Morlet in the analysis of seismic data. The continuous wavelet transform of a signal $g(u)$ is defined as:

$$\tilde{g}(s,t) = \int_{-\infty}^{\infty} \bar{\Psi}_{s,t}(u)g(u)du \qquad (5.2.2)$$

The wavelet transform $\tilde{g}(s, t)$ is a wavelet coefficient and t is time, s is the scale related to the frequency f as $f = f_0/s$, and f_0 determines the current frequency resolution. By choosing f_0 =1, we obtain the simple relation f =1/s. The continuous wavelet transform is a mapping of the function $g(u)$ onto the time frequency plane. By adjusting the window used in wavelet transform, slower and faster events can be categorized accordingly (Kvenmo et.al, 1999). This method breaks down the steady fluctuating time series into its frequency elements and computes the power of signal components in predetermined frequency bands, allowing to measure the amplitude of different flow motion waves in PU/Hz.

In previous study, we have found the PSD peaks around 3~5 HZ in all subjects with and without OSA (Liu et al. 2012). This peak PSD phenomenon is found in the wavelet transform figures as is shown in figure 5.6. All these peak frequencies were selected to analyse the vary of PSD along time. As is shown in figure 5.6 that, after the successful OSA surgery displayed higher PSD value in these peak frequencies than before surgery.

The AHI is correlated to the flow pattern that in turn is strongly dependent on the morphological change. To compare easily the effect of cross sectional area change on AHI, we summarize the AHI, minimum cross-section area near the retro-palate, maximum cross-section area in the oropharynx, theirs area ratio and AR changes in Table 5.2. It is worthy to note that there were no correlations between the increase in minimum cross-section area and AHI change, which is different from the correlation analysis in Mandibular advancement (MMA) (Zhao et al. 2013b).

5.3 Discussion

UPPP is a common method for OSA treatment in which the morphology change is crucial for surgery success. The prediction of the flow pattern in upper airway is crucial for improving the success rate of upper airway surgery. Invasive method to study the upper airway flow characteristics of OSA subjects is generally not applicable in the clinical practice. CFD is the best tool for prediction of flow pattern in upper airway and surgical treatment planning.

Many researchers studied the flow in upper airway of OSA patients with CFD simulation, however, no one compared the difference between successful and failed surgery models (Luo et al. 2004; Mylavarapu et al. 2009; Powell et al. 2011; Mihaescu et al. 2008). LES has been validated for being a good method to predict flow features in the upper airway (Lu et al. 2014). Therefore, in this study we have simulated using

LES and compared flow features in different upper airway models for both before and after surgery and for both successful and failed surgery. For models before surgery, the flow pattern is irregular, there are several recirculations in the reverse flow region, and the oscillation of the wall shear stress time series is strong but irregular and does not follow the breathing curve, indicating that the oscillation of time series is strongly influenced by the multiple recircualtions in reverse flow region. For models after successful surgery, the flow pattern is regular, and a single dominant recirculation is induced at the downstream of the minimum cross-section, and the oscillation profile of the wall shear stress time series is regular and follows the breathing curve closely, indicating that the regular oscillation profile is induced by the dominant recirculation. For the model after failed surgery, there are two main recirculations due to the morphological change, the oscillation of wall shear stress time series is strong but does not follow the breathing curve. From the comparison of the flow patterns, we can find that upper airway surgery has improved the regularity of flow pattern of the reversed flow, i.e., in the model with lower AHI, the reversed flow pattern is more regular and there exists a single dominant recirculation at oropharynx.

We found experimentally an intrinsic peak frequency (3~5 Hz) for the normal subject resulted from the flow separation downstream the minimum cross-sectional area (Liu et al. 2012). The current CFD simulation can capture the similar peak frequency in most of the models, but for the subject #4 model after failed surgery, the peak frequency is 31.6 Hz and the component in the range of 3 ~ 5 Hz is quite weak.

The flow resistance or pressure drop has a significant effect on OSA. Wootton et al. (2014) analysed numerically 15 pairs of obese OSA children, they found that the flow resistance in the pharynx and pressure drop from choanae to a minimum cross- section significantly correlated to the AHI, airway minimum cross-sectional correlation to AHI was weaker and the airway wall minimum pressure was not significantly correlated to AHI. Their conclusion is consistent with our result in this study. Different from the correlation analysis in MMA by Zhao et al., 2013b, for UPPP surgery, we did not observe a significant correlation between the increase of the minimum cross-section area and the change of AHI.

5.4 Conclusion

CFD has been considered as a useful tool for predicting the outcome of OSA treatment of the patients who were received the UPPP surgery. Compared the flow pattern in upper airway between successful and failed subjects by using LES model of CFD, the following results can be concluded:

1. All upper airway model of four OSA subjects exist a large negative pressure in the anterior side of the wall, which indicating a high flow resistance. For successful surgical treatment, the large negative pressure has changed to positive near the retro-palate. However, for the failed surgery treatment, the negative pressure still exists near the retro-palate and even extended to the wall of oropharynx for both the anterior and posterior side. The failed elimination of the negative pressure near the retro-palate should cause the failure of

surgery while the additional negative pressure in the oropharynx would make it worse.

2. In terms of the axial velocity distribution, for the successful subjects, a single dominant recirculation stands near the wall and the pattern is regular. For the failed subject, there are two dominant recircualtions even though the patterns are regular indicating that one dominant recirculation should be a feature of a successful surgery.
3. The wall shear stress time series also shows apparent different patterns between successful and failed surgery outcomes and the wavelet analysis of the wall shear stress time series consistent with our research before(Liu et al. 2012) and after the successful OSA surgery the PSD displayed higher value in these peak frequencies than before surgery.
4. The statistically significant correlation (Altman, 1991) was found ($r = -0.723$, $p = 0.043 < 0.05$) between AHI and the maximum pressure drop from choanae to the cross-section near the retro-palate. However in our study we did not found the correlations between the increase in minimum cross-section area and AHI change, which is different from the correlation analysis in Mandibular advancement (MMA) (Zhao et al. 2013b).

Chapter 6 Stochastic resonance in spontaneous breathing

The stochastic resonance (SR) is a phenomenon that addition of noise in a nonlinear system can enhance the response of weak signal transmission significantly. Strategies of perioperative airway management of patients with OSA should be based on understanding of pathophysiology of upper airway obstruction. According to the Starling resistor model, the airway would occlude whenever pressures both upstream and downstream fall below a critical pressure. In another word, the breathing is unobstructed when the pressures both upstream and downstream is higher than that around the tissue of the oropharynx. We found inspiratory flow oscillates due to flow separation near the larynx in normal and OSA subjects, but the oscillation is weak in OSA subjects (Liu et al. 2012). In this chapter we assume the flow turbulent fluctuation as the input noise signal, the various intensities of this intrinsic noise generation could perform the SR phenomenon. If it is the case, the SR may play a role in enhancing the periodic flow oscillation due to the flow separation for controlling the spontaneous breathing. In this study, firstly, we have selected six adult normal subjects to investigate the possible SR phenomenon in spontaneous breathing of adults experimentally in a standard anechoic chamber. Then one of the typical normal subject and three OSA subjects are measured in the hospital accurately to compare the different SR pattern between normal and OSA subjects. Among them, two OSA subjects were conducted successful uvulopalatopharyngoplasty (UPPP) surgery and one is suffering severe OSA. The correlation between apnea-hypopnea index (AHI), the OSA severity, and flow oscillating signal SNR is evaluated experimentally. This will help to gain new insights into the mechanism of OSA and provide quantitative basis for evaluating the quality of spontaneous breathing control.

6.1 Method

The investigation has been approved by the local ethics committee and is performed in accordance with the Declaration of Helsinki, and the subjects are provided with written informed consent forms.

There were two experiments. In the first experiment, six normal subjects were selected to carry out the pressure measurement in mouth by microphone in a standard anechoic chamber for investigating the possible SR phenomenon for adult in spontaneous breathing. A sampling rate of 25 kHz was used, and the measuring time was 20 seconds. In the second experiment, a awaken normal subject and three asleep OSA subjects were selected to carry out accurate pressure measurement in the hypopharynx using pressure catheter sensor in the hospital. The sampling frequency was 128 Hz. The detailed experimental method and procedure were described in our previous paper (Liu et al. 2012).

The measured time series are analyzed by Fast Fourier Transformation (FFT). For a real signal f(t), if we regard it as an ergodic process, its autocorrelation is defined by (Papoulis and Pillai 2002):

$$R(\tau) = \lim_{T\to\infty} \frac{1}{T} \int_{-T/2}^{T/2} f(t) f(t-\tau) dt \quad , \tag{6.1}$$

and its correlation coefficient is defined by:

$$r(\tau) = \frac{\lim_{T\to\infty} \frac{1}{T} \int_{-T/2}^{T/2} \left[\left(f(t) - \mu \right) \left(f(t-\tau) - \mu \right) \right] dt}{\sigma^2} \quad , \tag{6.2}$$

where μ and σ are the mean and variance of the signal $f(t)$ and given by,

$$\mu = \lim_{T\to\infty} \frac{1}{T} \int_{-T/2}^{T/2} f(t) dt \quad , \quad \text{and} \quad \sigma^2 = \lim_{T\to\infty} \frac{1}{T} \int_{-T/2}^{T/2} \left[f(t) - \mu \right]^2 dt \quad . \tag{6.3}$$

The power spectral density (PSD) can be obtained by imposing Fourier transform (FT) on R(τ) (Narasimhan and Veena 2005),

$$S(\omega) = \int_{-\infty}^{\infty} R(\tau) e^{-i\omega\tau} d\tau \quad . \tag{6.4}$$

On the other hand, if we impose on r(τ), since

$$r(\tau) = \frac{1}{\sigma^2} R(\tau) - \frac{\mu^2}{\sigma^2} , \tag{6.5}$$

we can get

$$s(\omega) = \int_{-\infty}^{\infty} \left[\frac{1}{\sigma^2} R(\tau) - \frac{\mu^2}{\sigma^2} \right] e^{-i\omega\tau} d\tau = \frac{1}{\sigma^2} S(\omega) - 2\pi \frac{\mu^2}{\sigma^2} \delta(\omega) \quad , \tag{6.6}$$

where $\delta(\omega)$ is Dirac function. Therefore, if $\omega \neq 0$, $s(\omega)$ and $S(\omega)$ have only difference of a coefficient and consequently could be considered as the same one for analysis though $s(0)$ and $S(0)$ are very different. Thus, in this study we also call $s(\omega)$ as PSD.

6.2 Results

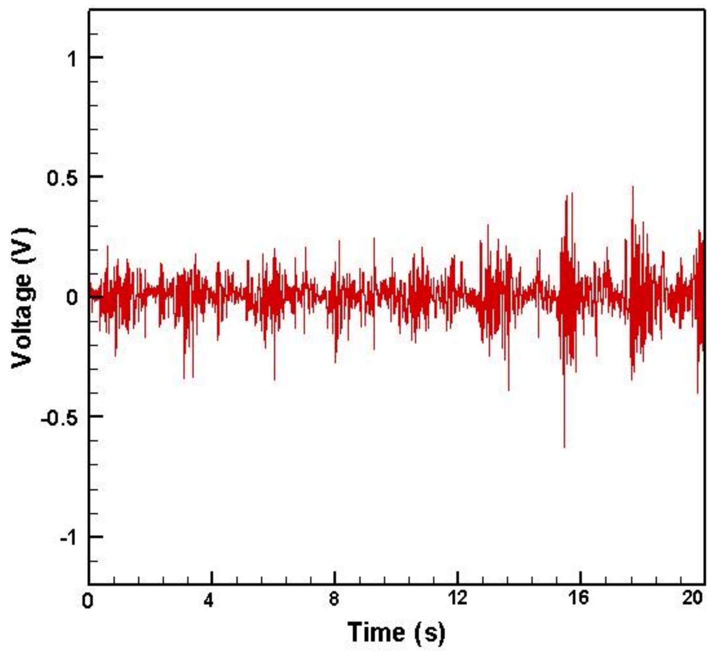

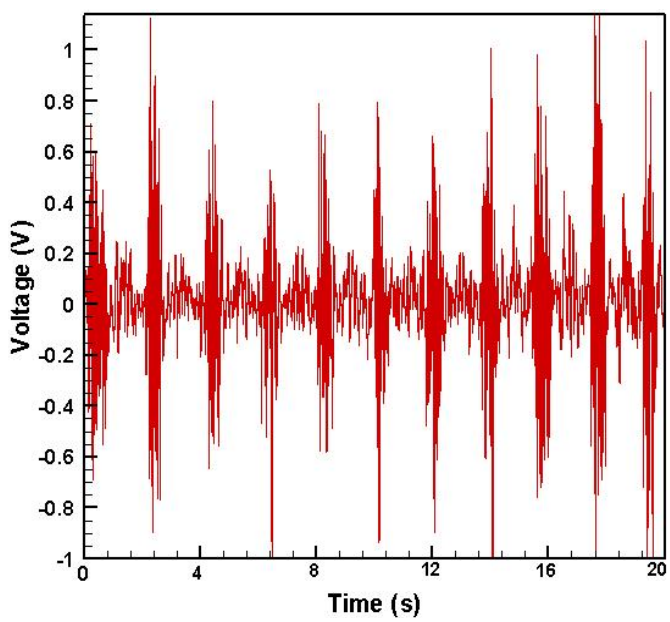

Fig.6.1. Time series of measured pressure variation for spontaneous (left) and volitional (right) breathing measure by microphone in anechoic chamber.

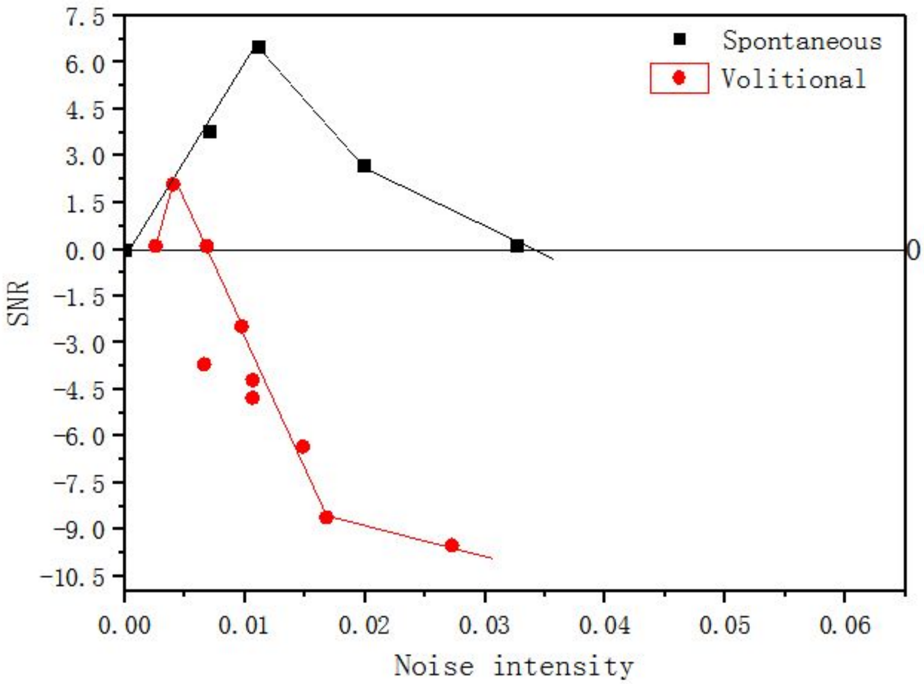

Spontaneous
Volitional
SNR
Noise intensity
7.5
6.0
4.5
3.0
1.5
0.0
-1.5
-3.0
-4.5
-6.0
-7.5
-9.0
-10.5
0.00
0.01
0.02
0.03
0.04
0.05
0.06
0

(a)

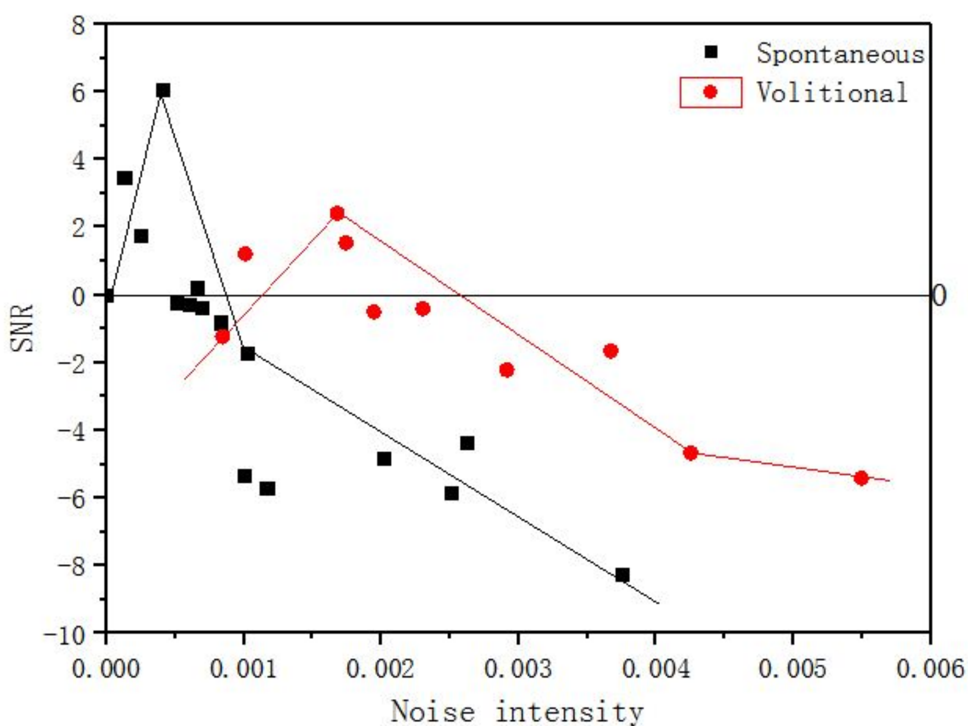

Spontaneous
Volitional
SNR
Noise intensity
8
6
4
2
0
-2
-4
-6
-8
-10
0.000
0.001
0.002
0.003
0.004
0.005
0.006
0

(b)

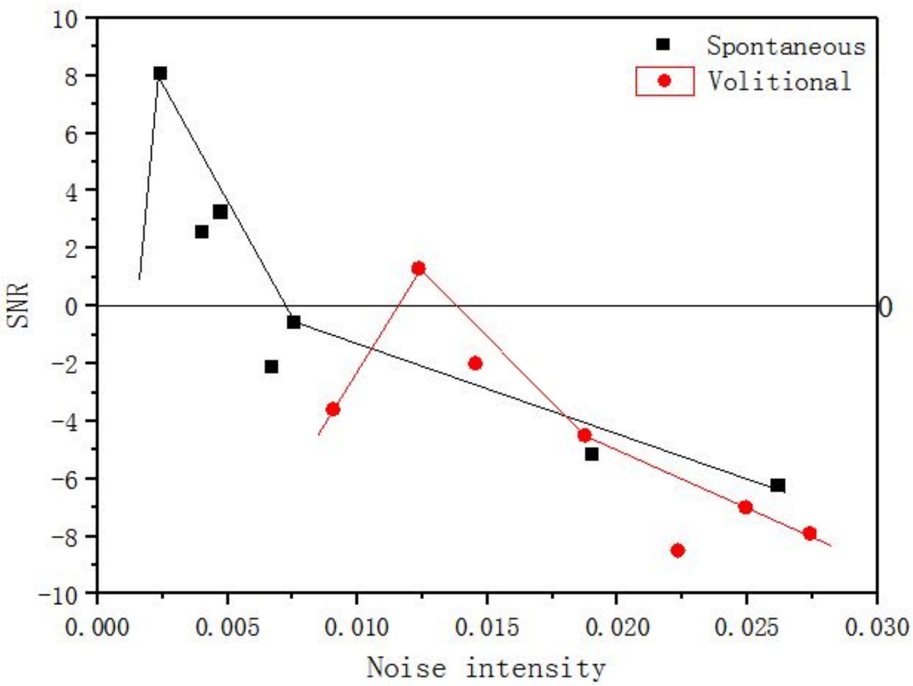

Spontaneous
Volitional
SNR
Noise intensity
10
8
6
4
2
0
−2
−4
−6
−8
−10
0.000
0.005
0.010
0.015
0.020
0.025
0.030

(c)

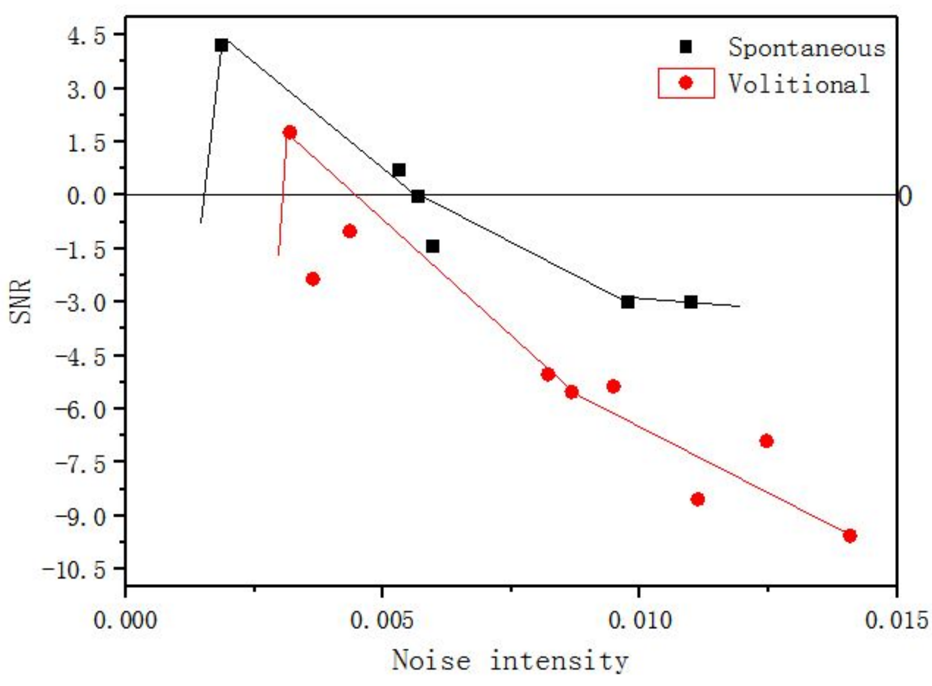

Spontaneous
Volitional
SNR
Noise intensity
4.5
3.0
1.5
0.0
−1.5
−3.0
−4.5
−6.0
−7.5
−9.0
−10.5
0.000
0.005
0.010
0.015

(d)

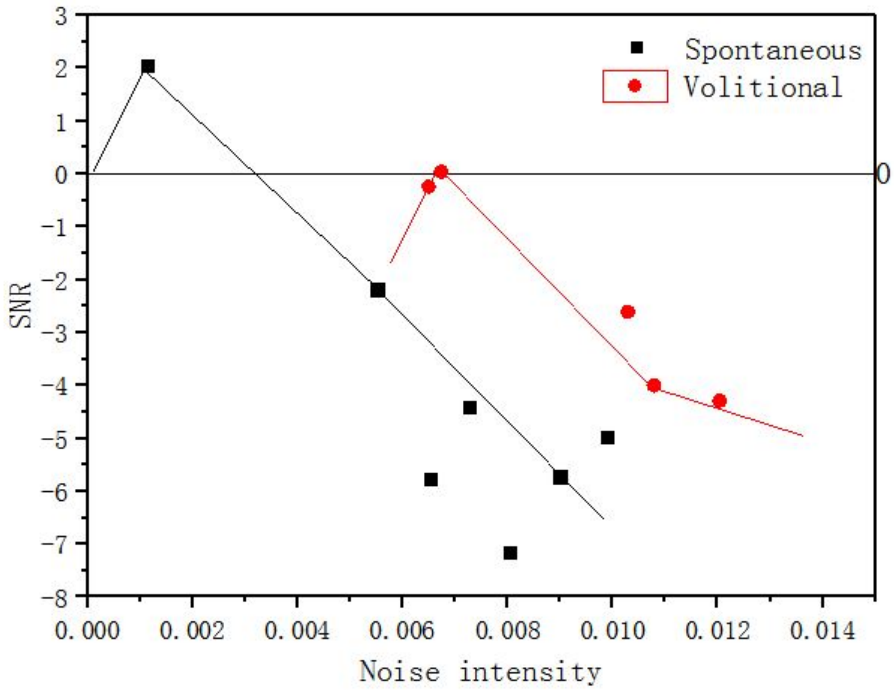

(e)

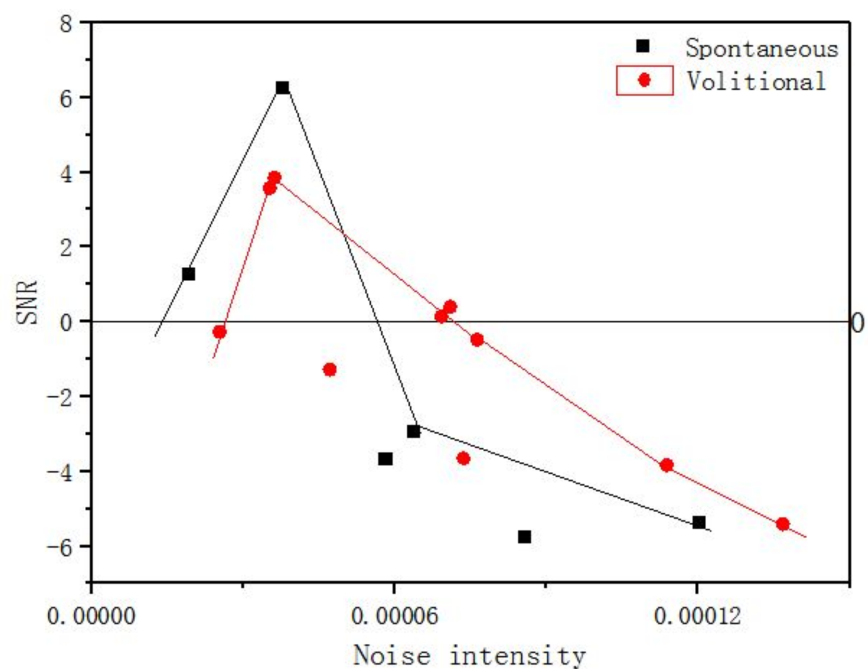

(f)

Fig.6.2. SNR distribution with noise intensity for both spontaneous and volitional breathing of six normal subjects. (a) Subject 1; (b) Subject 2; (c) Subject 3 (d) Subject 4; (e) Subject 5; (f) Subject 6.

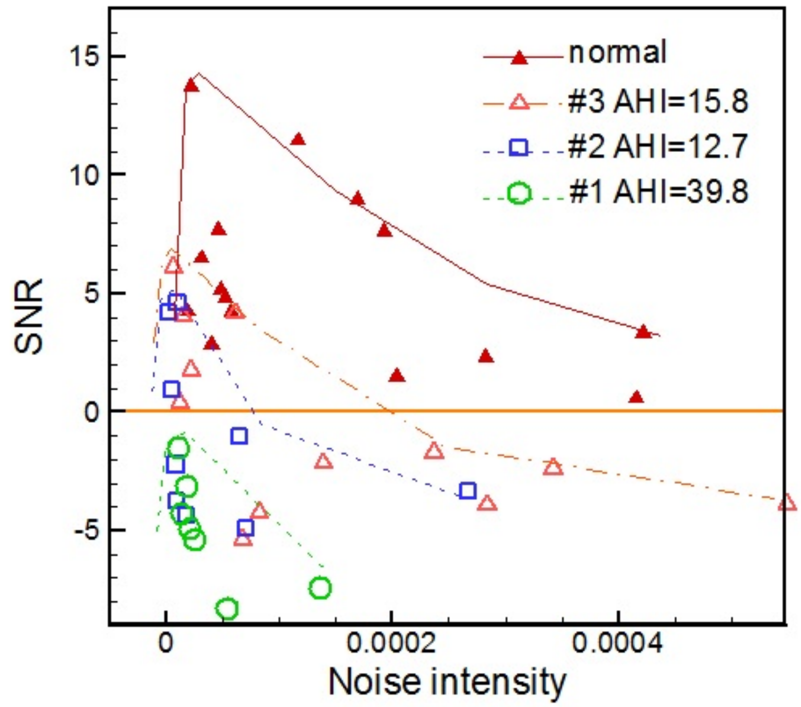

(a)

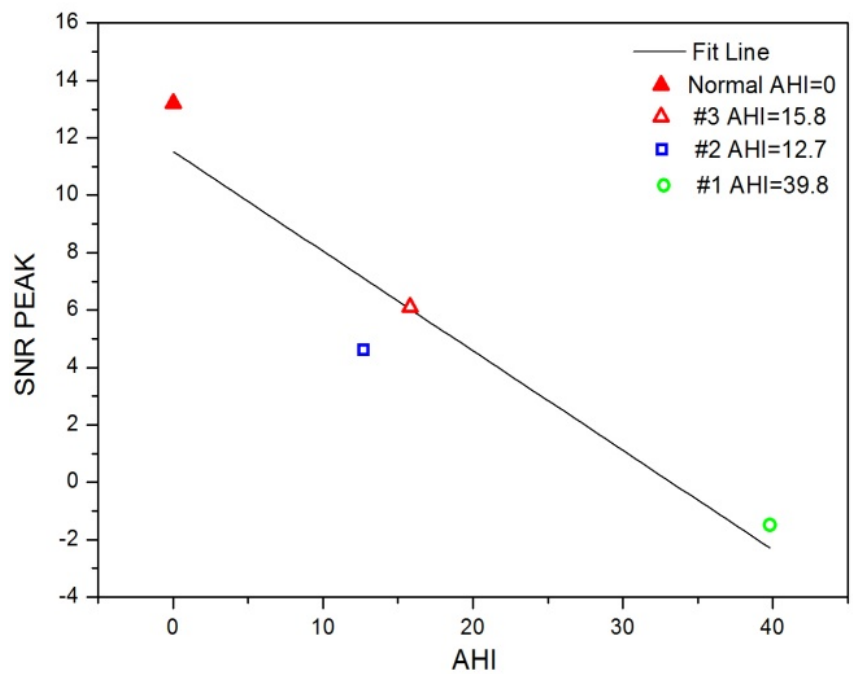

(b)

Fig.6.3. (a) SNR distribution with noise intensity measured by catheter for normal and OSA subjects. (b) Regression fit between peak of the SNR and AHI.

6.2.1 The stochastic resonance in spontaneous breathing of adult

To investigate the role of stochastic resonance in spontaneous breathing control, we measured the pressure variation in the upper airway of six normal adults in an anechoic chamber. We distinguished the spontaneous and volitional breathing by breathing frequency: 12-15 cycles per minute for spontaneous and ~20 cycles per minute for volitional breathing. Fig. 6.1 shows the pressure signal of one subject for both spontaneous and volitional breathing. The pressure waveform of spontaneous breathing is continuous but that of volitional breathing performs "impulsive" pattern clearly. After carting out autocorrelation for the pressure of spontaneous breathing, we found that the respiratory flow fluctuation of spontaneous breathing is not random but has periodic signal imbedded in, and the dominant frequency is around ~5 Hz (Liu et al. 2012).

All the six subjects are Asian, subject 1 is a male about 50 years old, subject 2-5 are males around 25 years old and subject 6 is a female of 30 years old. It is shown in Fig. 6.2 that the SNR increases initially with increasing noise level; after the peak, it decreases with further increasing noise level for both spontaneous and volitional breathing. The existence of such a peak is the principal signature of stochastic resonance and this is the evidence of SR phenomenon in adults. From each sub-figure, it clearly shows that the peak of SNR in spontaneous breathing is higher than that of volitional breathing. This SR phenomenon may play an important role in the respiratory system as periodic signals are enhanced significantly by noise. The SNR values in most of the subjects are above zero with fewer negative values.

6.2.2 The correlation between SNR and AHI for OSA subjects

In our previous work (Liu et al. 2012), we demonstrated that flow oscillation is the intrinsic characteristics of upper airway, and the flow oscillation would be suppressed for obstructed sleep apnea subjects. Here we investigate the SNR variation for OSA subjects. AHI is an index used to assess the severity of OSA based on the total number of apnea and hypopnea of breathing occurring per hour of sleep. For these three OSA subjects, the AHI is 39.8, 12.7 and 15.8, respectively. According to the severity indices of OSA by Yim et al. (2006), Subject #1 is suffering a severe OSA while after UPPP surgery Subject #2 and Subject #3 recovered at an acceptable level. Fig. 6.3a shows the variation of SNR with noise level for normal and OSA subjects. For normal subject, the SNR is much higher than those of OSA subjects and exhibits clearly the signature of SR. For Subject #3 and Subject #2 whose AHI is 15.8 and 12.7 respectively, the SNR is higher than that of Subject #1 OSA subject (AHI=39.8), and the distributions look like the signature of SR. For #1 OSA subject, the AHI is 39.8, which is much higher than those of #2 and #3 OSA subjects, and the SNR is much lower than those of normal and other OSA subjects and even lower than zero. It is clearly shown that the SNR is correlated to AHI (Fig. 6.3b), i.e., the quality of oscillating signal is strongly correlated to OSA symptom. OSA is a disorder characterized by partial or complete pharyngeal airway closure during sleep; one of the main reasons of OSA is the loss of the reflex response, and during sleep the upper airway tissues are more relaxed which alters the fluid-solid coupling especially in OSA subjects. Our analyses support the hypothesis that the stochastic resonance can enhance periodic oscillating signal which is the stimulus to the mechanoreceptors and modulate the upper airway patency. It seems that the quality of the oscillating signal can serve as a quantitative measure to quantify the breathing quality of OSA subject.

6.3 Discussion

From the experimental and numerical study (Liu et al. 2012), we found that there exist flow oscillations in upper airway. It is known that oscillating pressure is the stimulus to trigger the reflex in the respiratory muscles (Henke and Sullivan 1993). Human upper airway is a very complicated system, which results in the highly turbulent and fluctuating respiratory flow due to the narrowness of upper airway. This turbulent flow is nonlinear and the flow separation is found to exist near larynx. The separation gives rise to flow oscillation with frequency of 3 ~ 5 Hz in spontaneous breathing (Liu et al. 2012). This periodic signal is buried under a broad range of noise. In a nonlinear system, the addition of noise can amplify the weak input signal so as to increase the output SNR, which would enhance the periodic signal transmission significantly. This phenomenon is called stochastic resonance. This phenomenon does not occur in linear system in which the noise only degrades the signal quality. Since the turbulent flow fluctuation in upper airway is nonlinear, the oscillating signal induced by the flow separation near larynx could be enhanced through stochastic resonance mechanism by considering the turbulent fluctuation as the input noise signal. According to the starling resistor model, the pressure surrounding the tissue of the oropharynx will contribute to airway collapse if it is larger than the pressure at upper (upstream, nasal) and lower (downstream, hypopharyngeal) segments (Gleadhill et al. 1991, Stalford et al. 2004). While when the muscular tone is sufficiently activated in tissues surrounding the collapsible tube, the pressure surrounding the tissue away from the collapsible element will become very low and the pressure both upstream and downstream would be larger than it; then the breathing is unobstructed (Schwartz et al. 1988, Stalford et al. 2004). For spontaneous breathing, it is believed that the enhanced periodic oscillation activates the mechanoreceptors (Miller 2014; Henke and Sullivan 1993), and this sensory input is transmitted to the central respiratory control system, which regulates effectively the diaphragm and lung movements. The breathing is controlled by various afferent stimuli simultaneously. For volitional breathing, the key efferent stimulus should be from motor cortex, therefore the signal from mechanoreceptor is weak, and the stochastic resonance phenomenon is not as strong as that of spontaneous breathing. The upper airway is in motion when breathing, therefore the morphology of upper airway would be different for spontaneous and volitional breathing. The morphology determines the pattern of flow separation, and it would affect the frequency and amplitude of flow oscillation accordingly, consequently it will influence the SNR of oscillating signal.

There are several factors that influence the patency of the upper airway, such as the negative pressure. Here we just consider one of the factors - flow oscillation due to the flow separation that may be an afferent stimulus to activate the mechanoreceptors. For the OSA subject, the narrowing upper airway suppresses the flow separation that results in the decline of flow oscillation, and consequently lowers the SNR. The SNR is closely correlated to AHI. For lower AHI, i.e. for normal subject or mild OSA subject, the SNR is quite high; for higher AHI, i.e., for severe OSA subject, the SNR is very low, and even below zero. The correlation between SNR and AHI supports the idea that the flow oscillation is the afferent stimulus to activate the mechanoreceptors which is one of the factors to regulate the patency of the upper airway.

6.4 Conclusion

The stochastic resonance (SR) is a phenomenon that addition of noise in a nonlinear system can enhance the response of weak signal transmission significantly. We investigate the SR phenomenon in the respiratory especially in OSA subjects and found that:

1. It is shown that the SNR increases initially with increasing noise level; after the peak, it decreases with further increasing noise level for both spontaneous and volitional breathing, which means there is a SR phenomenon in adults .
2. The peak of SNR in spontaneous breathing is higher than that of volitional breathing. The SR phenomenon may play an important role in the respiratory system as periodic signals are enhanced significantly by noise.
3. SNR is correlated to AHI, one of the main reasons of OSA is the loss of the reflex response, and during sleep the upper airway tissues are more relaxed which alters the fluid-solid coupling especially in OSA subjects. Our analyses support the hypothesis that the stochastic resonance can enhance periodic oscillating signal which is the stimulus to the mechanoreceptors and modulate the upper airway patency. It seems that the quality of the oscillating signal can serve as a quantitative measure to quantify the breathing quality of OSA subject.

Chapter 7 Conclusions and Suggestions for Future Research

7.1 Conclusions

Obstructive sleep apnea (OSA) is a common disorder characterized by partial or complete narrowing of the pharyngeal airway during sleep and widening the upper airway is often used in clinical practice. However, its success rate is unsatisfactory and the failure of the surgery would only exacerbate the symptom. This indicates that the widened airway is not the only criterion to appraise the breathing quality. Many researchers studied the flow in upper airway of OSA patients with CFD simulation; however, none of them has compared the difference between successful and failed surgery models or reported the importance of 3-5 Hz oscillation signal (Luo et.al, 2004; Mihaescu et.al, 2008; Mylavarapu et.al, 2009; Powell et.al, 2011). In this study, we use both numerical and experiments to investigate properly the pathogenesis of this disorder.

In a previous study (Liu et.al, 2012), we found in experiments that an intrinsic peak frequency (3~5 Hz) for the normal subjects which resulted from the flow separation downstream of the minimum cross-sectional area. In this study, both the experimental and numerical studies showed that the SNR at 3-5 Hz signal inversely correlates with AHI severity. This indicates that the 3-5 Hz oscillation signal induced by flow separation may play an important role in breathing control, as the oscillating pressure is the stimulus to trigger the reflex in the respiratory muscles (Henke et.al, 1993). For most of the OSA subjects, whereas the upper airway is narrowed increasing the flow resistance; the widening airway may decrease the flow resistance but it is not guaranteed to enhance the 3-5 Hz oscillation signal. This may be one of the reasons of surgery failure for OSA subject.

For models before surgery, there are several recirculations in the reverse flow region with irregular flow patterns; for models after successful surgery, the flow pattern appears to be regular, and a single dominant recirculation is observed at the downstream of the minimum cross-section, meanwhile the oscillation profile of the wall shear stress time series is regular and follows the breathing curve closely, indicating that the regular oscillation profile may be induced by this dominant recirculation. For the model after failed surgery, there is more than one recirculation due to the morphological changes, the oscillation of wall shear stress time series is strong but it does not follow the breathing curve. Comparing of the flow patterns, we found that upper airway surgery has improved the regularity of flow pattern of the reversed flow. In other words, in the model with a lower AHI, the reversed flow pattern is more regular and there exists a single dominant recirculation at oropharynx.

The flow resistance, or pressure drop, has a significant effect on OSA. Wootton et al., (2013) analysed numerically 15 pairs of obese OSA children and found that (1) the flow resistance in the pharynx and pressure drop from choanae to a minimum cross-section significantly correlates with the AHI, (2) that the correlation between airway minimum cross-sectional and AHI was weaker and, (3) that the airway wall minimum pressure was not significantly correlated to AHI. Our results in the current thesis is consistent with their conclusions. In contrast to the correlation analysis in MMA by Zhao et al.,(2013) for UPPP surgery, we did not observe a significant correlation between the increase in minimum cross-section area and the change of AHI.

In the present thesis we also found the SR phenomenon in both normal and OSA subjects. The peak of SNR in spontaneous breathing is higher than that of volitional breathing. The SR phenomenon may play a crucial part in the respiratory system as periodic signals are enhanced significantly by noise. Our analyses support the hypothesis that the SR can enhance periodic oscillating signal which works as a stimulus to the mechanoreceptors and modulates the upper airway patency. It seems that the quality of the oscillating signal can serve as a quantitative measure to quantify the breathing quality of OSA.

7.2 Suggestions for future research

7.2.1 Experimental study in upper airway

As we discussed in Chapter 4, two 1:1 scaled upper airway models were produced using the 3-D printing technique (3500 HD Max-3D System, USA) with uniform wall thickness (0.5 mm) by rigid material. Due to the non-transparency of the 3-D printing material, the transparent window need to be incision in the orophyarnx wall to measure velocity profiles, which would cause measuring error.

To solve the limitations above, further exploration is needed. For increasing the experimental accuracy, the transparent material should be used to build the model which will decrease the measuring error significantly, and in that case, the velocity profiles of the whole UA can be measured accurately.

In addition, we suggest that flexible material can be used to build the UA models to assess its circumstance in reality.

7.2.2 SR phenomenon in OSA

In this thesis, SR phenomenon has been found in both normal and OSA subjects. Because the periodic signalbe are enhanced significantly by noise, the SR phenomenon may play an vital role in the respiratory system.

In this research, our analyses support the hypothesis that the stochastic resonance can enhance periodic oscillating signal which is the stimulus to the mechanoreceptors while modulating the upper airway patency. It seems that the quality of the oscillating signal can serve as a quantitative measure to quantify the breathing quality of OSA subject.

We suggest that oscillating signal should be the focus of the studies that are interested in quantifying the breathing quality of OSA subjects.

References

[1] Ballentine, R., & Hymes, A. (1998). *Science of breath: A practical guide*. Himalayan Institute Press.

[2] Xu, C., Sin, S., McDonough, J. M., Udupa, J. K., Guez, A., Arens, R., & Wootton, D. M. (2006). Computational fluid dynamics modeling of the upper airway of children with obstructive sleep apnea syndrome in steady flow. *Journal of biomechanics*, *39*(11), 2043-2054.

[3] Lucey, A. D., King, A. J. C., Tetlow, G. A., Wang, J., Armstrong, J. J., Leigh, M. S., ... & Hillman, D. R. (2010). Measurement, reconstruction, and flow-field computation of the human pharynx with application to sleep apnea. *IEEE Transactions on Biomedical Engineering*, *57*(10), 2535-2548.

[4] Levy P., Viot-Blanc V. and Pepin J.L. (2006), Sleep disorders and their classification-An overview. Randerath WJ, Sanner BM, Somers (eds): Sleep Apnea. Prog Respir Res. Basel, Karger, 35, 1-12

[5] Gleadhill, I. C., Schwartz, A. R., Schubert, N., Wise, R. A., Permutt, S., & Smith, P. L. (1991). Upper airway collapsibility in snorers and in patients with obstructive hypopnea and apnea. *American Review of Respiratory Disease*,*143*(6), 1300-1303.

[6] De Backer W. (2006), Obstructive sleep apnea-hypopnea syndrome, Randerath W.J, Sanner B.M., Somers V.K (eds):Sleep Apnea. Prog Respir Res. Basel, Karger, 35, 90-96.

[7] Lipton, A. J., & Gozal, D. (2003). Treatment of obstructive sleep apnea in children: do we really know how?. *Sleep medicine reviews*, *7*(1), 61-80.

[8] Mylavarapu, G., Murugappan, S., Mihaescu, M., Kalra, M., Khosla, S., & Gutmark, E. (2009). Validation of computational fluid dynamics methodology used for human upper airway flow simulations. *Journal of biomechanics*,*42*(10), 1553-1559.

[9] Yim S., Jordan A. and Malhotra A. (2006), Obstructive sleep apnea: Clinical presentation, diagnosis and treatment. Randerath WJ, Sanner BM, Somers(eds): Sleep Apnea. Prog Respir Res. Basel, Karger, 35, 118-136

[10] Remmers, J. E., DeGroot, W. J., Sauerland, E. K., & Anch, A. M. (1978). Pathogenesis of upper airway occlusion during sleep. *J Appl Physiol*, *44*(6), 931-8.

[11] Schneider, H., Boudewyns, A., Smith, P. L., O'Donnell, C. P., Canisius, S., Stammnitz, A., ... & Schwartz, A. R. (2002). Modulation of upper airway collapsibility during sleep: influence of respiratory phase and flow regimen.*Journal of Applied Physiology*, *93*(4), 1365-1376.

[12] Kirkness J.P., Krishnan V., Patil S.P., Schneider H. (2006), Upper airway obstruction in snoring and upper airway resistance syndrome, Randerath W.J, Sanner B.M., Somers V.K (eds):Sleep Apnea. Prog Respir Res. Basel, Karger, 35, 79-89.

[13] Schwartz, A. R., Smith, P. L., Wise, R. A., Gold, A. R., & Permutt, S. (1988). Induction of upper airway occlusion in sleeping individuals with subatmospheric nasal pressure. *Journal of Applied Physiology*, *64*(2), 535-542.

[14] Neill, A. M., Angus, S. M., Sajkov, D., & McEVOY, R. D. (1997). Effects of sleep posture on upper airway stability in patients with obstructive sleep apnea. *American journal of respiratory and critical care medicine*, *155*(1), 199-204.

[15] Szollosi, I., Roebuc, T., Thompson, B., & Naughton, M. T. (2006). Lateral sleeping position reduces severity of central sleep apnea/Cheyne-Stokes respiration. *SLEEP-NEW YORK THEN WESTCHESTER-*, *29*(8), 1045.

[16] Whitelaw, W. A., Brant, R. F., & Flemons, W. W. (2005). Clinical usefulness of home oximetry compared with polysomnography for assessment of sleep apnea. *American journal of respiratory and critical care medicine*, *171*(2), 188-193.

[17] Michael Littner, M. D., David Davila, M. D., Kushida, C. A., & Johnson, S. F. (2002). Practice parameters for the use of auto-titrating continuous positive airway pressure

devices for titrating pressures and treating adult patients with obstructive sleep apnea syndrome. *Sleep*, *25*(2), 143-147.

[18] Boudewyns A. N. and Van de Heyning P.H. (2006), Surgical treatment for obstructive sleep apnea. Randerath WJ, Sanner BM, Somers(eds): Sleep Apnea. Prog Respir Res. Basel, Karger, 35, 167-173

[19] Li, K. K., Powell, N. B., Riley, R. W., Troell, R. J., & Guilleminault, C. (2000). Long-term results of maxillomandibular advancement surgery. *Sleep and Breathing*, *4*(03), 137-140.

[20] Nithiarasu, P., Liu, C. B., & Massarotti, N. (2007). Laminar and turbulent flow calculations through a model human upper airway using unstructured meshes. *Communications in Numerical Methods in Engineering*, *23*(12), 1057-1069.

[21] Iwasaki, T., Saitoh, I., Takemoto, Y., Inada, E., Kanomi, R., Hayasaki, H., & Yamasaki, Y. (2011). Evaluation of upper airway obstruction in Class II children with fluid-mechanical simulation. *American Journal of Orthodontics and Dentofacial Orthopedics*, *139*(2), e135-e145.

[22] Jeong, S. J., Kim, W. S., & Sung, S. J. (2007). Numerical investigation on the flow characteristics and aerodynamic force of the upper airway of patient with obstructive sleep apnea using computational fluid dynamics. *Medical engineering & physics*, *29*(6), 637-651.

[23] Luo X.Y., Hinton J., Liew T.T. and Kan T.T. (2004), LES Simulation of Turbulent Flow in an Upper Airway Model, *Medical Engineering & Physics*. 26, 403-413.

[24] Sung, S. J., Jeong, S. J., Yu, Y. S., Hwang, C. J., & Pae, E. K. (2006). Customized three-dimensional computational fluid dynamics simulation of the upper airway of obstructive sleep apnea. *The Angle Orthodontist*, *76*(5), 791-799.

[25] Zhao, Y., & Lieber, B. B. (1994). Steady inspiratory flow in a model symmetric bifurcation. *Journal of Biomechanical Engineering*, *116*(4), 488-496.

[26] Yu, C. C., Hsiao, H. D., Lee, L. C., Yao, C. M., Chen, N. H., Wang, C. J., & Chen, Y. R. (2009). Computational fluid dynamic study on obstructive sleep apnea syndrome treated with maxillomandibular advancement. *Journal of Craniofacial Surgery*, *20*(2), 426-430.

[27] Nithiarasu, P., Hassan, O., Morgan, K., Weatherill, N. P., Fielder, C., Whittet, H., ... & Lewis, K. R. (2008). Steady flow through a realistic human upper airway geometry. *International Journal for Numerical Methods in Fluids*, *57*(5), 631-651.

[28] Mihaescu, M., Murugappan, S., Kalra, M., Khosla, S., & Gutmark, E. (2008). Large Eddy Simulation and Reynolds-Averaged Navier–Stokes modeling of flow in a realistic pharyngeal airway model: An investigation of obstructive sleep apnea. *Journal of biomechanics*, *41*(10), 2279-2288.

[29] De Backer, J. W., Vos, W. G., Verhulst, S. L., & De Backer, W. (2008). Novel imaging techniques using computer methods for the evaluation of the upper airway in patients with sleep-disordered breathing: a comprehensive review. *Sleep medicine reviews*, *12*(6), 437-447.

[30] Ito, Y., Cheng, G. C., Shih, A. M., Koomullil, R. P., Soni, B. K., Sittitavornwong, S., & Waite, P. D. (2011). Patient-specific geometry modeling and mesh generation for simulating obstructive sleep apnea syndrome cases by maxillomandibular advancement. *Mathematics and computers in simulation*, *81*(9), 1876-1891.

[31] Saksono, P. H., Nithiarasu, P., Sazonov, I., & Yeo, S. Y. (2011). Computational flow studies in a subject‐specific human upper airway using a one‐equation turbulence model. Influence of the nasal cavity. *International Journal for Numerical Methods in Engineering*, *87*(1‐5), 96-114.

[32] Luo, H. Y., & Liu, Y. (2008). Modeling the bifurcating flow in a CT-scanned human lung airway. *Journal of Biomechanics*, *41*(12), 2681-2688.

[33] Anderson, J. D., & Wendt, J. (1995). *Computational fluid dynamics* (Vol. 206). New York: McGraw-Hill.

[34] Sodja, J. (2007). Turbulence models in CFD. *University of Ljubljana*, 1-18.

[35] Pope S.B. (2000). Turbulent Flows. Cambirdge Univeristy Press, Cambridge.

[36] Holmes, D. G., & Connell, S. D. (1989). *Solution of the 2D Navier-Stokes equations on unstructured adaptive grids* (pp. 89-1932). American Institute of Aeronautics and Astronautics.

[37] Batinat, J. T., Branch, U. A., & Yangi, H. T. (1991). Spatial adaption procedures on unstructured meshes for accurate unsteady aerodynamic flow computation.

[38] Anderson, W. K., & Bonhaus, D. L. (1994). An implicit upwind algorithm for computing turbulent flows on unstructured grids. *Computers & Fluids*, *23*(1), 1-21.

[39] Randerath W.J. (2006), Electrical simulation of the upper airway muscles. Randerath W.J., Sanner B.M., Somers (eds): Sleep Apnea. Prog Respir Res. Basel, Karger, 35,160-163.

[40] Fogel, R. B., Malhotra, A., Shea, S. A., Edwards, J. K., & White, D. P. (2000). Reduced genioglossal activity with upper airway anesthesia in awake patients with OSA. *Journal of Applied Physiology*, *88*(4), 1346-1354.

[41] Taylor, E. W., Jordan, D., & Coote, J. H. (1999). Central control of the cardiovascular and respiratory systems and their interactions in vertebrates.*Physiological Reviews*, *79*(3), 855-916.

[42] Miller, R. D., Eriksson, L. I., Fleisher, L. A., Wiener-Kronish, J. P., Cohen, N. H., & Young, W. L. (2014). *Miller's anesthesia*. Elsevier Health Sciences.

[43] Yu, J. (2005). Airway mechanosensors. *Respiratory physiology & neurobiology*, *148*(3), 217-243.

[44] Dempsey, J. A., Smith, C. A., Harms, C. A., Chow, C., & Saupe, K. W. (1996). Sleep-induced breathing instability. University of Wisconsin-Madison Sleep and respiration Research Group. *Sleep*, *19*(3), 236-247.

[45] Sant'Ambrogio, G., Mathew, O. P., Fisher, J. T., & Sant'Ambrogio, F. B. (1983). Laryngeal receptors responding to transmural pressure, airflow and local muscle activity. *Respiration physiology*, *54*(3), 317-330.

[46] Henke, K. G., & Sullivan, C. E. (1993). Effects of high-frequency oscillating pressures on upper airway muscles in humans. *Journal of Applied Physiology*, *75*(2), 856-862.

[47] Dahoe, A. E., & Cant, R. S. (2004). On Least-Squares Gradient Reconstruction and its application in conjunction with a Rosenbrock method.

[48] Bahar, S., & Moss, F. (2003). The nonlinear dynamics of the crayfish mechanoreceptor system. *International Journal of Bifurcation and Chaos*, *13*(08), 2013-2034.

[49] Benzi, R., Sutera, A., & Vulpiani, A. (1981). The mechanism of stochastic resonance. *Journal of Physics A: mathematical and general*, *14*(11), L453.

[50] Bloch-Salisbury, E., Indic, P., Bednarek, F., & Paydarfar, D. (2009). Stabilizing immature breathing patterns of preterm infants using stochastic mechanosensory stimulation. *Journal of Applied Physiology*, *107*(4), 1017-1027.

[51] Bulsara, A. R., & Gammaitoni, L. (1996). Tuning in to noise. *Physics today*,*49*(3), 39-47.

[52] Collins, J. J., Chow, C. C., & Imhoff, T. T. (1995). Stochastic resonance without tuning. *Nature*, *376*(6537), 236-238.

[53] Hagan, R., Bryan, A. C., Bryan, M. H., & Gulston, G. (1977). Neonatal chest wall afferents and regulation of respiration. *Journal of Applied Physiology*,*42*(3), 362-367.

[54] Liu, Y., Ye, J., Liu, Z., Huang, L., Luo, H., & Li, Y. (2012). Flow oscillation—A measure to predict the surgery outcome for obstructed sleep apnea (OSA) subject. *Journal of biomechanics*, *45*(13), 2284-2288.

[55] Moss, F., Ward, L. M., & Sannita, W. G. (2004). Stochastic resonance and sensory information processing: a tutorial and review of application. *Clinical neurophysiology*, *115*(2), 267-281.

[56] Narasimhan, S. V., & Veena, S. (2005). *Signal processing: principles and implementation* (Vol. 1). Alpha Science Int'l Ltd..

[57] Papoulis, A., & Pillai, S. U. (2002). *Probability, random variables, and stochastic processes*. Tata McGraw-Hill Education.

[58] Russell, D. F., Wilkens, L. A., & Moss, F. (1999). Use of behavioural stochastic resonance by paddle fish for feeding. *Nature*, *402*(6759), 291-294.

[59] Suki, B., Alencar, A. M., Sujeer, M. K., Lutchen, K. R., Collins, J. J., Andrade, J. S., ... & Stanley, H. E. (1998). Life-support system benefits from noise. *Nature*, *393*(6681), 127-128.

[60] Wiesenfeld, K., & Moss, F. (1995). Stochastic resonance and the benefits of noise: from ice ages to crayfish and SQUIDs. *Nature*, *373*(6509), 33-36.

[61] Ball, C. G., Uddin, M. & Pollard, A., (2008). Mean Flow Structures Inside the Human Upper Airway. *Flow Turbulence Combust*, 81(1-2), pp. 155-188.

[62] Christian, G., Ara, T. & William, D. C., (1976). The Sleep Apnea Syndromes. *Annual Review of Medicine*, 27, 465-484.

[63] De Backer, J. W., Vanderveken, O. M., Vos, W. G., Devolder, A., Verhulst, S. L., Verbraecken, J. A., ... & De Backer, W. A. (2007). Functional imaging using computational fluid dynamics to predict treatment success of mandibular advancement devices in sleep-disordered breathing. *Journal of biomechanics*, *40*(16), 3708-3714.

[64] Freitas, R. K., & Schröder, W. (2008). Numerical investigation of the three-dimensional flow in a human lung model. *Journal of Biomechanics*, *41*(11), 2446-2457.

[65] Große, S., Schröder, W., Klaas, M., Klöckner, A., & Roggenkamp, J. (2007). Time resolved analysis of steady and oscillating flow in the upper human airways. *Experiments in fluids*, *42*(6), 955-970.

[66] Huang, Y., Malhotra, A., & White, D. P. (2005). Computational simulation of human upper airway collapse using a pressure-/state-dependent model of genioglossal muscle contraction under laminar flow conditions. *Journal of Applied Physiology*, *99*(3), 1138-1148.

[67] Lars, D., 2014. Fluid Mechanics, Turbulent Fow and Turbulence, G¨oteborg, Sweden: Chalmers University of Technology.

[68] Lin, C. L., Tawhai, M. H., McLennan, G., & Hoffman, E. A. (2007). Characteristics of the turbulent laryngeal jet and its effect on airflow in the human intra-thoracic airways. *Respiratory physiology & neurobiology*, *157*(2), 295-309.

[69] Luo, H. Y., Liu, Y., & Yang, X. L. (2007). Particle deposition in obstructed airways. *Journal of Biomechanics*, *40*(14), 3096-3104.

[70] Mihaescu, M., Murugappan, S., Gutmark, E., Donnelly, L. F., & Kalra, M. (2008). Computational modeling of upper airway before and after adenotonsillectomy for obstructive sleep apnea. *The Laryngoscope*, *118*(2), 360-362.

[71] Pope, B. S., 2003. *Turbulent Flows*. s.l.:Cambridge University Press.

[72] Van Lierde, K. M., Van Borsel, J., Moerman, M., & Van Cauwenberge, P. (2002). Nasalance, nasality, voice, and articulation after uvulopalatopharyngoplasty. *The Laryngoscope*, *112*(5), 873-878.

[73] Vos, W. D. B. J., De Backer, J., Devolder, A., Vanderveken, O., Verhulst, S., Salgado, R. & De Backer, W. (2007). Correlation between severity of sleep apnea and upper airway morphology based on advanced anatomical and functional imaging. *Journal of biomechanics*, *40*(10), 2207-2213.

[74] Wilcox, D. C. (1998). *Turbulence Modeling for CFD*. s.l.:California DCW Industries Inc.

[75] Cheng, G. C., Koomullil, R. P., Ito, Y., Shih, A. M., Sittitavornwong, S., & Waite, P. D. (2014). Assessment of surgical effects on patients with obstructive sleep apnea syndrome using computational fluid dynamics simulations. *Mathematics and computers in simulation*, *106*, 44-59.

[76] Luo, X. Y., Hinton, J. S., Liew, T. T., & Tan, K. K. (2004). LES modelling of flow in a simple airway model. *Medical Engineering & Physics*, *26*(5), 403-413.

[77] Malhotra, A., Huang, Y., Fogel, R. B., Pillar, G., Edwards, J. K., Kikinis, R., ... & White, D. P. (2002). The male predisposition to pharyngeal collapse: importance of airway length. *American Journal of Respiratory and Critical Care Medicine*, *166*(10), 1388-1395.

[78] McCabe, C. & Hardinge, M. (2011). Obstructive sleep apnoea. *Practice Nurse*, 41(10), 36-41.

[79] Yeh, T. T., & Hall, J. M. (2008). Uncertainty of NIST airspeed calibrations. *Technical document of Fluid Flow Group*.

[80] Zhao, M., Barber, T., Cistulli, P. A. & Sutherland, K., 2013. Simulation of upper airway occlusion without and with mandibular advancement in obstructive sleep apnea using fluid-structure interaction. Journal of Biomechanics, Volume 46, pp. 2586-2592.

[81] Zhao, M., Barber, T., Cistulli, P. A., Sutherland, K., & Rosengarten, G. (2013). Simulation of upper airway occlusion without and with mandibular advancement in obstructive sleep apnea using fluid-structure interaction.*Journal of biomechanics*, *46*(15), 2586-2592.

[82] Zhao, Y., & Lieber, B. B. (1994). Steady inspiratory flow in a model symmetric bifurcation. *Journal of Biomechanical Engineering*, *116*(4), 488-496.

[83] Heenan, A. F., Matida, E., Pollard, A., & Finlay, W. H. (2003). Experimental measurements and computational modeling of the flow field in an idealized human oropharynx. *Experiments in Fluids*, *35*(1), 70-84.

[84] Martonen, T. B., Quan, L., Zhang, Z., & Musante, C. J. (2002). Flow simulation in the human upper respiratory tract. *Cell biochemistry and biophysics*, *37*(1), 27-36.

[85] Powell, N. B., Mihaescu, M., Mylavarapu, G., Weaver, E. M., Guilleminault, C., & Gutmark, E. (2011). Patterns in pharyngeal airflow associated with sleep-disordered breathing. *Sleep medicine*, *12*(10), 966-974.

[86] Weickert, M., Teike, G., Schmidt, O., & Sommerfeld, M. (2010). Investigation of the LES WALE turbulence model within the lattice Boltzmann framework.*Computers & Mathematics with Applications*, *59*(7), 2200-2214.

[87] Wootton, D. M., Luo, H., Persak, S. C., Sin, S., McDonough, J. M., Isasi, C. R., & Arens, R. (2014). Computational fluid dynamics endpoints to characterize obstructive sleep apnea syndrome in children. *Journal of Applied Physiology*, *116*(1), 104-112.

[88] Zhao, M., Barber, T., Cistulli, P. A., Sutherland, K., & Rosengarten, G. (2013a). Simulation of upper airway occlusion without and with mandibular advancement in obstructive sleep apnea using fluid-structure interaction.*Journal of biomechanics*, *46*(15), 2586-2592.

[89] Zhao, M., Barber, T., Cistulli, P., Sutherland, K., & Rosengarten, G. (2013b). Computational fluid dynamics for the assessment of upper airway response to oral appliance treatment in obstructive sleep apnea. *Journal of biomechanics*, *46*(1), 142-150.

[90] Moss, F., Ward, L. M., & Sannita, W. G. (2004). Stochastic resonance and sensory information processing: a tutorial and review of application. *Clinical neurophysiology*, *115*(2), 267-281.

[91] Narasimhan, S. V., & Veena, S. (2005). *Signal processing: principles and implementation* (Vol. 1). Alpha Science Int'l Ltd..

[92] Stalford C B, (2004). The starling resistor: A model for explaining and treating obstructive sleep apnea. *AANA Journal*, 72 (2) 133-138.

[93] Miyazaki, S., Itasaka, Y., Yamakawa, K., Okawa, M., & Togawa, K. (1989). Respiratory disturbance during sleep due to adenoid-tonsillar hypertrophy. *American journal of otolaryngology*, *10*(2), 143-149.

[94] Rechtschaffen A., Kales A. (1968). A manual of Standardized Terminology, Techniques and Scoring System for Sleep Stages of Human Subjects. *NIH Publication*, No. 204. Washington, U.S. Government Printing Office.

[95] Whyte, K. F., Allen, M. B., Jeffrey, A. A., Gould, G. A., & Douglas, N. J. (1989). Clinical features of the sleep apnoea/hypopnoea syndrome. *QJM*, 72(1), 659-666.

[96] Young, T., Palta, M., Dempsey, J., Skatrud, J., Weber, S., & Badr, S. (1993). The occurrence of sleep-disordered breathing among middle-aged adults. *New England Journal of Medicine*, 328(17), 1230-1235.

[97] Durán, J., Esnaola, S., Rubio, R., & Iztueta, Á. (2001). Obstructive sleep apnea–hypopnea and related clinical features in a population-based sample of subjects aged 30

to 70 yr. *American journal of respiratory and critical care medicine*, 163(3), 685-689.

[98] App, W. E., Boatwright, G. W., Ostrander, S. E., Unruh, M. M., & Winslow, D. H. (1990). Disorder of excessive daytime somnolence: a case series of 1,000 patients. The *Journal of the Kentucky Medical Association*, 88(8), 393-396.

[99] Pride, N. B., Permutt, S., Riley, R. L., & Bromberger-Barnea, B. (1967). Determinants of maximal expiratory flow from the lungs. *Journal of Applied Physiology*, 23(5), 646-662.

[100] Suratt, P. M., Dee, P., Atkinson, R. L., Armstrong, P., & Wilhoit, S. C. (1983). Fluoroscopic and Computed Tomographic Features of the Pharyngeal Airway in Obstructive Sleep Apnea 1–3. *American Review of Respiratory Disease*, 127(4), 487-492.

[101] De Backer, W. (1993). Upper airway reflexes and obstructive sleep apnoea. *European Respiratory Journal*, 6, 9-9.

[102] Mihaescu, M., Mylavarapu, G., Gutmark, E. J., & Powell, N. B. (2011). Large eddy simulation of the pharyngeal airflow associated with obstructive sleep apnea syndrome at pre and post-surgical treatment. *Journal of biomechanics*, 44(12), 2221-2228.

[103] Reinhardt, J. M., D'Souza, N. D. and Hoffman, E. A. (1997). Accurate measurement of intrathoracic airways, *IEEE Transactions on Medical Imaging*, 16, 820–827.

[104] Choi, H. S., Haynor, D. R. and Kim, Y. (1991). Partial volume tissue classification of multichannel magnetic resonance images: a mixel model, *IEEE Transactions on Medical Imaging*, 10, 395–407.

[105] Soltanian-Zadeh, H., Windham, J. P. and Yagle, A. E. (1993). Optimal transformation for correcting partial volume averaging effects in magnetic resonance imaging, *IEEE Transactions on Medical Imaging*, 40, 1204–1212.

[106] Tardif, P. M. (2001). Virtual reality in radiology: virtual intervention, *Proceedings of SPIE*, 4322, 1005–1014.

[107] Kalender, W. (2000). Computed Tomography: fundamentals, system technology,

image quality, applications, *Wiley-VCH Verlag GmbH & Co*, Munich.

[108] Sonka, M., Park, W. and Hoffman, E. A. (1996). Rule-based detection of intrathoracic airway trees, *IEEE Transactions on Medical Imaging*, 15, 314–326.

[109] Mori, K., Hasegawa, J., Toriwaki, J., Anno, H. and Katada, K. (1996). Recognition of bronchus in three dimensional x-ray CT images with application to virtualized bronchoscopy system, *Proceedings of the 13th International conference on Pattern Recognition*, Piscataway, NJ, 3. 528–532.

[110] Schlatholter, T., Lorenz, C., Carlsen, I. C., Renisch, S. and Deschamps, T. (2002). Simultaneous segmentation and tree reconstruction of the airways for virtual bronchoscopy, *Proceedings of SPIE*, 4684, 103-113

[111] Cheng, H. D., Jiang, X. H. and Wang, J. (2002). Color image segmentation based on homogram thresholding and region merging, *Pattern Recognition*, 35, 373–393.

[112] Roerdink, J. and Meijster, A. (2001). The watershed transform: definitions, algorithms and parallelization strategies, *Fundamenta Informaticae*, 41, 187-228.

[113] Torrence, C. and Compo, G.P. (1998) A practical guide to wavelet analysis. Bulletin of the American Meteorological Society, 79, 61-78.

[114] Daubechies, Ingrid. (1992). Ten Lecures on Wavelets. Philadelphia, PA: SIAM.